UNIVERSITY OF CALIFORNIA
RIVERSIDE

Optoelectronics Investigations of Electron Dynamics in 2D-TMD Semiconductor Heterostructure Photocells: From Electron-Hole Pair Multiplication to Phonon Assisted Anti-Stokes Absorption

A Dissertation submitted in partial satisfaction
of the requirements for the degree of

Doctor of Philosophy

in

Physics

by

Fatemeh Barati

December 2018

Dissertation Committee:
Dr. Nathaniel Gabor, Chairperson
Dr. Yongtao Cui
Dr. Vivek Aji

Copyright by
Fatemeh Barati
2018

The Dissertation of Fatemeh Barati is approved:

Committee Chairperson

University of California, Riverside

ACKNOWLEDGEMENT

I would like to thank my advisor, Prof. Nathaniel Gabor, for the patient guidance, encouragement and advices he has provided over my years of being his student. Working with him has been a wonderful experience for me for I not only learned so much from his intellect but also from his friendly and kind manner life lessons, thank you.

I would like to thank Prof. Roland Kawakami for giving me this excellent opportunity of becoming a graduate student at UCR and trusting in me.

I would like to thank Prof. Vivek Aji and Prof. Yongtao Cui for their great ideas and collaborations toward improving my work and their kind support for my future academic goals, Prof. Roger Lake and Dr. Shanshan Su for their theoretical collaboration in part of this work. I'm grateful for my friends and colleagues at QMOlab, Dennis, Max, Trevor, Jacky, and Jed for without their friendship and support the completion of this work would have been all the more difficult. I'm grateful for everyone that has helped me throughout my journey to this day including lab facilities and other research groups here at UCR.

Finally I would like to thank my family, my Mom, my Dad, and my only sister Zahra, and above all Mir, I'm very lucky to have you in my life, and experience the true happiness around you, thank you.

DEDICATION

To my one and only best friend Mir Shahsavar
I couldn't have done this without your support
to my beloved parents
and to my little sister Zahra

ABSTRACT OF THE DISSERTATION

Optoelectronics Investigations of Electron Dynamics in 2D-TMD Semiconductor Heterostructure Photocells: From Electron-Hole Pair Multiplication to Phonon Assisted Anti-Stokes Absorption

by

Fatemeh Barati

Doctor of Philosophy, Graduate Program in Physics
University of California, Riverside, December 2018
Prof. Nathaniel Gabor, Chairperson

Efficient electron-hole (e-h) pair multiplication could lead to highly sensitive photodetectors, electroluminescent emitters, and improved-efficiency photovoltaic devices. In this thesis, using advanced optoelectronic measurements, I discuss the discovery of highly efficient multiplication of interlayer electron-hole pairs at the interface of ultrathin tungsten diselenide / molybdenum diselenide integrated into field-effect heterojunction devices. Electronic transport measurements of the interlayer current-voltage characteristics indicate that interlayer electron-hole pairs are generated by hot electron impact excitation at temperatures near T = 300 K. By exploiting this highly efficient interlayer e-h pair multiplication process, we demonstrated near-infrared optoelectronic devices that exhibit 350% enhancement of the optoelectronic responsivity at microwatt power levels.

We extend our understanding of these materials by conducting spatially and spectrally resolved imaging of the device photoresponse at low temperatures. Under

carefully tuned experimental conditions, we observe phonon assisted anti-stokes absorption near the interlayer exciton edge of the van der Waals semiconductor heterostructure composed of tungsten diselenide and molybdenum diselenide. At low photon energies near 1 eV, we observed a strong photocurrent peak with several low energy echoes spaced by 30 meV below the fundamental absorption feature. We attribute this highly unusual absorption to high-harmonic anti-stokes absorption; The alignment of the exciton dipole moment to the atomic displacement of the out-of-plane optical phonon modes gives rise to resonant absorption features akin to vibronic transitions in molecules. The anti-stokes process is the first and most critical step toward laser cooling of atomic layer semiconductors. Moreover, it could enhance the efficiency of next generation photovoltaics, since it converts vibrational energy into electronic excitations using photons with energies that are lower than the band gap.

TABLE OF CONTENTS

Acknowledgements iv
Dedication v
Abstract vi

Chapter 1: Introduction and Background

1.1 Introduction: Electron-Hole Pair Production and Annihilation 1
1.2 Semiconductor P-N Junctions 2
1.3 Conventional P-N Junction Diodes Band Diagram 2
1.4 Conventional P-N Junction Photodiodes 6
References 8

Chapter 2: Theory of 2DEG and 2D-Transition Metal Dichalcogenides Band Structure

2.1 Introduction 9
2.2 Electronic Structure 10
2.3 Electronic Band Structure of *2L*-WSe_2/$MoSe_2$ 13
2.4 Transport in Conventional Two Dimensional Electron Gas (2DEG) 19
2.4.1 Band Diagram of 2DEG 21
2.4.2 Density of States of 2DEG 23
2.5 Density of States in Transition Metal Dichalcogenides 26
References 28

Chapter 3: Device Fabrication

3.1 Introduction 30
3.2 Wafer Preparation 30
3.3 Exfoliation 31
3.4 Stacking 2D-TMD atomic layers 35
3.5 Device Fabrication 37
References 40

Chapter 4: instrumentation: Low Temperature Broadband Photocurrent Scanning Microscope

4.1 Introduction 41
4.2 Light-Matter Interaction at the Nanoscale 41

4.3 The Supercontinuum Scanning Photocurrent Spectroscopy Microscope 42
4.4 Electronic Transport Experiment Instrumentation 45
4.5 Optical Imaging Microscopy Instrumentation 50
4.6 Optoelectronic Experiment Instrumentation 53
4.6.1 Fianium Supercontinuum Ultrafast Fiber Lasers 53
4.6.2 Princeton Instruments Monochromator 55
4.6.3 Getting Light Into A Monochromator 58
4.6.4 Gathering Spectrally Resolved Light Out Of Monochromator 61
4.6.5 Dual-Axis Scanning Galvo System 63
4.6.6 Spatially And Spectrally Resolved Laser Excitations 66
4.6.7 Power Dependence Experiments 70
4.7 Running Experiments Through Software 72
References 74

Chapter 5: Basic Optical Characterization of TMDs Heterostructures

5.1 Introduction 75
5.2 Raman Spectroscopy 76
5.3 Photoluminescence Spectroscopy 80
5.4 Photocurrent and Differential Reflection Spectroscopy 81
References 84

Chapter 6: Hot Carrier-Enhanced Interlayer Electron–Hole Pair Multiplication in 2D Semiconductor Heterostructure Photocells

6.1 Introduction 85
6.2 2D-TMD Semiconductors Junction Characteristics 86
6.3 Gate Voltage Dependence of I-V_{SD} Characteristics of $2L$-$WSe_2/MoSe_2$ 90
6.4 Temperature Dependence of I-V_{SD} Characteristics of $2L$-$WSe_2/MoSe_2$ 92
6.5 Interlayer Electron Transport of $2L$-$WSe_2/MoSe_2$ 95
6.5.1 Forward Bias Characteristics 96
6.5.2 Reverse Bias Characteristics 99
6.6 Gate and Temperature Dependence of $d\log I/dV_G$ of $2L$-$WSe_2/MoSe_2$ 102
6.7 Power Dependence of I-V_{SD} Characteristics of $2L$-$WSe_2/MoSe_2$ 104
6.8 Comparison of the Model to Experimental Data 108
6.9 Photoresponse of the Atomic Layer Hetero-Junction 110
6.10 2D-TMD N^+-N Junction Characteristics 111
References 114

Chapter 7: Phonon-Assisted Antistokes Upconversion in a 2D-TMD Heterostructure
7.1 Laser Cooling of Semiconductors 115

7.2 Preliminary Optical Characterizations 116
7.3 Spectral Imaging of High-Energy Excitation 119
7.4 Spectral Imaging of Low-Energy Excitation 120
7.5 2D-TMD P-N Junction Characteristics 122
7.5 Phonon-Assisted Antistokes Shift 125
References 128

Chapter 8: Conclusion 129

LIST OF FIGURES

Figure 1.1. P-N junction at equilibrium. 3

Figure 1.2. Schematic representations of depletion layer width and energy band diagram of a P-N junction under various biasing conditions. 4

Figure 1.3. Current-voltage characteristics of a typical silicon P-N junction. 5

Figure 1.4. The semiconductor PN junction photodiode. 7

Figure 2.1. Constituent elements of transition metal dichalcogenides are highlighted in the periodic table. 10

Figure 2.2. Various atomic structures of TMDs. 11

Figure 2.3. Two-dimensional Brillouin zone (BZ) of MX_2. 13

Figure 2.4. Schematics of the $MoSe_2$/*2L*-WSe_2 heterostructure. 15

Figure 2.5. Schematics of the $MoSe_2$/*2L*-WSe_2 electronic band structure. 18

Figure 2.6. Conduction and valence band line-up at a junction between an N-type AlGaAs ad intrinsic GaAs. 21

Figure 2.7. Dispersion relation, band diagram in real space and momentum space. 22

Figure 2.8. Energy band diagram of a 2D-TMD material with hyperbolic band structure. 28

Figure 3.1. Exfoliation process. 34

Figure 3.2. Optical images of a few exfoliated layers of WSe_2, and $MoSe_2$. 34

Figure 3.3. Transfer microscope and device schematics. 35

Figure 3.4. Schematic illustration and optical images of the dry-transfer process. 37

Figure 3.5. Optical images of devices. 39

Figure 3.6. Optical images of a fabricated device with different magnifications from 5x to 100x. 39

Figure 4.1. Schematic diagram of the supercontinuum scanning photocurrent spectroscopy microscope (SSPSM). 44

Figure 4.2. Photograph from the optical cryostat. 45

Figure 4.3. Photograph of wire bonding the electrical pads of the device. 47

Figure 4.4. Schematics of the atomic layer device. 47

Figure 4.5. Photographs and the electrical circuit diagram of the equipment used for electronic experiments. 50

Figure 4.6. Optical imaging microscopy. 52

Figure 4.7. Schematic of the imaging microscope. 52

Figure 4.8. A typical supercontinuum spectrum 54

Figure 4.9. Schematics of the ray diagram of SP-2300 monochromator. 57

Figure 4.10. Monochromator Control Software & Grating efficiency curves of SP2300. 57

Figure 4.11. Diagram of the lens system required for getting light into the entrance slit of MC. 60

Figure 4.12. Getting light into the MC. 60

Figure 4.13. Optical diagram for getting light out of the MC. 62

Figure 4.14. Getting light out of the MC. 62

Figure 4.15. Scanning galvo system. 65

Figure 4.16. Schematics of the scanning Gaussian beam over the surface of the sample. 66

Figure 4.17. Diffraction limited beam spot to the cryostat. 69

Figure 4.18. Power dependence experiment. 71

Figure 4.19. Profile of the custom-written SSM software. 73

Figure 5.1. Schematic drawing of the four Raman active and two inactive modes. 77

Figure 5.2. Optical images, Raman spectroscopy, and PL spectroscopy of devices 79

Figure 5.3. Device geometry and the PL spectra of the 2D semiconductor heterostructure device. 81

Figure 5.4. Differential reflection and photocurrent spectroscopy measurements of Device. 83

Figure 6.1. Various heterostructure band alignments. 86

Figure 6.2, Schematics of the $MoSe_2$/2*L*-WSe_2 electronic band structure under different values of V_{SD} and V_G. 89

Figure 6.3. Gate voltage dependence of the I-V_{SD} and dI/dV_{SD} characteristics in the 2D N^+-N heterojunction device. 91

Figure 6.4. Temperature dependence of the interlayer I-V_{SD} characteristics. 94

Figure 6.5. Schematics of TMD band structure and interlayer electronic transport. 98

Figure 6.6. Gate voltage, source-drain voltage, and temperature dependence of $dlogI/dV_G$ in the atomic layer semiconductor heterostructure device. 103

Figure 6.7, Interlayer photocurrent characteristics and multiplication enhancement in the 2D heterojunction photocell. 106

Figure 6.8. Interlayer current-voltage characteristics in the transport regime near the onset to NDC. 109

Figure 6.9. Wavelength dependence of the photocurrent-voltage characteristics at $T = 300$ K. 111

Figure 6.10. Band structure, and current-voltage characteristics of the 2D semiconductor heterostructure device. 113

Figure 7.1. Device configuration, and Raman Spectra. 118

Figure 7.2. Gate voltage dependence of the excitation photon energy of the P-N atomic layer heterostructure under high excitations. 120

Figure 7.3. Low energy excitations. 122

Figure 7.4. Band structure, and interlayer charge transfer at the P-N junction of 2*L*-WSe_2/$MoSe_2$. 124

Figure 7.5. Gate voltage dependence of I-V_{SD} characteristics under illumination and in the absence of light. 124

Figure 7.6. Band profile, two-level system transitions, and *E*-*K* diagram of the heterointerface of *2L*-WSe_2/$MoSe_2$ 127

CHAPTER 1

INTRODUCTION AND BACKGROUND

1.1 Introduction: Electron-Hole Pair Production and Annihilation

When external energy is supplied to a conventional semiconductor, the valence band electrons may jump to the conduction band leaving behind a vacancy in the valence band called a hole. The electron and the newly formed hole, whose formation required sufficient excess energy to raise the electron across the band gap of the semiconductor, combine to form an electron-hole (e-h) pair. The excess energy required for e-h pair generation can be supplied from a heat source, from high energy charge carriers, or from the interaction of light with the semiconductor. In the inverse process, the excited electron can release the gained energy and recombine back to the conduction band through a process called e-h pair annihilation. Conduction band electrons may also gain sufficient kinetic energy to collide with carriers in the valence band generating additional electron-hole pair via impact ionization[1]. Efficient e-h pair generation results in extra charge carriers and thus could lead to highly sensitive photodetectors, electroluminescent emitters, and improved-efficiency photovoltaic devices. In this thesis, I discuss optoelectronic transport and e-h pair generation in 2D-TMD semiconductors heterostructures configured into P-N and N-N heterojunction devices. For comparison to modern technology, it is informative to first present the basic characteristics and behavior of conventional semiconductors.

1.2 Semiconductor P-N Junctions

Semiconductor P-N junctions are essential building blocks for electronic and optoelectronic devices. In conventional P-N junctions, regions depleted of free charge carriers form on either side of the junction, generating built-in potentials associated with uncompensated dopant atoms. Carrier transport across the junction occurs by diffusion and drift processes influenced by the spatial extent of this depletion region. With the advent of atomically thin van der Waals materials and their heterostructures, it is now possible to realize a P-N junction at the ultimate thickness limit. Van der Waals junctions composed of P- and N-type semiconductors - each just one-unit cell thick - are predicted to exhibit completely different charge transport characteristics than bulk heterojunctions. In this thesis we aim to study the optoelectronic characteristics of atomically thin heterojunctions composed of transition metal dichalcogenides and to do so it is important to first understand the basic working principles of a conventional P-N junction. In this chapter introduce the conventional P-N junction. After describing the basic solid state physics of two-dimensional materials (Chapter2), we then present 2D van der Waals junctions and photo junctions composed of transition metal dichalcogenides in Chapter 6.

1.3 Conventional P-N Junction Diodes Band Diagram

In conventional materials, when P- and N-type semiconductors are jointed together, the large carrier concentration gradients at the junction cause carrier diffusion. Holes from the p-side diffuse into the N-side, and electrons from the n-side diffuse into the P-side. As holes continue to leave the P-side, some of the negative acceptor ions (N_A^-) near the

junction are left uncompensated, since the acceptors are fixed in the semiconductor lattice, whereas the holes are mobile. Similarly, some of the positive donor ions (N_D^+) near the junction are left uncompensated as the electrons leave the n-side. Consequently, a negative space charge forms near the P-side of the junction and a positive space charge forms near the n-side. This phenomenon creates a space charged region at the junction, a region that is depleted of mobile carriers, called the depletion region[1]. This space charge region creates an electric field that is directed from the positive charge toward the negative charge, as indicated in Fig. 1.1b at top.

The electric field is in the direction opposite to the diffusion current for each type of charge carrier. The lower illustration of Fig. 1.1b shows that the hole diffusion current flows from left to right, whereas the hole drift current due to the electric field flows from right to left.

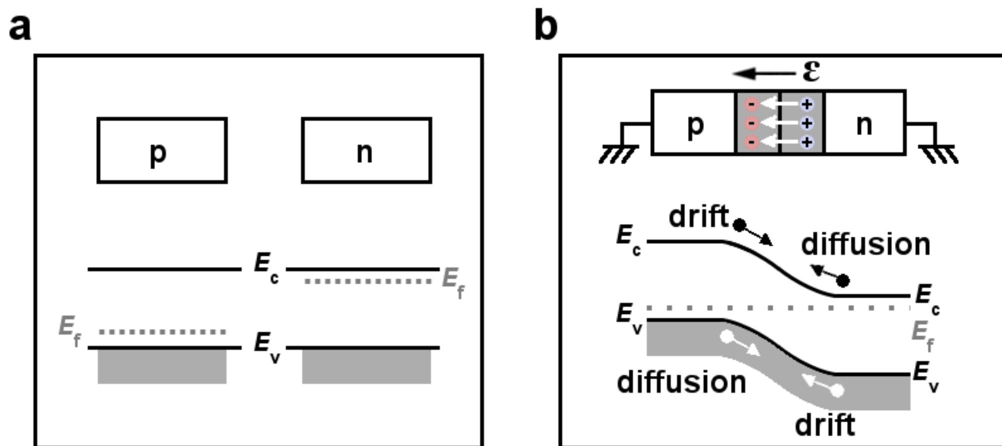

Figure 1.1. P-N junction at equilibrium. a, Uniformly doped P-type and N-type semiconductors before the junction is formed. b, The electric field in the depletion region and the energy band diagram of a P-N junction in thermal equilibrium.

The electron diffusion current also flows from left to right, whereas the electron drift current flows in the opposite direction. The diffusion of carriers continues until the drift current balances the diffusion current, then reaching a thermal equilibrium as indicated by a constant Fermi energy. The equilibrium energy band diagram, shown again in Fig. 1.2a, illustrates that the total electrostatic potential across the junction is V_{bi}. The corresponding potential energy difference from the P-side to the n-side is approximately qV_{bi}. Forward and reverse bias conditions are illustrated in Fig. 1.2 b, & c.

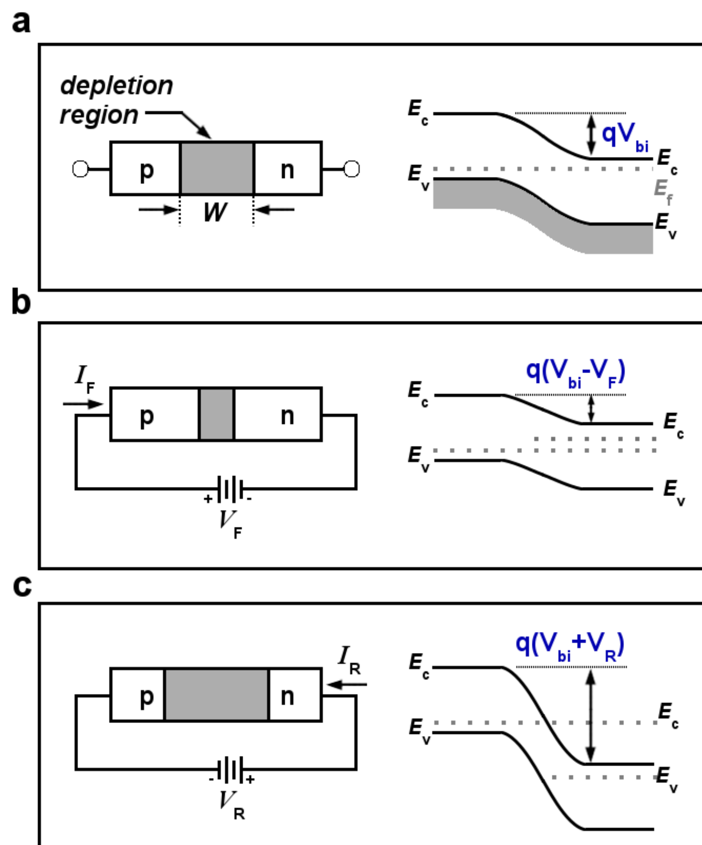

Figure 1.2. Schematic representations of depletion layer width and energy band diagram of a P-N junction under various biasing conditions. a, Thermal equilibrium condition. b, Forward bias condition. c, Reverse bias condition.

The most important characteristic of P-N junctions is that they rectify, that is, they allow current to flow easily in only one direction. Figure 1.3 shows the current-voltage characteristics of a typical silicon P-N junction.

Forward Bias:

If we apply a positive voltage V_f to the p-side with respect to the n-side, the P-N junction becomes forward-biased, as shown in Fig. 1.2b. The total electrostatic potential across the junction decreases by V_f and becomes V_{bi}- V_f. Thus, forward bias reduces the depletion layer width[2].

Reverse Bias:

By contrast, as shown in Fig, 1.2c, if we apply positive voltage V_R to the N-side with respect to the p-side, the P-N junction now becomes reverse-biased and the total electrostatic potential across the junction increases by V_R becoming $V_{bi} + V_R$. Here, we find that reverse bias increases the depletion layer width[2].

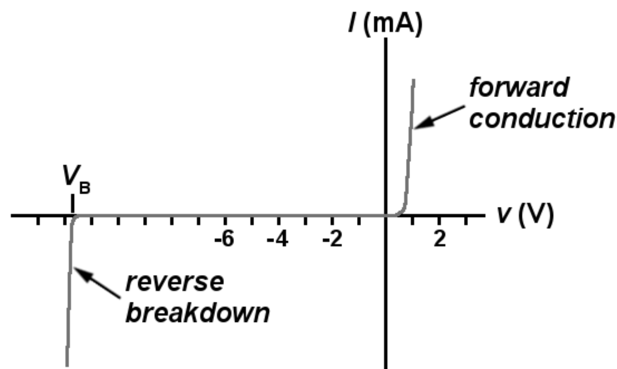

Figure 1.3. Current-voltage characteristics of a typical silicon P-N junction.

1.4 Conventional P-N Junction Photodiodes

One of the interesting approaches to studying the interaction of light with matter is through photo-sensitive diode devices. Because the PN junction is composed of semiconducting materials, the minimum energy required to excite an electron from the valence band to the conduction band is the band gap energy E_{GAP}. The electronic potential energy profile and schematic device characteristics are shown in figure 1.4

The P-N junction is an important electronic and optoelectronic element in modern electronics, yet also provides an experimental platform to study light-matter interactions in novel semiconductor materials such as atomically thin van der Waals materials. If a photon whose energy exceeds the band gap energy is incident on the P-N junction, it creates an electron-hole pair that is separated by the electric field and collected at the contacts. This leads to additional current that offsets the dark current-voltage (I-V) characteristic, illustrated in Fig. 1.4b. In forward bias, the amount of optical power converted to electrical power generated in the device, $P = I_0V_0$, is the power conversion efficiency. This is the basic operating principle of solar cell devices used for energy harvesting. In reverse bias, the built-in field may become so strong that electrons and holes are accelerated to high kinetic energies, giving rise to avalanche multiplication used in highly sensitive photodetectors.

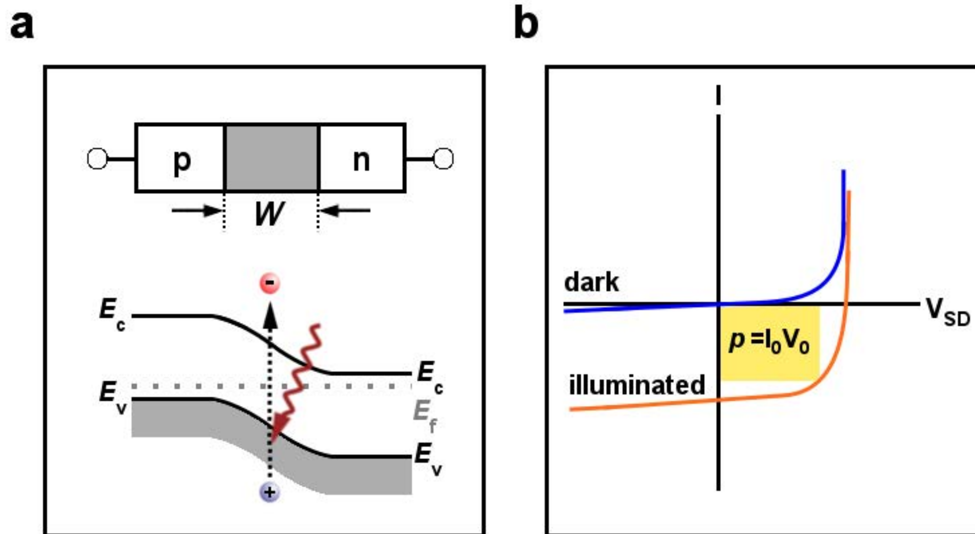

Figure 1.4. The semiconductor PN junction photodiode. a, Schematic potential energy diagram for electrons in a PN junction showing the potential energy barrier (or built-in electric field). An incident photon excites an electron-hole pair in the junction. The electron-hole pair is separated and collected at the device contacts. b, Typical current-voltage characteristics for a conventional PN junction. This figure is adapted from reference 3.

REFERENCES

1. Sze, M. & NG, K. K. *Physics of Semiconductor Devices*. (Wiley-Interscience publications, United States, 1963).

2. Datta, S., *Electron Transport in Mesoscopic Systems*. (Cambridge university Press, *Cambridge, 1995).*

3. *Gabor, N. M. Extremely Efficient and Ultrafast: Electrons, Holes, and their Interactions in the Carbon Nanotube P-N Junction.* (Cornell University, 2012).

CHAPTER 2

THEORY OF TRANSITION METAL DICHALCOGENIDES BAND STRUCTURE

2.1 Introduction

Transition metal dichalcogenides are a class of materials with stoichiometry MX_2, where M is a transition metal of group-IV, group-V or group-VI, and X represents a chalcogen, such that one hexagonally packed layer of M atoms is sandwiched between two layers of X atoms. The bulk of TMDs consist of stacked sheets of atomically thin layers, each layer typically with a thickness of 6~7 Å. The intralayer M–X bonds are predominantly covalent in nature, whereas the sandwich layers are coupled by weak van der Waals forces thus allowing the crystal to easily cleave along the layer surface. The properties of bulk TMDs are diverse, ranging from insulators such as HfS_2, semiconductors such as $MoSe_2$ and WSe_2, semimetals such as WTe_2 and $TiSe_2$, to true metals such as NbS_2 and VSe_2. Exfoliation of these materials into atomically thin two-dimensional crystals preserves their bulk properties, while new physical properties emerge due to quantum confinement effects. Among them, monolayers of group-VI transition metal dichalcogenides are of particular interest as a family of ultrathin semiconductors[1].

In this chapter we first present an intuitive description of the electronic band structure of this class of 2D layered materials and then explicitly discuss some of the

exotic properties that emerge in them due to quantum confinement.

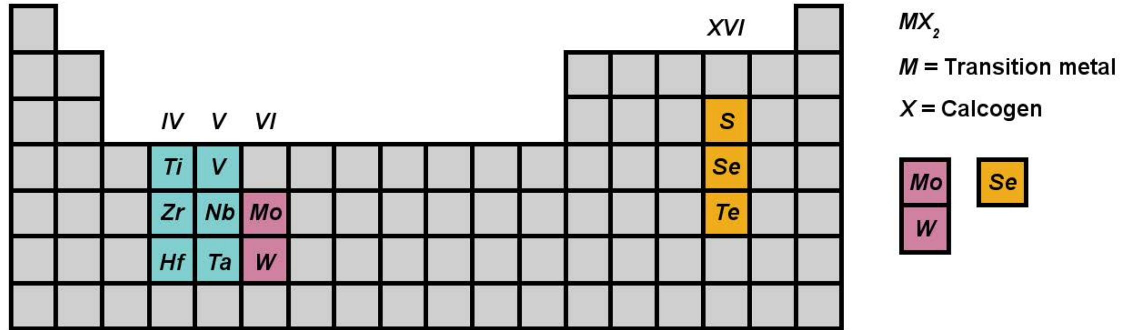

Figure 2.1. Constituent elements of transition metal dichalcogenides are highlighted in the periodic table. One transition metal (group IV, V, and VI) and two chalcogen atoms (group XVI) form TMD crystals. The semiconductor TMD materials used in this thesis are Mo, W, and Se.

2.2 Electronic Structure

The electronic structures of two- dimensional (2D) TMDs are largely determined by their crystal structures. Their layered bulk structure is the stacking of monolayers by weak van der Waals like forces, while in plane stability of monolayers is provided by strong covalent bonds. Among the various TMDs, the group-VIB materials (M=Mo, W; X=S, Se) have been most extensively studied in 2D forms, where both the monolayers and few-layers are proved to be stable in air under room temperature. In this thesis, we focus primarily on $MoSe_2$ and WSe_2 and heterostructures composed of these two constituents.

In TMDs, each transition metal atom is surrounded by six chalcogen atoms that coordinate in either trigonal prismatic or octahedron in three different layered structures

1T, 2H, and 3R (Figure 2.2 a, b). 1T is not as stable as the 2H and 3R phases for the two group-VIB TMDs we are focusing on in this thesis. For the 2H and 3R phases, the monolayer has the identical structure and the difference lies in the stacking order of the monolayers in the layered structures[2].

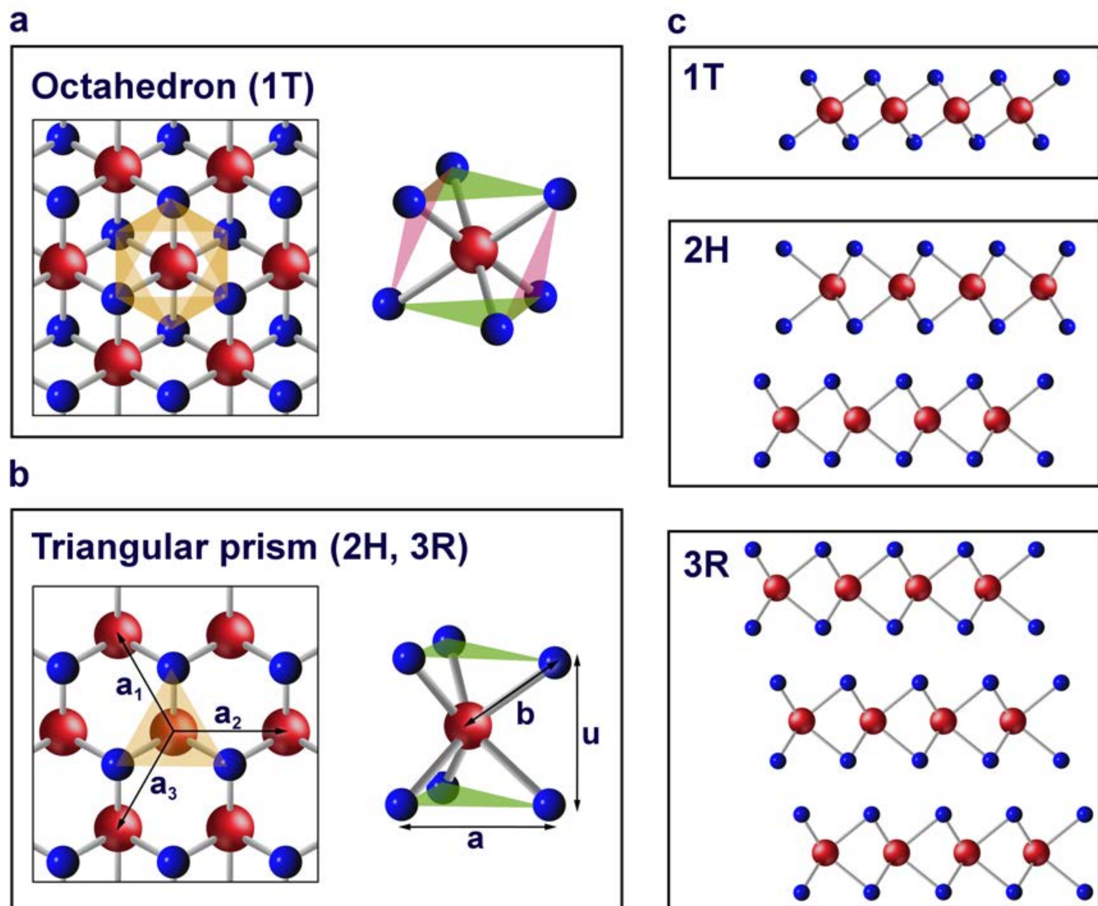

Figure 2.2. Various atomic structures of TMDs. a, Top view of an octahedral coordination of a TMD with transition atoms (red) and chalcogen atoms (blue) at the left and the polymorph structure at right, octahedron only has one form of 1T layered structure. b, Triangular prism coordination with 2H, and 3R structure and the polymorph structure. c, Side view of 1T, 2H, and 3R polytype structures. This figure is adapted from reference 3.

The 2H phase of bulk TMD crystals exhibits hexagonal symmetry, having two monolayers per repeat unit, where the neighboring monolayers are rotated 180◦ with respect to each other. The 3R phase has the rhombohedral symmetry, having three layers per repeat unit, where the neighboring layers are translations of each other (Figure 2.2 c). In general, thin film TMDs exfoliated from the natural crystals are mostly 2H stacking[3].

In MX_2 crystals with trigonal prism structure, we require three lattice parameters *a, b*, and *u* to describe the crystal structure. As shown in Figure 2.2b, *a* = distance between nearest neighbor in-plane M–M and X–X atoms, *b*= nearest neighbor M–X separation, and *u*= distance between the M and X planes. The corresponding in-plane hexagonal Brillouin zone contains the high-symmetry points $\Gamma=(0,0)$, $K=\frac{4\pi}{3a}(1,0)$, $M=\frac{4\pi}{3a}(0,\frac{\sqrt{3}}{2})$ shown in figure 2.3[4]. Using a_1 and a_2 the primitive vectors of the real 2D lattice described by equation (2.1) shown in figure 2.2a, we can calculate the corresponding reciprocal lattice vectors b_1, and b_2 according to equation (2.2) shown in figure 2.3.

$$b=\sqrt{\frac{7}{12}}a\,,\; u=\frac{a}{2}$$

$$\overrightarrow{a_1}=\frac{a}{2}\left(\sqrt{3}\vec{x}+\vec{y}\right) \qquad \overrightarrow{a_2}=\frac{a}{2}\left(-\sqrt{3}\vec{x}+\vec{y}\right) \tag{2.1}$$

$$\overrightarrow{b_1}=\frac{2\pi}{a}\left(\frac{\sqrt{3}}{3}\overrightarrow{K_x}+\overrightarrow{K_y}\right) \qquad \overrightarrow{b_2}=\frac{2\pi}{a}\left(-\frac{\sqrt{3}}{3}\overrightarrow{K_x}+\overrightarrow{K_y}\right) \tag{2.2}$$

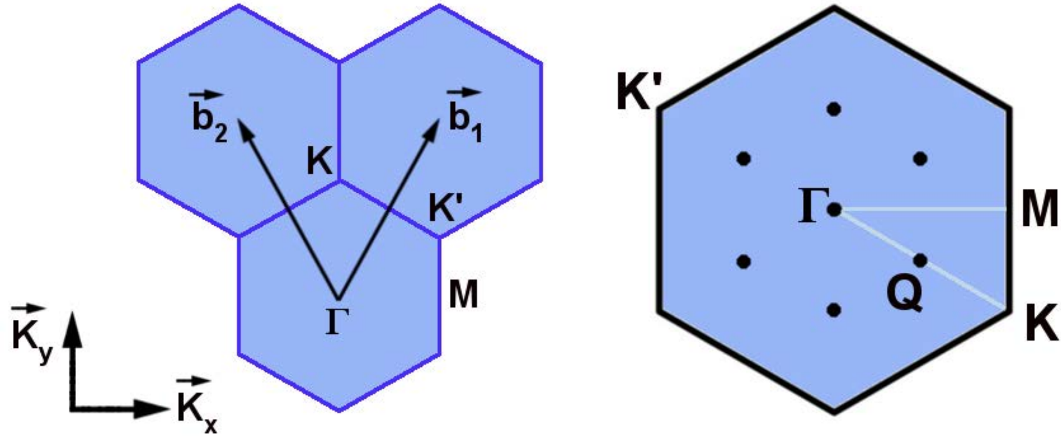

Figure 2.3. Two-dimensional Brillouin zone (BZ) of MX_2. The high symmetry points Γ, K, K' and M are shown. Vectors b_1 and b_2 denote the in-plane reciprocal lattice vectors. Adapted from. Figure adapted from reference 4.

The six Q points in Figure 2.3 (which are not high symmetry points) correspond to the approximate position of the edges of the conduction band in multi-layer TMD. In monolayers, it is important to note that the conduction band minimum (CBM) and the valence band maximum (VBM) are both located at the corners of the first BZ, where they are considered as the only active band. In the next section, we present calculations of the band structures that result from combining these unique crystal structures. We then use this knowledge to understand the band structure near the corners of the BZ.

2.3 Electronic Band Structure of 2L-WSe_2/$MoSe_2$

When combined into heterostructures the transition metal dichalcogenides band structure changes and forms a new band structure at the interface of the two materials. This new band structure is completely distinguished from each of the individual layers,

just like a new semiconductor with its own band structure. Throughout this thesis, we study the electronic band structure of a heterostructure composed of *2L*-WSe_2/$MoSe_2$ at the high symmetry points of K. In this section, we present detailed band structure calculations of the new band structure that emerges in this unique combination of materials.

As discussed in previous section, monolayers of TMD are formed by layers in which the transition metal atom (W or Mo) is sandwiched between sulfur or selenium atoms. The atomic model representing the heterostructure of a *2L*-WSe_2 stacked on top of a layer of $MoSe_2$ is illustrated in figure 2.4a. Figure 2.4b illustrates the atomic layer heterostructure on a Si/SiO_2 substrate with back gate and source and drain contacts. In the remainder of this section the theoretical discussion on the electronic band structure of this heterostructure is represented under applying positive and negative electric field between the two layers.

Band dispersions and band gap energies of the $MoSe_2$/*2L*-WSe_2 heterostructure including spin-orbit coupling (SOC) were calculated using the Vienna ab initio simulation package (VASP)[5-7] in the projected-augmented-wave method[8]. We used the generalized gradient approximation (GGA) of the Perdew-Burke-Ernzerhof (PBE)[9-11] form for the exchange correlation energy.

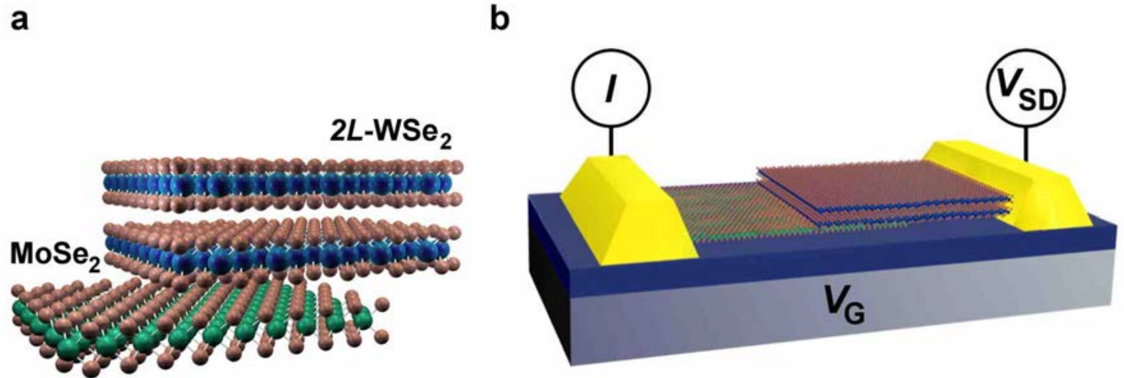

Figure 2.4. Schematics of the $MoSe_2$/*2L*-WSe_2 heterostructure. a, Schematic illustration of the atomic layer structure of a stack of *2L*-WSe_2 on a layer of $MoSe_2$. b, Heterostructure integrated into a field effect transistor with source and drain contacts and a back-gate from underneath.

The van der Waals (vdW) interactions between the layers are accounted for by using the DFT-D2 method of Grimme[12]. We set the kinetic energy cutoff for our calculation at 500 eV. For all structural relaxations, the convergence tolerance on the Hellmann-Feynman forces is less than 0.01 eV/Å. An 8×8×1 Γ-centered Monkhorst-Pack k- point mesh is used for the 2D films. A vacuum layer of 20 Å is included in the supercell in the z- direction to prevent interactions between the periodic repetitions of the two-dimensional structure. With these settings, the lattice constant of $MoSe_2$ is calculated as 3.3247 Å and the lattice constant of WSe_2 as 3.326 Å, so the lattice mismatch between the two materials is less than 0.1%.

Our simulation results are consistent with the published lattice constants of the two materials[13,14]. For the trilayer heterostructure, the lattice constant is 3.3254 Å. The calculated vdW gap between $MoSe_2$ and bilayer WSe_2 is 3.15 Å (the vertical distance

between the Se and Se atoms), which is consistent with the published results of ref.[15]. The thickness of trilayer system is 12.94 Å (the vertical distance between Mo to the furthest W atom). The calculated PBE bandgaps of monolayer $MoSe_2$ and bilayer WSe_2 are 1.317 eV and 1.18 eV, respectively. Our calculated results are consistent with prior simulation results[16,17]. Experimental measurements show that the bandgap of monolayer $MoSe_2$ is 1.55 eV[18], and the bandgap of bilayer WSe_2 has an indirect bandgap of 1.26 eV[19].

The band alignment and band structure of the combined trilayer TMD heterostructure under different electric fields are calculated, and a small sample of band-alignments are shown in Figure 2.5 below. Band structure calculations of the $MoSe_2$/*2L*-WSe_2 heterostructure give an intrinsic type II heterojunction, and exhibit strong qualitative and quantitative agreement with the band offset energies obtained from electronic transport measurements. Figure 2.5 shows the calculated $MoSe_2$/*2L*-WSe_2 heterostructure band alignment under negative (Fig. 2.5a), zero (Fig. 2.5b), and positive (Fig. 2.5c) applied electric field. The electric field is oriented perpendicular to the 2D plane to simulate the electric field due to interlayer applied V_{SD}.

Figure 2.5a shows the heterostructure band alignment under a negative V_{SD} bias voltage, which was calculated by applying a negative electric field of -0.2 eV/Å, pointing from WSe_2 to $MoSe_2$. With this negative electric field the bandgap is a 0.73 eV direct gap. For bilayer WSe_2, the conduction band minimum (CBM) composed of d_{Z^2} is at K, while the valence band maximum (VBM) composed of W $d_{x^2-y^2}$ and d_{xy} is also at K. The $MoSe_2$ also has a direct gap at the K valley. The orbital composition is the same as WSe_2.

Figure 2.5b shows the heterostructure bands with no applied electric field. Here the band gap is an indirect 0.94 eV gap and shows features indicative of an intrinsic type II heterojunction. The bandgap of bilayer WSe_2 is 1.14 eV while the bandgap of $MoSe_2$ is 1.25 eV. The CBM is at the K valley as set by $MoSe_2$, while the VBM is at the Γ valley from WSe_2. In the $MoSe_2$ layer, the CBM is at K and the VBM is at Γ. The CBM is composed of Mo d_{z^2}. The VBM is composed of d_{z^2}. In the WSe_2 layer, the CBM is also at K; the VBM is at the Γ valley. WSe_2's CBM is also composed of d_{z^2}, while its VBM is composed of d_{z^2} . Figure 2.5c shows the band alignment of the heterostructure under positive V_{SD}, which was calculated by applying positive electric field 0.2 eV/Å.

From the heterostructure height of 2.0 nm, a direct correlation between eV_{SD} and electric field would give an approximate V_{SD} value of $V_{SD} > 4$ V. For N-type conduction, the potential barrier is fully reduced, thus giving rise to current flow in high forward bias (See section 3.9.1 for details). We note that, due to several regimes of device transport, the quantitative changes of the band structure with electric field cannot be dependably related to exact applied voltage. In Figure 2.5c, the minimum gap of 0.96 eV is completely determined by WSe_2. The CBM, which is composed of W's $d_{x^2-y^2}$ and d_{xy}, is at Σ, while the VBM composed of W's d_{z^2} is at the Γ valley. $MoSe_2$ has direct gap with its CBM and VBM both at K. The composition of the CBM of $MoSe_2$ is Mo d_{z^2}; the VBM composition of $MoSe_2$ is $d_{x^2-y^2}$ and d_{xy}.

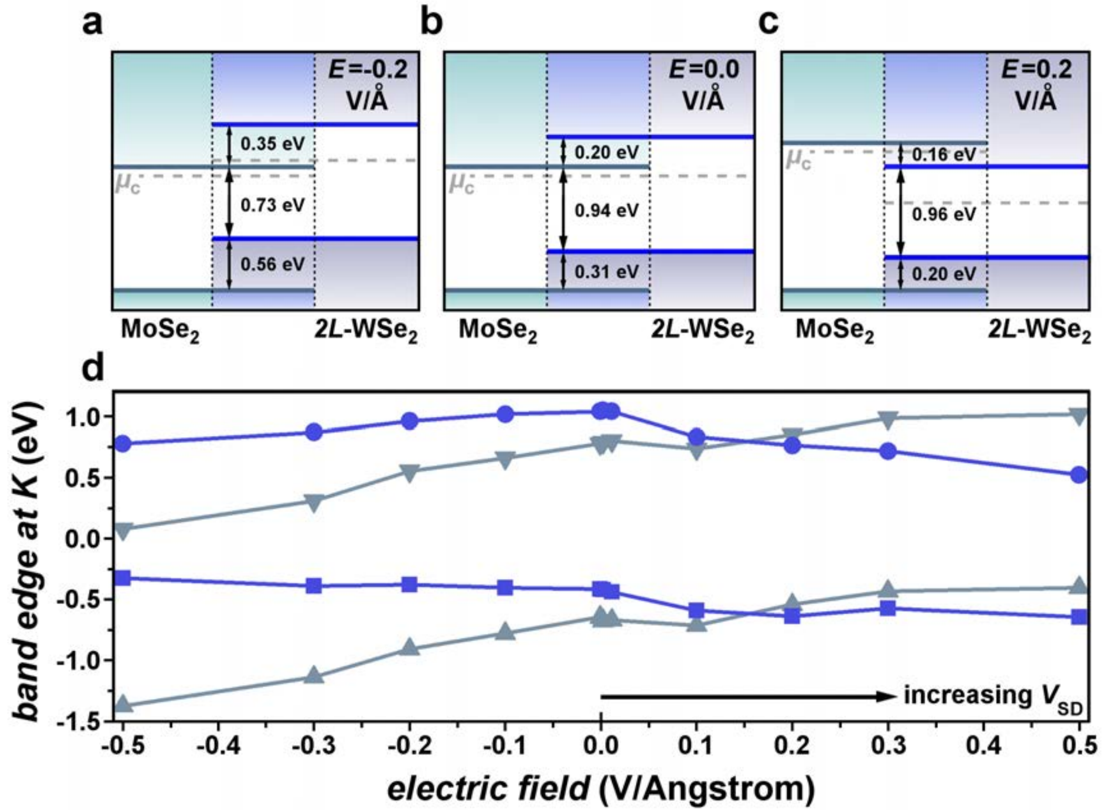

Figure 2.5. Schematics of the $MoSe_2$/*2L*-WSe_2 electronic band structure. a, b, c, Schematic illustration of the electronic band structure of the heterostructure under negative, zero, and positive electric field, respectively. Gray horizontal dashed lines show chemical potential of the individual layers, and the region in between the two vertical dashed lines is the junction. d, Band edge energies as a function of applied electric field. Positive electric field is in the direction of forward applied V_{SD}. Data colors match band edge assignments in a-c. Circles (inverted triangles) correspond to WSe_2 ($MoSe_2$) conduction band minimum. Squares (triangles) correspond to WSe_2 ($MoSe_2$) valence band maximum.

Figure 2.5d shows the transition of the conduction and valence bands as a function of applied electric field. The conduction bands in $MoSe_2$ and WSe_2 grow closer together at low electric fields ($E < 0.2$ eV/Å), and eventually cross over, giving rise to the high-field condition shown in Figure 2.5c. At negative electric fields, corresponding to

reverse V_{SD}, the conduction bands grow farther apart in energy, giving rise to the conditions in Figure 2.5a.

The band structure calculations confirm an indirect band gap at the interface of $MoSe_2$ and WSe_2 forming a staggered band alignment, knowing the electronic band structure of the system allows us to electrostatically tune the chemical potential around. The calculations revealed a band gap of about 1ev at the interface of this system, which is the activation energy one needs to photoexcite an electron across the interface, this number is consistent with all other previously reported literature[16,18,19, &23]. This information will be important in the future to optimize the optoelectronic parameters and create an interlayer exciton in order to study anti-stokes absorption process (chapter 7). We note that the quantitative changes of the band structure with electric field cannot be dependably translated to V_{SD} without detailed knowledge of the potential energy landscape as a function of voltage. However, the band structure calculations can be used as a guide to confirm our understanding of the effects of an applied electric field due to applied V_{SD}, as discussed in the next section.

2.4 Transport in Conventional Two Dimensional Electron Gas (2DEG)

In order to understand the electronic transport and the interaction of light with two-dimensional transition metal dichalcogenides, we need to understand the density of available electronic states (DOS). We continue the remainder of this chapter with first introducing and understanding the 2D electron gas, and how transport takes place in this prototypical system. We then review the parabolic nature of the band diagram of 2DEG

and derive the density of states of this conventional 2D system. Finally we introduce the band dispersion of 2D-TMD and introduce its hyperbolic functionality and then calculate the density of available electronic states in them and later compare the results with the conventional 2DEG system.

The two dimensional electron gas is an electron gas that is free to move in two dimensions, but tightly confined in the third dimension. This confinement leads to quantized energy levels for motion in the third direction, giving rise to high energy subband structure that may be ignored when studying electron transport. Thus the electrons appear to be a 2D sheet embedded in a 3D world.

To understand how this 2D electron layer is formed, we must first consider the band structure that results from combining AlGaAs and GaAs. Bringing two layers into contact (Figure 1.2) creates a hetero-junction at the interface. The conduction and valence band line-up in the z-direction when we first bring the layers in contact. The Fermi energy E_f in the wide gap AlGaAs layer is higher than that in the narrow gap GaAs layer[20]. Consequently electrons spill over from the n-AlGaAs leaving behind positively charged donors. This space charge gives rise to an electrostatic potential that causes the bands to bend as shown in figure 2.6. At equilibrium the Fermi energy is constant everywhere. The electron density is sharply peaked near the GaAs-AlGaAs interface (where the Fermi energy is inside the conduction band) forming a thin conducting layer, which is usually referred to as the two-dimensional electron gas (2DEG)[20].

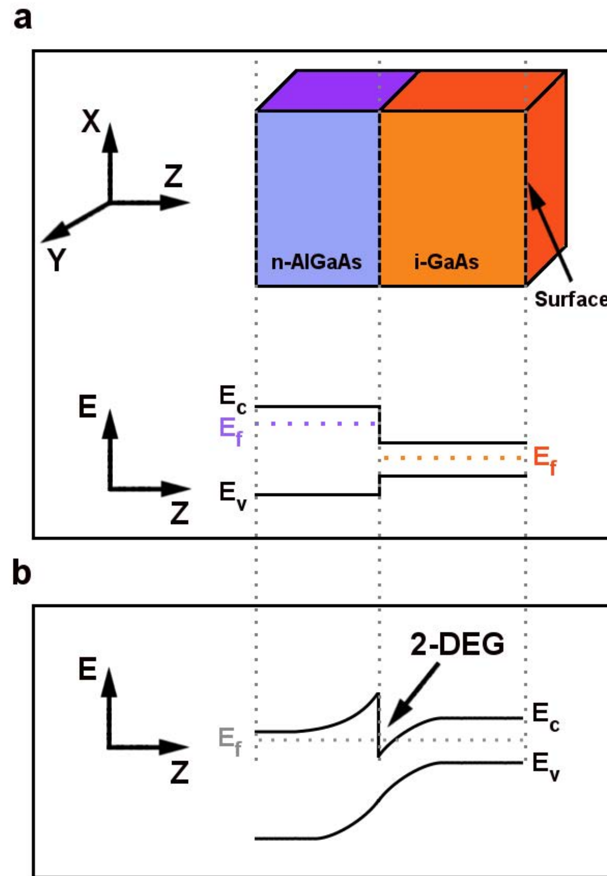

Figure 2.6. Conduction and valence band line-up at a junction between an N-type AlGaAs ad intrinsic GaAs, a, Before and b, After charge transfer has taken place. Note that this is a cross-sectional view. This figure is adapted from reference 20.

2.4.1 Band Diagram of 2DEG

Here (in sections 2.4.1 and 2.4.2) we aim to find out the density of electronic states in a conventional two-dimensional electron gas and study its relation with electronic energy, then later in section 2.5 we study the density of electronic states in an atomic layer 2D-TMD to compare the results. To calculate the density of states we need to first find out

the dispersion relation of the band diagram by solving the Schrodinger equation (2.3), for a free electron gas in the absence of magnetic fields, the eigenfunctions are obtained from equation 2.3,

$$\left[E_S + \frac{\left(i\hbar\nabla + eA\right)^2}{2m} + U\left(x, y\right)\right]\Psi(x, y) = E\Psi(x, y) \tag{2.3}$$

by setting U=0 and A=0, The eigenfunctions normalized to an area S (a circle with radius a in Fig. 2.7) have the form:

$$\Psi(x, y) = \frac{1}{\sqrt{S}}\exp\left(ik_x x\right)\exp\left(ik_y y\right) \tag{2.4}$$

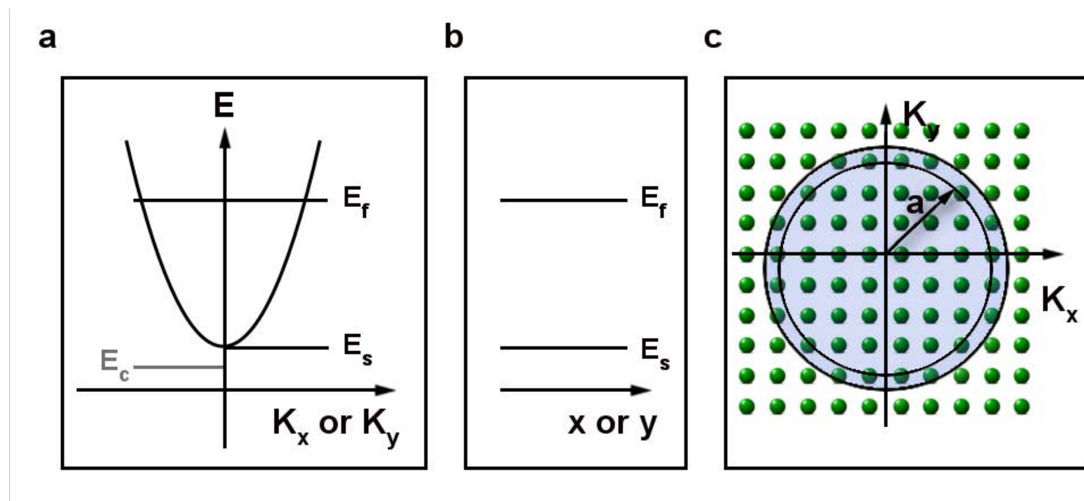

Figure 2.7. Dispersion relation, band diagram in real space and momentum space. a, Dispersion relation for a free electron gas in two dimensions. Note that the bottom of the two-dimensional sub-band E_s lies a little higher than the conduction band edge E_c in the bulk material. b, Band diagram in real space showing only the bottom of the band and the Fermi energy, E_f. c, Assuming periodic boundary conditions, k_x, and k_y take on quantized values depending on the dimensions of the sample. This figure is adapted from reference 20.

with eigenenergies given by

$$E = E_S + \frac{\hbar^2}{2m}\left(k_x^{\ 2} + k_y^{\ 2}\right) \tag{2.5}$$

The dispersion relation equation 2.5 is sketched in figure 2.7a. It is also common to draw band diagrams in real space showing only the bottom of the band (corresponding to k_x=k_y=0) and the Fermi energy.

2.4.2 Density Of States of 2DEG

Having the eigenfunctions of the dispersion relation of a 2DEG we can now calculate the density of states. It describes the number of states per interval of energy at each energy level available to be occupied by electrons (holes), referring to the number of quantum states per unit energy. In other words, the density of states, denoted by *g(E)* indicates how densely packed quantum states are in a particular system. Integrating the density of the quantum states over a range of energy will produce a number of states ($N(E)$) indicated by equation 2.6. The number of quantum states is important in the determination of optical properties of a material.

$$N(E) = \int_E^{\Delta E} g(E)dE \tag{2.6}$$

Here *g(E)dE* represents the number of states between *E* and *dE*. From the Schrodinger equation (2.4.1), we found that the energy of a particle is quantized and is given by:

$$E = \frac{k^2\hbar^2}{2m} \tag{2.7}$$

The variable *k* is related to the physical quantity of momentum. A particle's energy is

$$E = \frac{1}{2}mv^2 = \frac{m^2v^2}{2m} = \frac{p^2}{2m}$$

Relating the previous two equations yields

$$E = \frac{k^2\hbar^2}{2m} = \frac{p^2}{2m} \rightarrow k = \frac{p}{\hbar}$$

Here the momentum is a vector, which has components in the x, y, and z directions. Therefore, k must also have direction components k_x, k_y, and k_z. However in 2D, an electron is confined along one dimension but able to travel freely in the other two directions. In the image below, an electron would be confined in the z-direction but would travel freely in the XY plane and it can only exist in the well.

The wave function in a 1D well is given by

$$\psi(x) = A\cos(kx) + B\sin(kx) \tag{2.8}$$

where $k = \frac{n\pi}{a}$, where a is the width of the barrier. In two dimensions:

$$k_x = \frac{n_x\pi}{a},\ k_y = \frac{n_y\pi}{a},\ \text{and } k_z = \frac{n_z\pi}{a}$$

To calculate density of states we need to find the number of states in the interval of E and $E+dE$. In k-space, the interval is simply k and $k+dk$. In the 2D case, the unit cell is simply a square with side length of π/a (The unit cell is the smallest shape which can repeatedly be used to construct a lattice as in a diamond crystal). In figure 2.7c, the area of the unit cell is:

$$A_0 = \left(\frac{\pi}{a}\right)^2$$

Next, we need to find the area of the ring and then divide by the area of the unit cell. The area of a circle is πr^2 where r is the radius. The area of the ring is then:

$$A = \frac{1}{4}\left(\pi(k+dk)^2 - \pi k^2 = 2\pi k dk\right)$$

Dividing the ring area by the unit cell area, the density of states can be found:

$$g(k)dk = 2\left(\frac{A}{A_0}\right) = (2)\frac{\frac{\pi}{2}kdk}{\left(\frac{\pi}{a}\right)^2} = \frac{a^2}{\pi}kdk \qquad (2.9)$$

The relationship between k and E is:

$$k = \sqrt{\frac{2mE}{\hbar^2}}$$

Then:

$$dk = \frac{1}{2}\left(\frac{2m}{\hbar^2}\right)\left(\frac{2mE}{\hbar^2}\right)^{-1/2} dE = \frac{m}{\hbar^2}\left(\frac{2mE}{\hbar^2}\right)^{-1/2} dE$$

Substituting the results into the density of states equation (2.9) will give the density of states in terms of energy.

$$g(E)dE = \frac{a^2}{\pi}\left(\frac{2mE}{\hbar^2}\right)^{1/2}\left[\frac{m}{\hbar^2}\left(\frac{2mE}{\hbar^2}\right)^{-1/2}\right]dE$$

$$g(E)dE = \frac{a^2 m}{\pi\hbar^2}dE$$

$$g(E) = \frac{a^2 m}{\pi\hbar^2} \qquad (2.10)$$

Equation 2.10 reveals that the conventional 2D density of states, interestingly, does not depend on energy.

2.5 Density of States in Transition Metal Dichalcogenides

The probability of absorbing photons depends on the number of available electronic states. Therefore, to understand how light interacts with 2D-TMDs we need to first understand the density of electronic states (DOS). To find out the density of electronic states *g(E)* in 2D-TMD atomic layer semiconductors we use the energy spectrum (shown in Figure 2.8) calculated theoretically through effective tight-binding two-valley Bloch Hamiltonian[21,22,23]:

$$E_{\tau S}^{n}\left(k\right)=\frac{1}{2}\left(\lambda\tau S+n\sqrt{\left(2atk\right)^{2}+\left(\Delta-\lambda\tau S\right)^{2}}\right) \tag{2.11}$$

Here, Δ is the band gap energy, 2λ is the spin splitting in the valence band, the valley index $\tau=\pm1$ corresponds to $\pm K$ points, and the spin index $s=\pm$ corresponds to the z-component of the spin. $n=\pm1$ indexes the conduction and valence band, respectively. We note here that the energy spectrum is hyperbolic; $E(k)$ is approximately parabolic at low energies but tends towards a constant linear slope at high electron energies.

The density of states in 2D-TMDs can be calculated directly from equation 2.11 and is given by:

$$g\left(E\right)=\frac{1}{2n\pi a^{2}t^{2}}\left(\frac{2E-\lambda\tau S}{n}\right)=\frac{2E-\lambda\tau S}{2n^{2}\pi a^{2}t^{2}} \tag{2.12}$$

The density of electronic states in the conduction band ($n=1$) can be written as:

$$g\left(E\right)=\frac{1}{\pi a^{2}t^{2}}\left(E+E_{GAP}\right)=\frac{E_{GAP}}{\pi a^{2}t^{2}}\left(1+\frac{E}{E_{GAP}}\right) \tag{2.13}$$

Here, E_{GAP} is the energy difference between the conduction and valence band in the *K*

and *K'* valleys of a monolayer TMD, such as $MoSe_2$ or WSe_2. From equation 2.13, the density of states approaches a constant value for electrons near the bottom of the bands, but depends linearly on the electron energy at high energies. Comparing this to equation 2.10, we note that this result is distinct from the density of states in conventional 2D electron gases, where *g(E)* does not depend on energy due to parabolic band structure.

Calculating the density of available electronic states is important to understand the electron transport through the interface of the heterostructure. Density of states being linearly proportional to energy for this type of 2D atomic layer system forms a completely different *I-V* characteristic from conventional semiconductor P-N junctions (formulation represented in chapter 6).

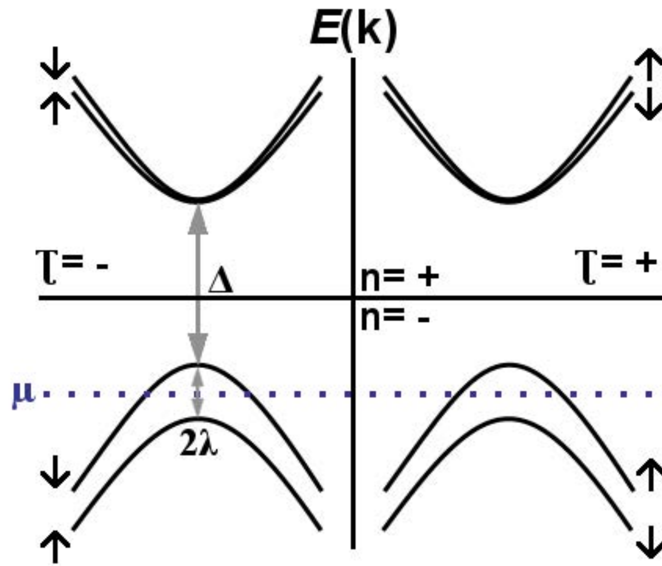

Figure 2.8. Energy band diagram of a 2D-TMD material with hyperbolic band structure.

REFERENCES

1. Choi W., et al. Recent development of two-dimensional transition metal dichalcogenides and their applications. *Materials Today*, **20**, 116-130 (2017).

2. Liu G. B., et al. Electronic structures and theoretical modeling of two-dimensional group-VIB transition metal dichalcogenides. *Chem Soc Rev*, **44**, 2577-2788 (2015).

3. Zhang Y. J., et al. 2D crystals of transition metal dichalcogenide and their iontronic functionalities. *2D Mater*. **2**, (2015).

4. Silva Guillen J. A. et al., Electronic Band Structure of Transition Metal Dichalcogenides from Ab Initio and Slater–Koster Tight-Binding Model. *Appl. Sci.* **6**, 284 (2016).

5. Kresse, G. & Furthmüller, J. Efficient iterative schemes for ab initio total-energy calculations using a plane-wave basis set. *Phys. Rev. B* **54**, 11169-11186 (1996).

6. Kresse, G. & Hafner, J. Ab initio molecular dynamics for liquid metals. *Phys. Rev. B* **47**, 558-561 (1993).

7. Kresse, G. & Furthmüller, J. Efficiency of ab-initio total energy calculations for metals and semiconductors using a plane-wave basis set. Comput. *Mater. Sci.* **6**, 15-50 (1996).

8. Blöchl, P. E. Projector augmented-wave method. *Phys. Rev. B* **50**, 17953-17979 (1994).

9. Perdew, J. P. et al. Atoms, molecules, solids, and surfaces: Applications of the generalized gradient approximation for exchange and correlation. *Phys. Rev. B* **46**, 6671- 6687 (1992).

10. Wang, Y. & Perdew, J. P. Correlation hole of the spin-polarized electron gas, with exact small-wave-vector and high-density scaling. *Phys. Rev. B* **44**, 13298-13307 (1991).

11. Kresse, G. & Joubert, D. From ultrasoft pseudopotentials to the projector augmented- wave method. *Phys. Rev. B* **59**, 1758-1775 (1999).

12. Harl, J., Schimka, L. & Kresse, G. Assessing the quality of the random phase approximation for lattice constants and atomization energies of solids. *Phys. Rev. B* **81**, 1151261-11512618 (2010).

13. Horzum, S. et al. Phonon softening and direct to indirect band gap crossover in strained single-layer MoSe2. *Phys. Rev. B* **87**, 1254151-1254155 (2013).

14. Brixner, L. H. Preparation and properties of the single crystalline AB2-type selenides and tellurides of niobium, tantalum, molybdenum and tungsten. *J. Inorg. Nucl. Chem.* **24**, 257–263(1962).

15. Bhattacharyya, S. & Singh, A. K. Semiconductor-metal transition in semiconducting bilayer sheets of transition-metal dichalcogenides. *Phys. Rev. B* 86, 0754541-0754547 (2012).

16. Tongay, S. et al. Thermally driven crossover from indirect toward direct bandgap in 2D semiconductors: MoSe2 versus MoS2. *Nano Lett.* **12**, 5576-5580 (2012).

17. Sahin, H. et al. Anomalous Raman spectra and thickness-dependent electronic properties of WSe2. *Phys. Rev. B* **87**, 1654091-1654096 (2013).

18. Zhang, Y. et al. Direct observation of the transition from indirect to direct bandgap in atomically thin epitaxial MoSe2. *Nat. Nanotechnol.* **9**, 111-115 (2014).

19. Zhang, Y. et al. Electronic structure, surface doping, and optical response in epitaxial WSe2 thin films. *Nano Lett.* **16**, 2485-2491 (2016).

20. Datta, S., *Electron Transport in Mesoscopic Systems*. (Cambridge university Press, *Cambridge, 1995).*

21. Sosenko, E., Zhang, J., Aji, V. Superconductivity in transition metal dichalcogenides. *arXiv* **2**, 1512.01261 (2016).

22. Xiao, D., Liu, G., Feng, W., Xu, X. & Yao, W. Coupled spin and valley physics in monolayers of MoS2 and other group-VI dichalcogenides. *Phys. Rev. Lett*. **108**, 1968021-1968025 (2012).

23. Xu, X., Yao, W., Xiao, D. & Heinz, T. F. Spin and pseudospins in layered transition metal dichalcogenides. *Nat. phys.* **10**, 343-350 (2014).

CHAPTER 3

DEVICE FABRICATION & TRANSPORT MEASUREMENTS OF *2L*-WSe_2/$MoSe_2$

3.1 Introduction

The devices studied in this thesis consist of two types of group-VI transition metal dichalcogenides known as tungsten diselenide (WSe_2), and molybdenum diselenide ($MoSe_2$). We start this chapter by carefully reviewing the wafer preparation procedure, and then introduce the scotch and blue tape-based micromechanical exfoliation technique. Afterwards, we explicitly illustrate the dry transfer method for assembling the individual layers and building the van der Waals heterostructures, and finally present the device fabrication tools and techniques.

3.2 Wafer Preparation

Two-inch Si wafers coated with 290 nm thick SiO_2 with crystal planes of (100) are used as substrates for preparing devices. We cut these wafers into small pieces with dimensions less than 1cm x 1cm to exfoliate thin layers on them. The dimension of the exfoliated flakes is of the order of tens of microns; so we need a way to mark the position of them on the substrate and be able to find them easily. We pattern a mask of two dimensional arrays that covers the whole area of the Si wafers through photolithography, cleave the wafers, and clean them before using them for exfoliation and device fabrication. The procedure for cleaning wafers is summarized below:

1. First cleaning: rinse wafer with acetone and isopropyl alcohol (IPA).
2. Spin coating photoresist: cover the surface with two layers of hexamethyldisilazane (HDMS) and a positive resist of AZ5214.
3. Bake the wafer in 110 °C for 5 minutes.
4. Photolithography to pattern the mask on the surface of the wafer, we used Karl Suss Mask Aligner with 1 micron resolution, we generally expose the samples for 16 seconds with ultra-violet light.
5. Develop them with a combination of one part of AZ 400K developer and four parts of DI water for one minute and then dry them with nitrogen gas.
6. The patterned wafers then need to get etched. We use Reactive Ion Etch (RIE) system at the Center for Nanoscale Science & Engineering with the rate of 20 μm/min for 2 minutes.
7. Lift off the resist with acetone pressure.
8. Once wafer is patterned, we then slice it into very small pieces.
9. Clean them through acetone sonication and finally rinse them in acetone and IPA.

Wafers are now ready for exfoliation, transferring and then device fabrication.

3.3 Exfoliation

We fabricated $MoSe_2$/*2L*-WSe_2 heterostructures by mechanical exfoliation of WSe_2 and $MoSe_2$ flakes from bulk crystals (2D Semiconductor) onto Si wafers coated with 290 nm-thick SiO_2. There are two types of tapes that can be used for micromechanical exfoliation of atomic layered materials, scotch tape and silicone-free

adhesive plastic film (blue tape). Scotch tape is good for exfoliation of graphene and hexagonal boron nitride, for which you can take advantage of the strong adhesion of the tape to repeat the peeling off process successively. Blue tape instead is very appropriate for exfoliation of transition metal dichalcogenides; lower amount of adhesion is sufficient to avoid tearing the layers apart into smaller flakes and at the same time reduce the number of layers by peeling it off.

There are several steps for exfoliation with blue tape that makes exfoliation more efficient:

1) Take a piece of crystal and place gently on the tape (tape #1).

2) Take another piece of tape (tape #2) and lay this tape on the tape#1 parallel, gently press with your fingers.

3) Peel the pieces of tape off from each other, and repeat the last step over and over to have a tape dappled with spots (unlike graphene and h-BN don't spread it out by exfoliating spots with flakes on top of each other, it will tear the flakes off), now you have two pieces of tape, each of which can be used for exfoliating atomic layers of TMDs onto SiO_2/Si wafers. In general, we keep #1 for later and start using #2, the result of this process is shown in figure 3.1a.

4) Carbon-tape the back of a Si wafer down to a clean glass slide that is also taped down to the workstation.

5) Place tape #2 gently on Si wafer and let it adhere; do not touch the surface of

the tape for more adhesion.

6) These dapples will be like islands and because of their thickness there will be a few bubbles created between them, and around this area will be tape in contact with wafer due to adhesion, shown in figure 3.1 b, and c.

7) Exfoliate tape from wafer in such a way to have control over moving the bubble through them, depicted in figure 3.1d.

8) Take the wafer apart from glass slide using a clean razor. In general exfoliation methods produce flakes with different sizes and thicknesses randomly distributed over the surface of the substrate, and only a small fraction of these flakes are atomically thin. With this method we get at least a few monolayer, bilayer flakes at each trial. Optical images of a few exfoliated bilayers of WSe_2 and monolayers of $MoSe_2$ are shown respectively in figure 3.2 a and b.

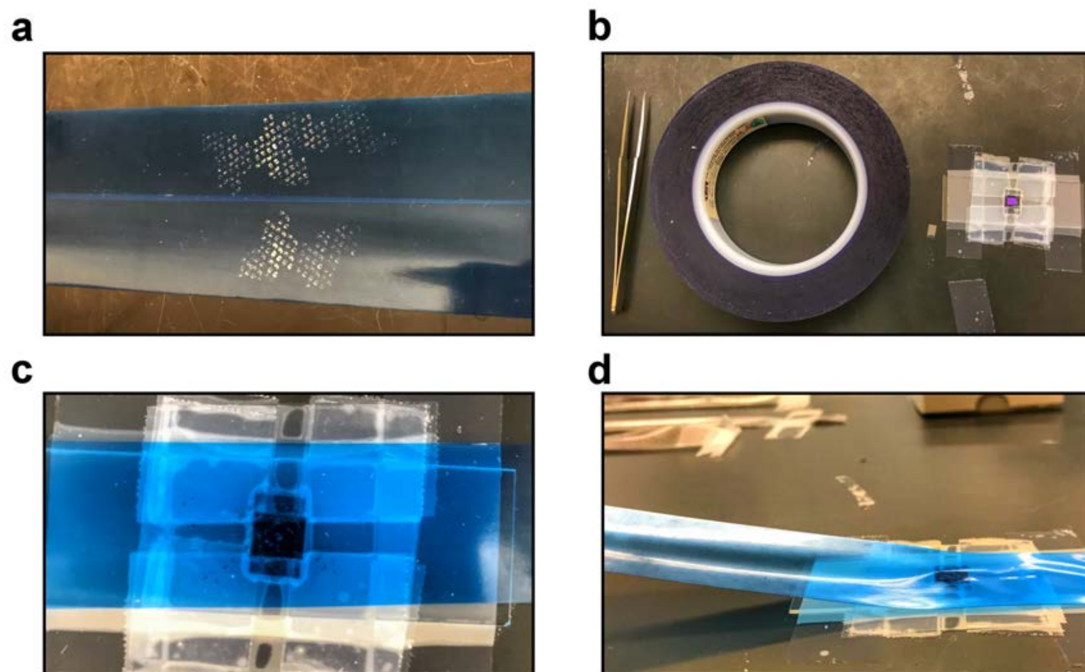

Figure 3.1. Exfoliation process. a, Tapes #1 and #2 ready for exfoliation. b, Tweezers, blue tape and a small Si wafer carbon taped from underneath to a glass slide. c, Closer view of tape on wafer. d, Exfoliation of the tape from the wafer, showing the small angle.

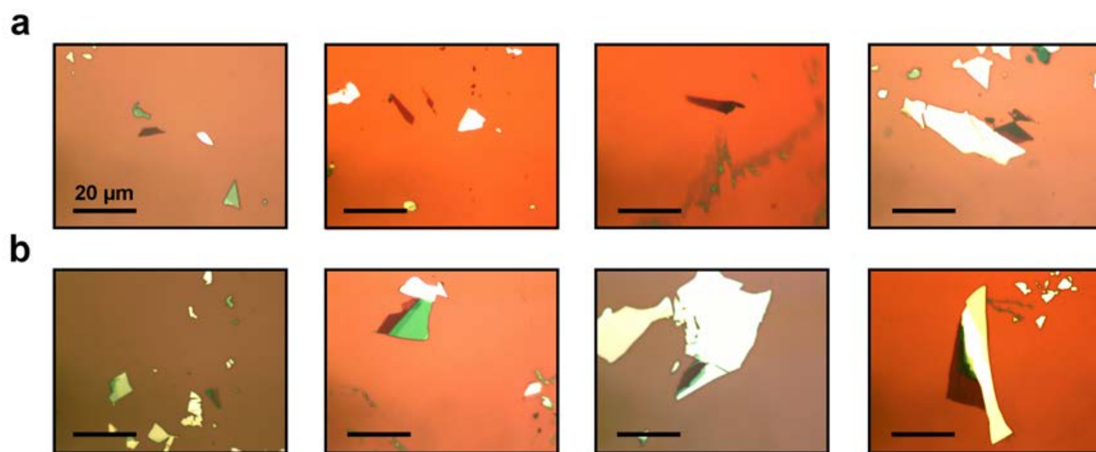

Figure 3.2. Optical images of a few exfoliated layers of WSe_2, and $MoSe_2$ respectively in a and b, scale bars are 20 µm.

3.4 Stacking 2D-TMD Atomic Layers

The heterostructure devices are assembled using a highly customized, temperature-controlled transfer microscope that ensures that the interface between the two layers has no intentional contact to polymer films. The dry pick-up transfer process, described below, results in heterostructures with minimal interfacial contamination, and is followed by two annealing processes. The van der Waals pick-up and transfer process is based on Andres Castellanos-Gomez technique[1], and is represented schematically in Figure 3.4 to highlight key distinctions of this work.

The microscope shown in figure 3.3a consists of a sample stage where the target layer will be placed, objectives with different magnifications to monitor the process, and stamping stage that holds the glass slide with an attached viscoelastic stamp. Figure 3.3b shows a schematic of a stacked bilayer of WSe_2 on a monolayer of $MoSe_2$.

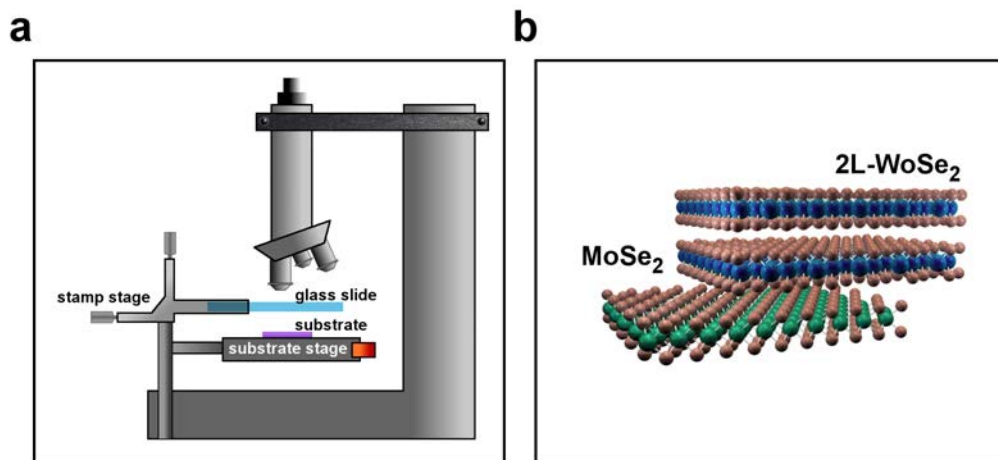

Figure 3.3. a, Transfer microscope with constituent components. b, A stacked heterostructure that is made using this microscope.

To achieve this, we first use a stamp to pick up the target layer, (Fig. 3.4a, top). The stamp mounted in a micromanipulator consists of a layer of polydimethylsiloxane (PDMS) adhered to the top of a glass slide and a thin layer of polypropylene carbonate (PPC) spin coated on top of it. The stamp is lowered until the PPC contacts the first target layer, WSe_2. We then heat the stage to 40° C. Next, we let the stage to cool off to 34° C and very quickly lift the stamp up, as shown in Figure 3.4b (top).

To assemble the heterostructure, we lower the WSe_2 flake and place it on to the $MoSe_2$ flake on the stage as shown in Figure 3.4c (top). The stamp is transparent, and we can see through it and align the orientation of the two flakes with sub-micrometer resolution with respect to each other using the XY knobs of the translation stage on the rotatable sample stage. The stage is then heated to 80° C, to begin melting the PPC which then adheres strongly to the surface. The stamp is then lifted very slowly, causing the PPC to separate from the PDMS. This leaves the stack of two flakes with PPC on top. We then remove the residual PPC using acetone. Figure 3.4 (a, and b), bottom, show optical images of the resultant exfoliated flakes of WSe_2 and $MoSe_2$. Dashed lines highlight the individual layers and overlapped region of the heterostructure.

The working principle of the transfer is based on the viscoelasticity: the stamp behaves as elastic solid at short timescales while it can slowly flow at long timescales. Flakes are adhered to its surface because the viscoelastic material gets into close contact with the flakes. By slowly peeling off the stamp from the surface, the viscoelastic material detaches, releasing the flakes that adhere preferentially to the acceptor surface.

The stamping method can be also applied to transfer two-dimensional crystals onto pre-fabricated devices with trenches and electrodes.

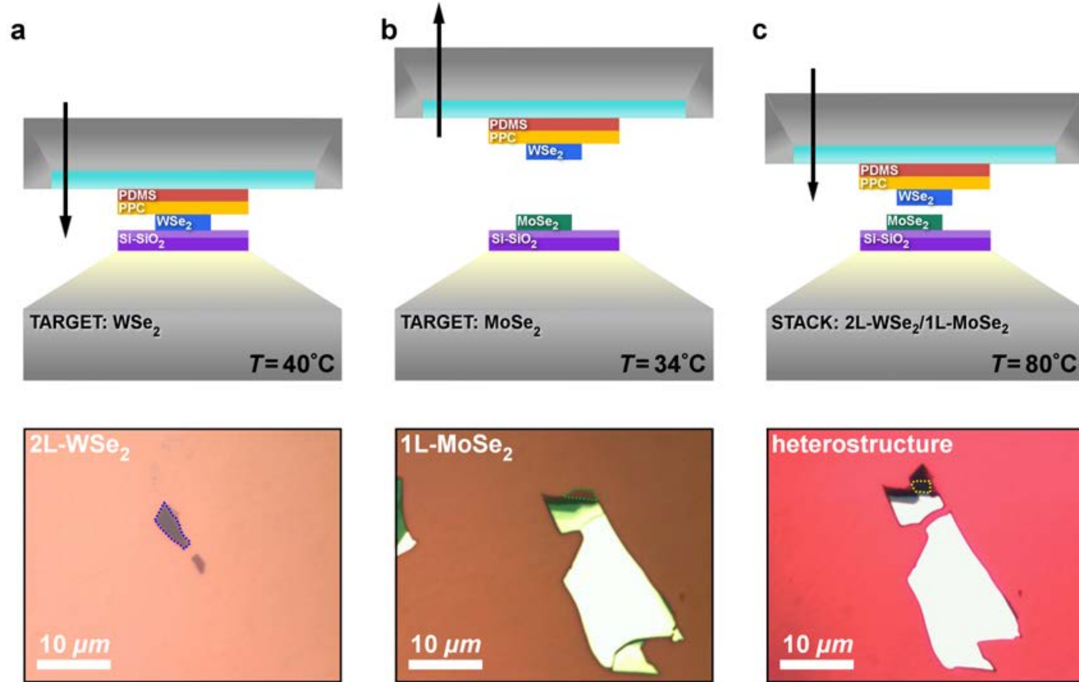

Figure 3.4. Schematic illustration and optical images of the dry-transfer process. a, b, c, (top), Schematic illustration of the transfer microscope at different temperatures for different purposes. a, b, c, (bottom), Optical images of exfoliated flakes of WSe_2, $MoSe_2$, and $MoSe_2$/*2L*-WSe_2 heterostructures respectively. Dashed lines indicate the area of the individual layers and the overlapped region, which are about 14μm^2, 8μm^2, and 4.3μm^2 respectively from left to right.

3.5 Device Fabrication

Electrical contacts on the heterostructures are patterned by either electron-beam lithography or focused ion-beam lithography and deposited by electron-beam evaporation of Ti/Au (5nm adhesion layer /150 nm) for electrodes on each layer and on the

overlapped region as well. A focused beam of electrons or ions scans over the surface of the substrate and exposes custom patterns on the electron/ion sensitive resist film (MMA/PMMA) with ultra-high resolution.

High vacuum deposition is then used to deposit metal onto the e-beam defined pattern. Figure 3.5a (left to right), shows several heterostructures made by transferring flakes of figure 3.2a to b respectively. Figure 3.5b illustrates fabricated devices of figure 3.5a using EBL and E-Beam evaporation. Figure 3.6 shows optical images of the second device from figure 3.5b in different objectives magnifications. From left to the right the images are taken with 5x, 10x, 20x, 50x, and 100x objectives respectively.

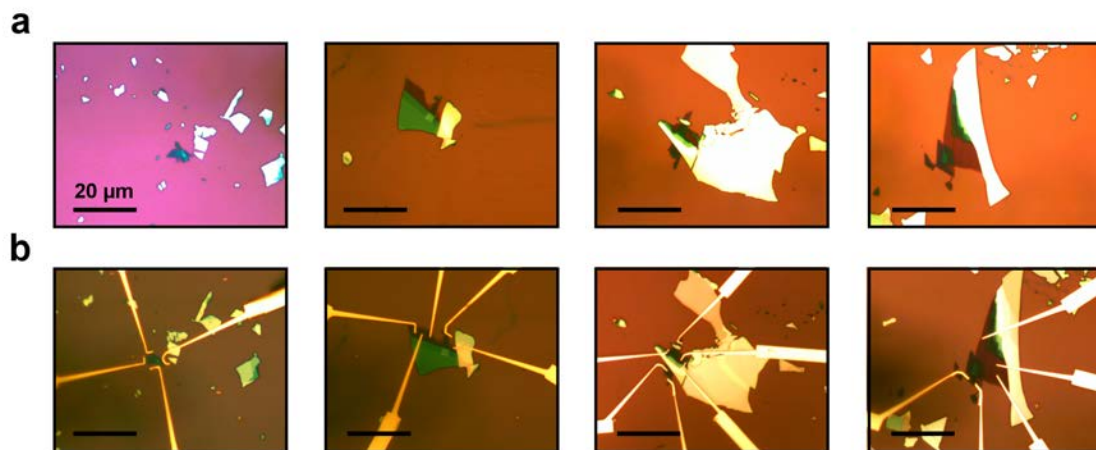

Figure 3.5. a, Heterostructures made from flakes of figure 3.2 a and b. b, Heterostructures from part a with written electrodes, scale bars are 20 µm.

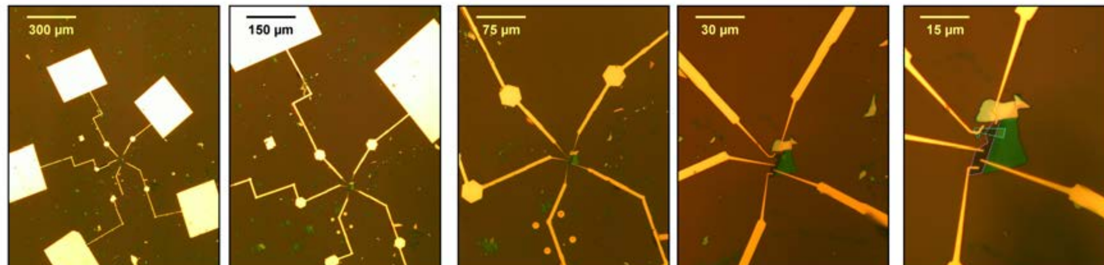

Figure 3.6. Optical images of a fabricated device with different magnifications from 5x to 100x.

REFERENCES

1. Castellanos-Gomez, A. et al. Deterministic transfer of two-dimensional materials by all- dry viscoelastic stamping. *2D Mater. Lett.* **1**, 1-8 (2014).

CHAPTER 4

INSTRUMENTATION: LOW TEMPERATURE BROADBAND PHOTOCURRENT SCANNING MICROSCOPE

4.1 Introduction

It was after the discovery of graphene by Andrew Geim and Noveselov that scientists found interest in numerous other layered materials. One important family of two-dimensional materials is the family of transition metal dichalcogenides (TMDs). In their bulk form, TMDs have been studied for decades owing to their wide range of electronic, optical, mechanical, chemical and thermal properties. More recently, as these materials have been isolated into ultrathin films, optoelectronics experiment techniques have proven great tools for exploring quantum mechanical electron and phonon behavior. In this chapter, we discuss a novel optoelectronic probe designed to study this new family of materials and their heterostructures.

4.2 Light-Matter Interaction at the Nanoscale

Interaction between light fields (electromagnetic radiation) and matter at the nanoscale is a growing subject of research due to the increasing interest in the novel phenomena that occurs as a result of this interaction. Classically, light-matter interactions are a result of an oscillating electromagnetic field resonantly interacting with charged particles. In the quantum view, light fields will act to couple quantum states of the matter. As a practical basis for studying light-matter interactions, semiconductor based

optoelectronics is a field that has attracted a lot of attention both experimentally and theoretically. In this chapter, we present the optoelectronic instrumentation needed to explore quantum phenomena in nanoscale semiconductors. In later chapters, we then present experiments that use these techniques to explore optoelectronic gain due to hot carrier impact excitation and anti-Stokes absorption for applications in laser cooling of TMD based semiconductor devices.

4.3 The Supercontinuum Scanning Photocurrent Spectroscopy Microscope

Supercontinuum scanning photocurrent spectroscopy microscope (SSPSM) is a powerful tool designed to explore quantum optoelectronic properties of atomic scale devices by integrating optics and electronics into a combined quantum transport microscope. The SSPSM is equipped with a helium flow optical cryostat that enables both electrical access and optical illumination to nanoscale devices through its electrical feedthroughs and a transparent window. This cryostat can create a low-pressure environment via a turbo pump system and can be cooled down to helium temperatures T = 4 K.

For optical illumination a collimated beam of light is introduced to the back aperture of an objective through optical and optomechanical components of the microscope, generating a diffraction limited beam spot that can be scanned over the nanoscale device. The resulting current is recorded to form a spatial map of photocurrent. Reflected light from sample is collected by a photodiode detector (PD) converting the

optical power to electrical power (as a photovoltage), and the reflected intensity is monitored to form a simultaneous image of the device.

The SSPSM microscope employs a supercontinuum Fianuim white laser as the light source (discussed in section 4.5.1 of this chapter) along with Princeton Instrument monochromator (see section 4.6.2 for details) for spatially and spectrally resolved supercontinuum excitations. Power dependence experiments are achieved using automated attenuation optics (discussed in 4.6.7).

Figure 4.1 illustrates a schematic diagram of the microscope. Laser light reaches mirror M5 through two different paths: light either passes through the monochromator via the left optical line in yellow, exits from its slit, hits L4 and reaches M5 for spectrally resolved experiments, or using a flip mount mirror FM1 and a periscope (PSC) passes through the right optical line in red and then reaches to the front of the exit slit of monochromator. Light then reaches M5 via the second flip mount mirror (FM2) for power dependence measurements. Laser light reflecting from M5 generates a diffraction limited beam spot by passing through different optical components. In the following, we give a highly detailed description of the integrated system that combines electronic and optical tools to study nanoscale devices.

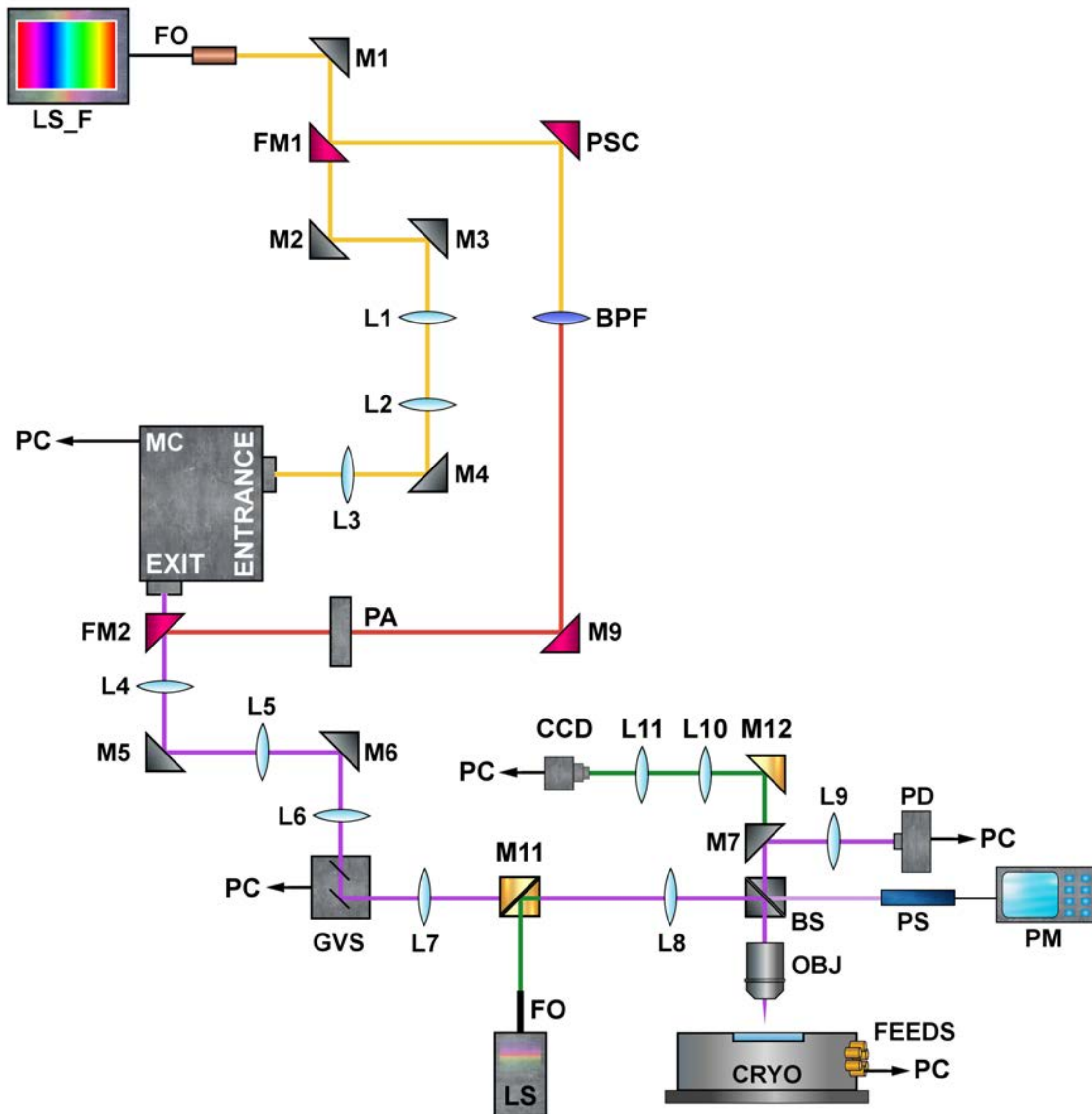

Figure 4.1. Schematic diagram of the supercontinuum scanning photocurrent spectroscopy microscope (SSPSM). Constituent components of the microscope comprise: light source of Fianium (LS_F), FO (fiber optics), monochromator (MC), mirrors (M), lenses (L), flip mount mirrors (FM), galvos system (GVS), beam splitter (BS), objective (OBJ), power sensor (PS), power meter (PM), photodiode detector (PD), CCD camera (CCD), cryostat (CRYO), PSC (periscope), band pass filter (BPF). Electronic experiments are conducted through the optical CRYO, while optical illumination is introduced via OBJ to devices.

4.4 Electronic Transport Experiment Instrumentation

A Helium flow optical cryostat is used to combine electrical measurements and optical illumination on devices. In this section we'll first present its application as a probe station that enables electronic transport measurements on samples with the assistance of several other pieces of equipment. In the next section, we describe the integration of optical illumination to perform optoelectronic experiments.

The optical cryostat has a sample holder at the center where the sample is mounted, surrounded by ten electrical contacts for electronic manipulation. The sample is

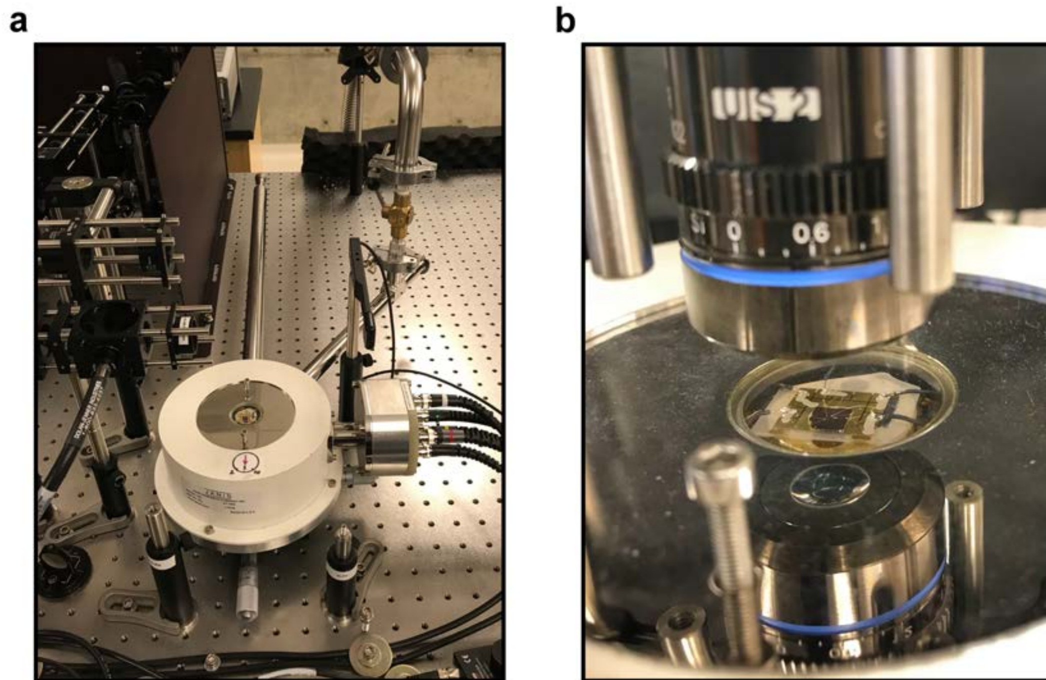

Figure 4.2. a, Photograph from the optical cryostat, a few BNC cables are connected to feedthroughs from right that are internally connected to the device, and two arms for vacuum pump and He transfer. b, A zoomed in view of a device in the cryostat under the microscope objective that introduces light from top to the sample, device is under vacuum.

separated from the outside environment by a 25.4 mm clear view epoxy sealed quartz window for optical illumination in high vacuum. The distance between the sample holder and the window is about 3mm, a typical working distance for many microscopic objectives. The ten internal electrical contacts have output pin feedthroughs outside the chamber providing electrical access to the device.

Figure 4.2a depicts a photograph from optical cryostat; the BNC cables are connected to feedthroughs of the cryostat for electrical access to device. A zoomed in view of the device under the microscope objective is shown in figure 4.2b. The objective introduces a collimated laser light from top to the sample for optical illumination presented in section 4.6.

Using a turbo pumping station, the chamber is evacuated to a pressure of 10^{-6} mTorr through an evacuation port located on the left arm in figure 4.2. A Si diode temperature sensor along with a 50 Ω heater ring located at the base of the cryostat is coupled to an external temperature controller. It can control and vary the temperature between 4-360 K. Temperature control can be mediated also by regulating the helium flow through He delivery line (the left arm in figure 4.2). A continuous flow of He through the delivery line and cooling the metal base underneath the sample holder will cool the sample to temperatures close to 4 K.

The electronic contact pads of devices on Si substrates are wire bonded to the conductive pads (Ti/Au: 10/150 nm) of the chip carrier (a patterned substrate of sapphire) using a wire-bonding machine. Figure 4.3a shows wire connections between device pads

and the chip carrier. After wire bonding, devices are soldered to the electronic pads of the cryostat and silver painted for further electronic experiments shown in figure 4.3b.

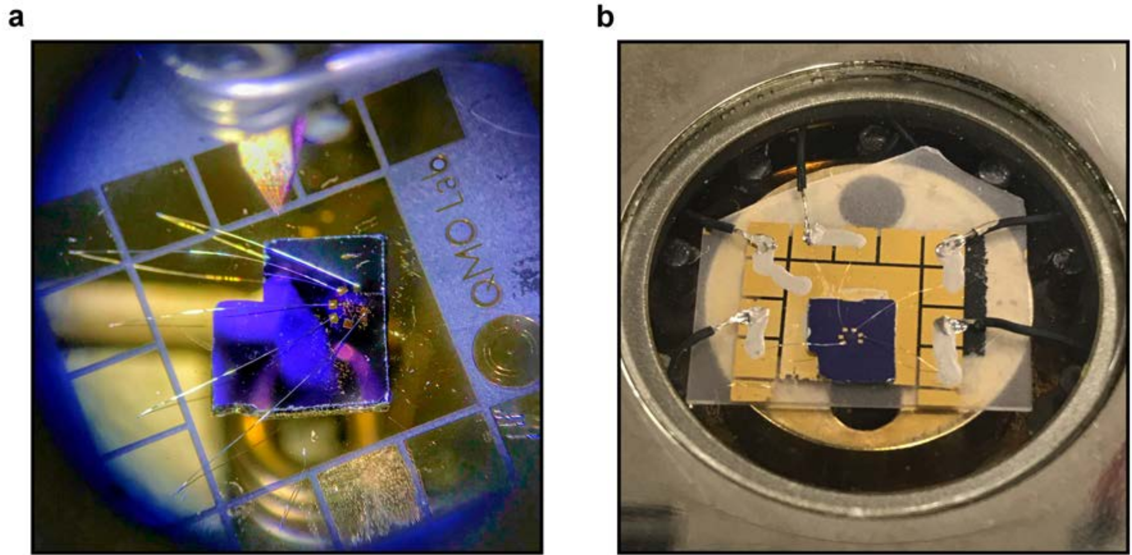

Figure 4.3. a, Photograph of wire bonding the electrical pads of the device to contact pads of the chip carrier. b, Photograph of soldering chip carrier to electrical pins of the cryostat.

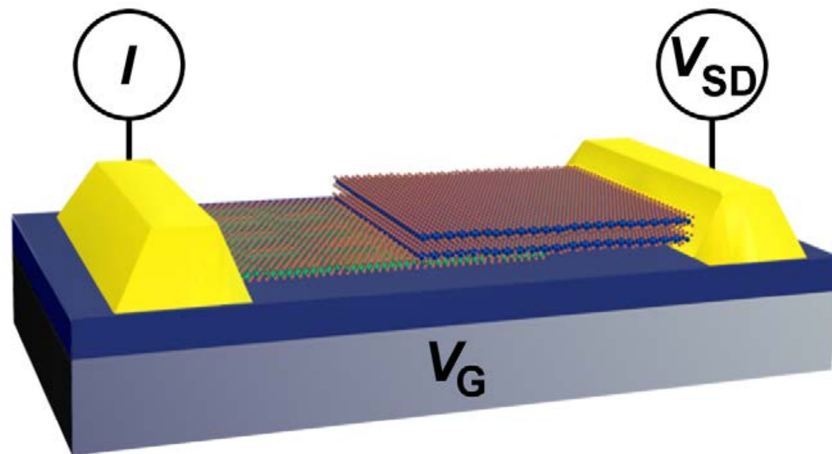

Figure 4.4. Schematics of the atomic layer device, arrangement of the layers, and the electrical contacts configuration.

Transport measurements are performed through the electrical configuration of the device shown in figure 4.4, where source-drain voltage is applied to one layer and the interlayer electrical current collected from the other while having an underneath back gate of Si/SiO_2.

All experimental parameters can be controlled though labview or a python based software (discussed in section 4.6.6). Figure 4.5 shows a photograph of a high voltage amplifier (Falco System WMA-100), current preamplifier (DLinstruments), switch box, and two sets of DAQs respectively from top to bottom, with electrical connection configuration. The two outputs of DAQ#1, labeled AO0 (in red), and AO1 (in blue) provide input voltages for source-drain and gate respectively. A BNC cable connects AO0 to mount #2 (top) on the switch box while mount #2 (bottom) serves as the source-drain voltage probe used to apply voltage to one of the layers of the heterostructure.

The electrical device response must be analyzed and studied; Data Acquisition Hardware (DAQ) supplies the input voltage and interfaces between the voltage/current signal and the computer by converting the signal into digital values.

A grounded switch box allows physical connection between DAQ output channels and the current/voltage probes, these probes transport electrical signal from DAQ output channels to device and from device to computer via DAQ input channels.

In most devices, a Si/SiO_2 back gate is designed to tune the carrier concentration by electron and hole doping of the TMD heterostructures. Typically, a high voltage of up to ±50 V is needed for the type of the heterostructures under the study of this thesis. It can be achieved by incorporating a high voltage amplifier before the gate probe output.

The amplifier multiplies the signal taken from AO1 shown in figure 4.5 for the gate voltage probe.

An Ithaco DL current preamplifier (Model 1211 with option 10) is used to convert the electrical signal taken from the device into an output signal with a strong signal to noise ratio by collecting the interlayer current from the heterostructure and transforming the signal to the input channel of DAQ#2 (Ai17).

BNC cables from the cryostat feedthroughs can be plugged into the switch box mounts labled 3-10 (bottom row), while V_{SD} (in red), V_G (in blue), and I (in purple) probes can make the connection to device through the top row. AO2, AO3, and Ai16 connections from DAQ#2 represented in section 4.6.6.

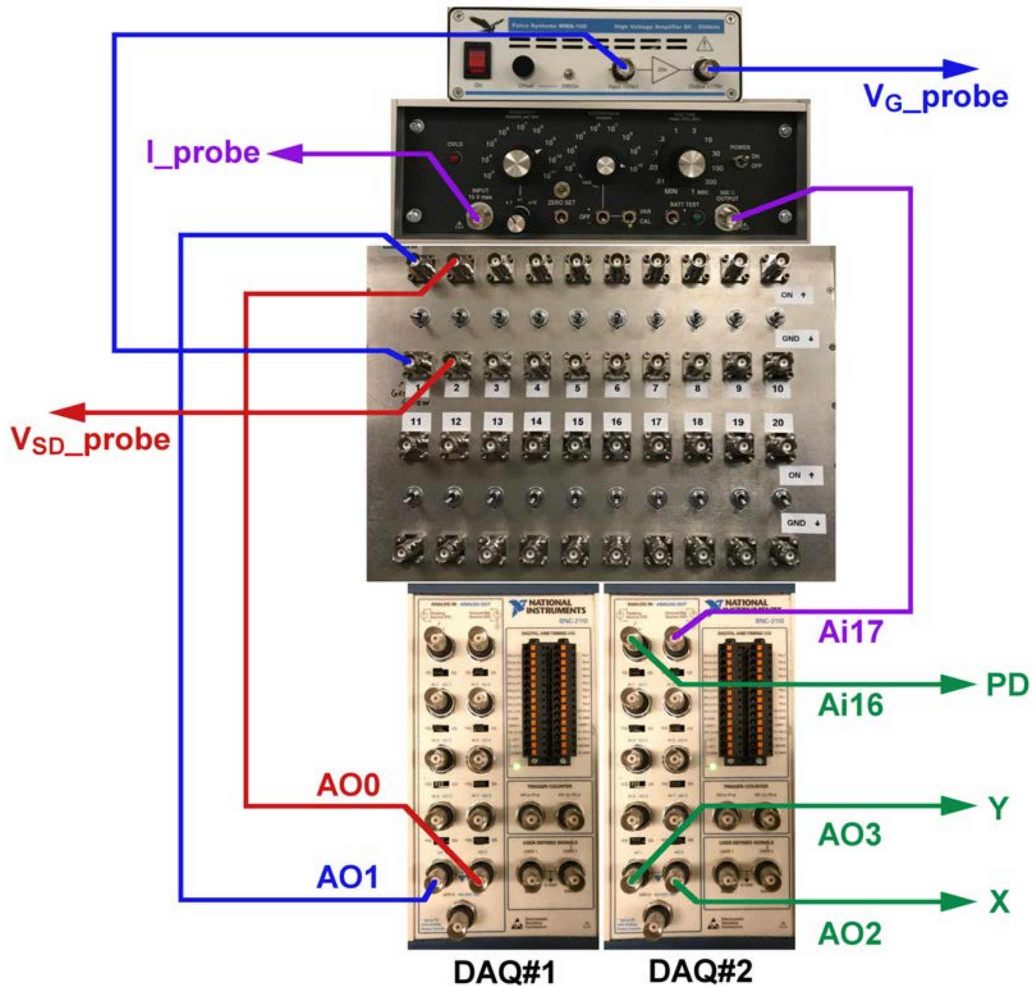

Figure 4.5. Photographs and the electrical circuit diagram of the equipment used for electronic experiments.

4.5 *Optical Imaging Microscopy Instrumentation*

In order to conduct optoelectronic experiments on any device, it first needs to be positioned underneath the laser excitation beam for optical illumination. Here we present a basic optical imaging microscopy technique designed to position the devices prior to optoelectronic experiments. A fiber optic illuminator (115 V, MI-150 fiber optic

illuminator w/IR Filter and Holder) with quartz halogen lamp is used as the light source to illuminate the sample.

Figure 4.6 illustrates schematics of the optical microscope in which the divergent beam of light source gets collimated by passing through a lens (VIS-NIR 100 mm), and then reaches a dichroic mirror. Dichroic Mirrors/Beamsplitters spectrally separate light by transmitting and reflecting light as a function of wavelength. Here we use a 950 nm dichroic longpass filter, which is highly reflective below the cutoff wavelength and highly transmissive above it. This filter reflects light shorter than 950 nm towards the sample, and passes light longer than that emitted from the sample directly towards the detection, so we won't detect the scattered light caused by reflected light. The transmitted light from dichroic mirror passes through two lenses of 75 mm and 30 mm to reduce the image size and become compatible with the screen dimension of the CCD camera (EO-3112C ½" CMOS Color USB Camera).

Figure 4.7a shows the schematic of the optical imaging microscope taken from figure 4.1 and a photograph taken from the actual microscope is illustrated in part b of figure 4.7. Fiber optics (FO) attached to a cage mount introduces light to the system.

Light reflects from mirror M11 (also coupled to the same cage mount with 45-degree rotation) towards a lens (L8=100 mm) for collimation. Collimated light hits the dichroic mirror (DM); it reflects wavelengths above 950 nm down to the sample after passing through an objective (OBJ= Olympus, Plan N-10X/0.25).

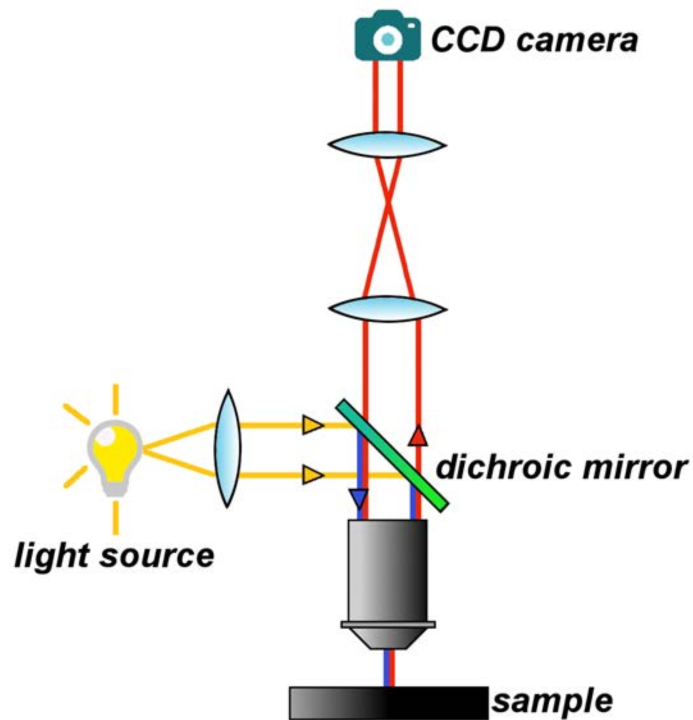

Figure 4.6. Optical imaging microscopy, consisting of a light source, a dichroic mirror, image reducer (a pair lens), an objective, and a CCD camera.

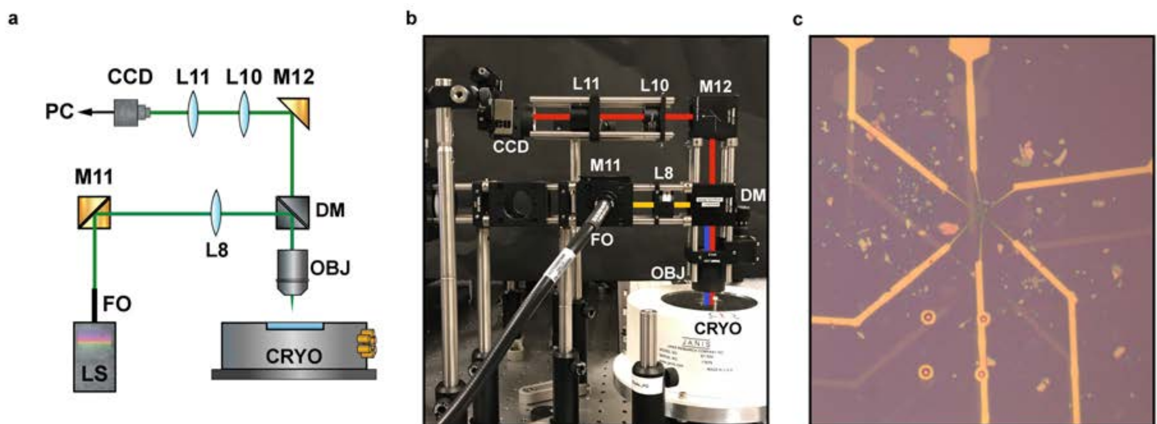

Figure 4.7. a, Schematic of the imaging microscope. b, Optical diagram on a photo of the actual microscope. c, An optical image taken with this optical microscope from a device.

Light in higher wavelengths is then back reflected from sample, passes through DM, and hits the second mirror (M12). The reflected light from M12 passes through two lenses (L10=75 mm, and L11=30 mm) to reduce the image size and eventually reaches a CCD camera that is connected to PC for imaging. Figure 4.7c shows an optical image of a device taken with this microscope.

4.6 Optoelectronic Experiment Instrumentation

Optoelectronic experiments are performed by combining optical illumination along with electronic measurements on the devices mounted in the cryostat. Supercontinuum scanning photocurrent spectroscopy microscope (SSPSM) uses a broadband supercontinuum white laser for the light source, which makes it a unique and powerful experimental technique to investigate spatially and spectrally resolved optoelectronic properties of nanoelectronic devices. In this section we present supercontinuum scanning photocurrent spectroscopy microscope (SSPSM) by dissecting it into its constituent components and explaining each part separately before discussing the assembly of a combined microscope for spatially and spectrally resolved measurements.

4.6.1 Fianium Supercontinuum Ultrafast Fiber Lasers

One of the major components of every optical microscope is the light source; a Fianium supercontinuum is the light source coupled to this microscope for spatially and

spectrally resolved excitations. In optics, a supercontinuum is formed when a collection of nonlinear processes act together upon a pump beam in order to cause severe spectral

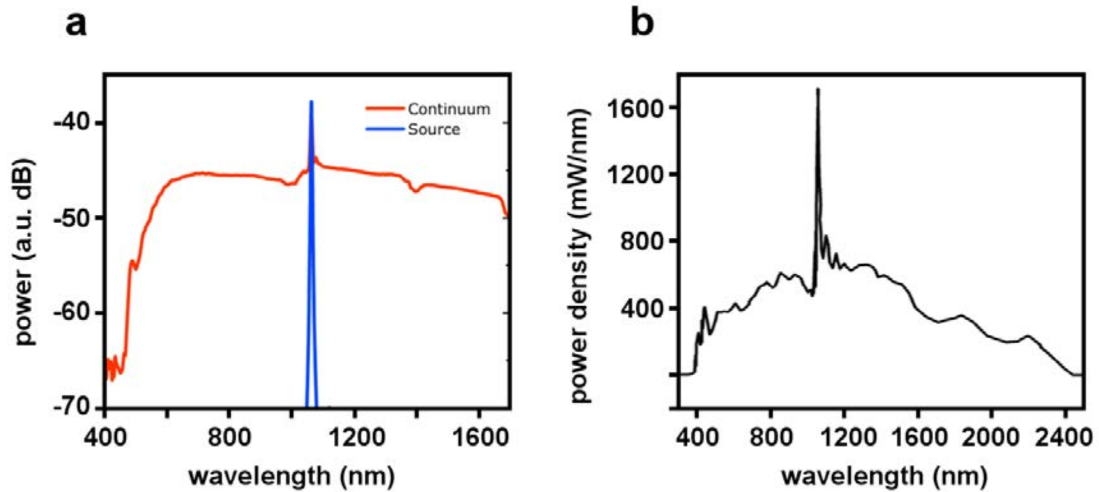

Figure 4.8. a, A typical supercontinuum spectrum in red and the pump pulse in blue, this panel is adapted from reference 2. b, Power dependence supercontinuum spectra of Fianium SC400-8.

broadening of the original pump beam, for instance using a microstructured optical fiber[1]. The result is a smooth spectral continuum.

Figure 4.8a shows a typical supercontinuum spectrum. The blue line shows the spectrum of the pump source launched into a photonic crystal fiber while the red line shows the resulting supercontinuum spectrum generated after propagating through the fiber. The output of these lasers consists of just one wavelength with a combination of these desirable features: high output power, broad and flat spectrum, very broad spectral bandwidth, high degree of spatial coherence that allows tight focusing and the corresponding low temporal coherence, generating ultrafast broadband supercontinuum light[2].

The light source we use for this microscope is a Fianium WhiteLaseTM SC400-8; a picosecond pulsed laser pump (repetition rate = 20 MHz, pulse width = 6 ps) is launched into a micro-structured optical fiber (the non-linear medium) of 1.5-meter length. At the output of the fiber, the collimated white beam of light has an average power of 8 W and a power spectral density of 4 mW/nm that ranges from λ ~ 400-2200 nm, yielding a resolving power of about 3W in the visible range. The Fianium supercontinuum spectrum used for this microscope is shown in figure 4.8b, the pump source is at 1055 nm, as shown from the sharpest peak in the spectrum.

4.6.2 Princeton Instruments Monochromator

In order to spectrally resolve the supercontinuum light, we use Princeton Instruments monochromator (SP-2300). Incoming light at the entrance slit of the monochromator is directly imaged to the exit slit after passing through a diffraction grating (DG1). Figure 4.9 shows schematics of the optical diagram of laser light that passes through different components of the monochromator of the microscope.

There are two micrometer-controlled slits implemented in the monochromator (MC) to adjust their width from 10 μm to 3 mm. These are rectangular apertures through which light enters into and exits from the MC. They control the spectral resolution of the MC by separating close wavelengths.

Light is focused onto the entrance slit and reflected by the first mirror (M1) onto the parabolic collimating mirror (CM). The collimating mirror collimates the light and reflects it directly to the diffraction grating (DG1) in this image. SP-2300 has a triple

grating turret labeled DG1, DG2, and DG3 shown in figure 4.9. Each of them has a specific number of gratings 600, 300, and 150 g/mm respectively with identical blazing wavelength of 1.2 μm. The blaze wavelength is the wavelength for which the blazed grating is most efficient. Diffraction grating disperses the light and spatially separates it into constituent spectral components. In figure 4.9 three colors of purple, green, and red are indicative of diffracted light.

After the diffraction grating, light is re-focused by parabolic focusing mirror (FM) onto the exit slit. Only the particular wavelength that falls directly on the exit slit passes through it and is detected (in diagram of figure 4.9 white light enters the MC and only green passes through the exit slit).

A motorized controller adjusts the angle of the diffraction grating to align the spectrally separated light components towards the exit slit. The width of the exit slit should be adjusted to narrow the output spectral distribution. This controller operates through the Acton Monochromator Control software on a PC. The functions on the software allow changing the gratings, the wavelength, wavelength scanning and the rate of scan, shown in figure 4.10a. Diffraction grating efficiency curves of SP-2300 as a function of wavelength for DG1, DG2, and DG3 respectively are shown in Figure 4.10b. Since the blazing wavelength of our MC is 1.2 μm, the response signal exists between yellow (800 nm-blaze), and red (2 μm-blaze) curves.

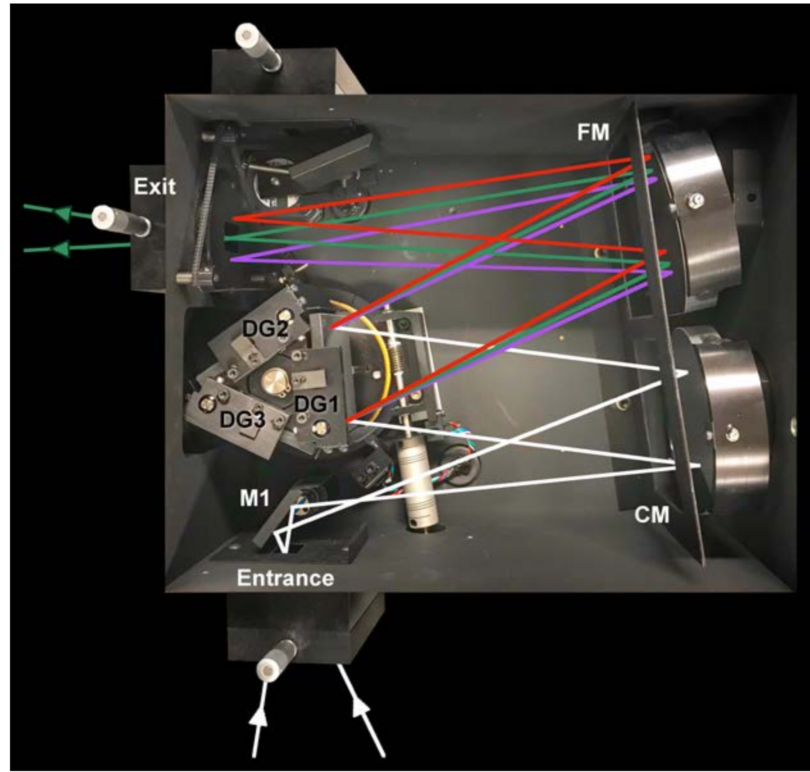

Figure 4.9. Schematics of the ray diagram of SP-2300 monochromator.

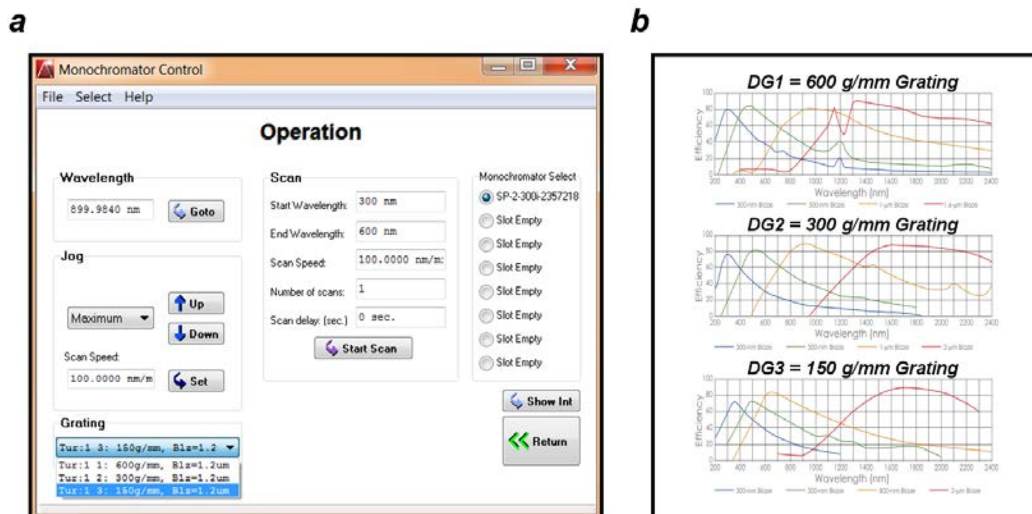

Figure 4.10, a. Monochromator Control Software, b. Grating efficiency curves of SP2300.

4.6.3 Getting Light Into A Monochromator

To achieve the highest optical throughput, we aim to get as much light into the monochromator as possible, regardless of geometry. Each monochromator has an acceptance pyramid, often described by an F/# or numerical aperture (NA). It's a measure of energy throughput, lower F/# means better light gathering power and energy throughput. The position and dimensions of the internal optics determines this pyramid. Usually the pyramid is treated as an acceptance cone with the cone peak on the center of the entrance slit, and the F/# defined by an equivalent circle on the square grating image[3].

In order to reach the maximum achievable performance in coupling a point source laser to a monochromator, we need to collect as much light as possible from the source and focus it on the entrance slit opening at an F/#, which is equal to the monochromator F/#. There are two rules for most efficient coupling; First, we fill the monochromator acceptance cone by choosing a correct F/#. Second, get as much light as possible through the slit while observing the first guideline. The numerical aperture of the lenses we choose to focus light into the entrance slit matches the effective numerical aperture of the monochromator lens system (SP-2300) with *f*/3.9.

Figure 4.11 shows a diagram of the lens system required to introduce light into the MC. The output of the fiber optics is a collimated beam of white light with diameter of d_1= 3 mm. To fill the acceptance cone we need to first expand the laser beam, at least two lenses (L1, and L2) are necessary to accomplish this. In figure 4.11 the laser beam of diameter $d_1$is expanded to $d_2$using a concave lens with focal length $-f_1$ and a convex lens

with f_2.

The numerical aperture of L3 should match the numerical aperture of MC, which gives us $F_{\#MC} = 3.9\ mm = \frac{f_3}{d_3}$ (I), for a collimated light $d_3 = d_2$. The expansion ratio gives $d_2 = \left(\frac{f_2}{f_1}\right) d_1 = \left(\frac{f_2}{f_1}\right) \times 3\ mm$ (II); plugging (I) into (II) defines the relation (III) between the focal length of these three lenses to get the most efficiency out of the SP-2300 MC. $d_2 = \left(\frac{f_2}{f_1}\right) \times 3\ \text{mm} = \frac{f_3}{3.9\ \text{mm}}$, or $\frac{f_3}{11.7} = \frac{f_2}{f_1}$ (III).

The lenses we choose should apply in equation III, and be compatible with the optical elements of the MC. The lenses used in this microscope are inked VIS-NIR achromatic lenses with f_1 = -50 mm, f_2 = 200 mm, and f_3 = 50mm, designed to limit the effects of chromatic and spherical aberration. Inked lenses minimize the stray light within an optical system, while achromatic lenses are corrected to bring two wavelengths (typically red and blue) into focus on the same plane.

Figure 4.12 a, and b show the schematic diagram and photograph of the optical and optomechanical components of the microscope to get light into the monochromator. Light beam coming with diameter of 3mm from the Fianium laser source (LS_F) reflects from first mirror (M1) into a right-angled mirror (M2) that reflects light upward to a height equal to the center of the entrance slit of the monochromator.

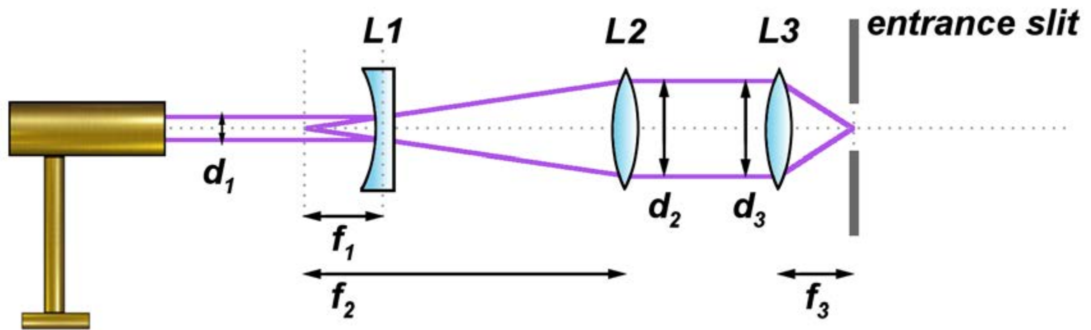

Figure 4.11. Diagram of the lens system required for getting light into the entrance slit of MC.

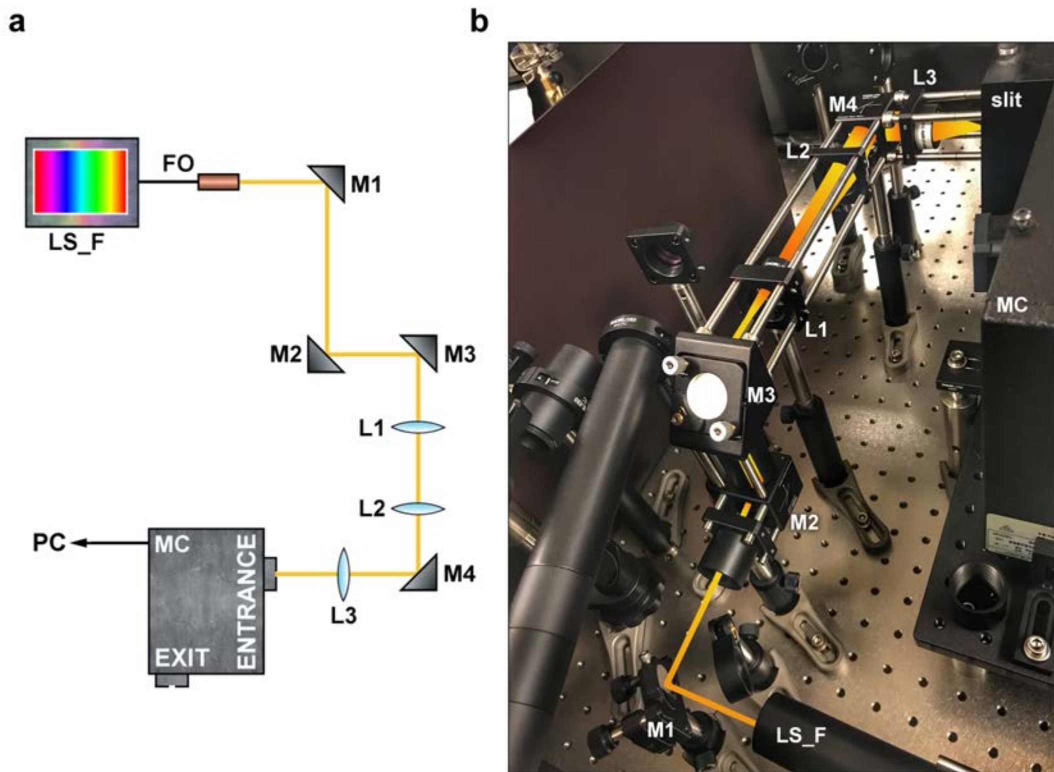

Figure 4.12. Getting light into the MC. a, Schematics of the optics that introduces light into the MC. b, Optical diagram on a photograph of the actual microscope to introduce light to the MC.

The two lenses L1 and L2 with focal lengths of 50 mm and 200 mm respectively, expand the beam diameter to 12.8 mm. Using the third lens L3 with $f_3 = 50$ mm we focus light into the entrance slit with an acceptance cone compatible with the optics of the monochromator, illustrated in figure 12b on the photo.

Mirror mounts M1 and M3 each has a pair of adjusters that allows aligning the beam perfectly along x and y direction. Mirrors M2 and M3 are used as a periscope to transport the laser beam high enough to be able to introduce it to the center of the slit of monochromator. The output power of the optical fiber is 8 W, so we want to keep the fiber height as low as possible close to the surface of the optical table for safety purposes, using a periscope helps to allow this configuration.

4.6.4 Gathering Spectrally Resolved Light Out Of Monochromator

The light cone that leaves the exit slit of the monochromator is the image of the incoming light at the entrance slit. A VIS-NIR inked-achromatic lens (L1) with focal length of 75 mm is well positioned in front of the exit slit to form a collimated beam from the output light cone. The collimated light should then enter the galvos (dual-axis scanning galvanometer mirror positioning system) to form a 2D-spatial scanning beam. Details about the galvos system is explained in section 4.6.5.

Figure 4.13 illustrates the beam that gets out of monochromator and is introduced to the galvos. The diameter (d_1) of the first collimated beam is about 19 mm, which is very large compared to the area of the scanning mirror of the galvos, so a beam reducer is

necessary to decrease its diameter.

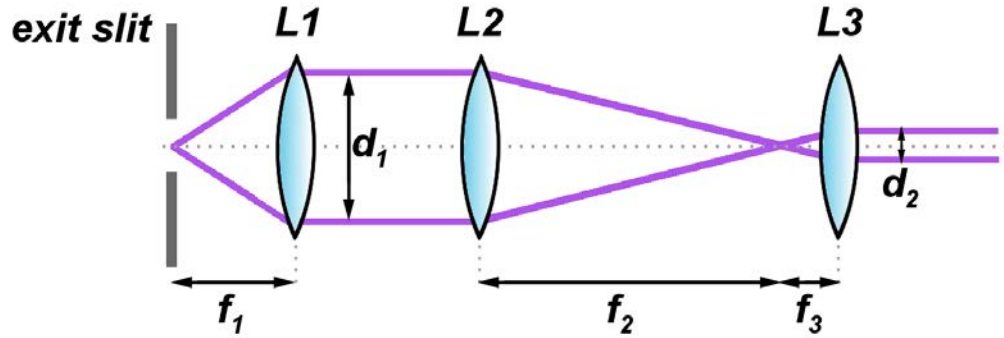

Figure 4.13. Optical diagram for getting light out of the MC.

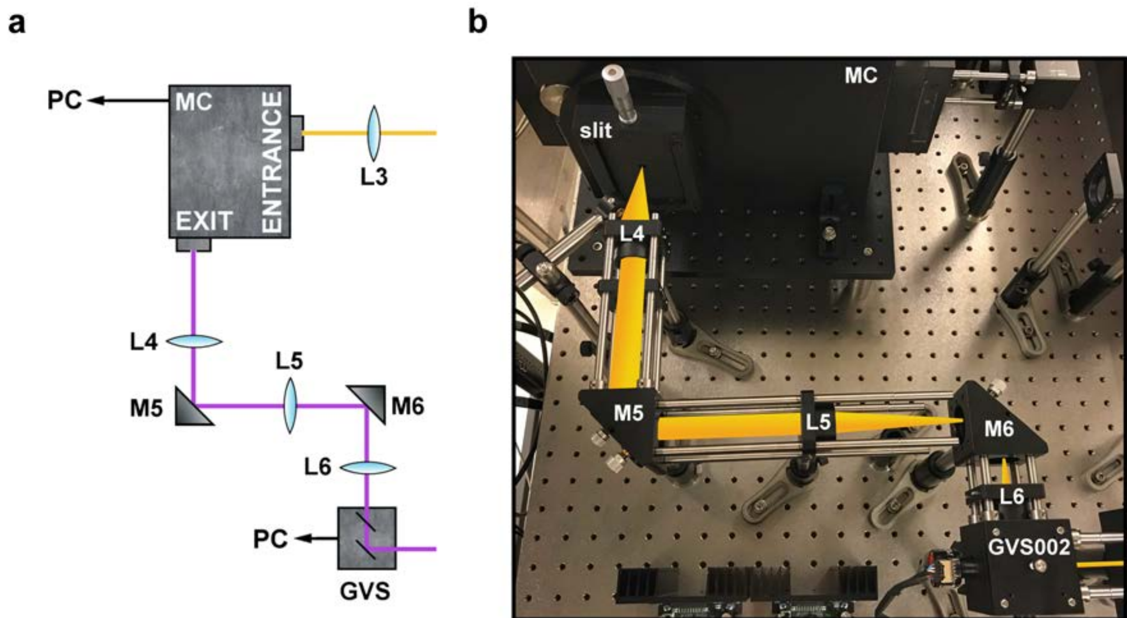

Figure 4.14. Getting light out of the MC. a, Schematic of the optical components that collimate the output light from MC. b, Optical diagram of light on a photograph of the actual microscope.

A pair of lenses (L2, and L3) with focal lengths of 150 mm, and 30 mm is used to reduce the beam size by 5 times.

Figure 4.14 a, and b show the schematics and a photograph of the optical and optomechanical components before it reaches the galvos system. The spectrally resolved light cone exiting the slit in Fig. 4.14 gets collimated via f_4=75 mm. A pair of lenses of f_5 = 150 mm and f_6 = 30 mm introduces a collimated beam of laser light to the scanning mirror of galvos system (GVS002) compatible with its optical components. Using four adjusters of the two mirrors M5 and M6 we can tune the laser path along ±x and ±y into a perfect alignment.

4.6.5 Dual-Axis Scanning Galvo System

The output of the lens L6 in figure 4.15a is a collimated single wavelength beam that hits the scanning mirror (bottom mirror) of the dual-axis galvos system (Thorlabs, GVS002). The dual-axis galvos scanner system comprises a galvanometer, two mirrors, two servo driver boards, and a power supply (Thorlabs, GPS011). A schematic of the electrical circuit configuration of the components and mirrors assembly is shown in figure 4.15 a, c, & d.

Each galvo consists of a galvanometer-based scanning motor with an optical mirror mounted on the shaft and a detector that provides mirror positional feedback to the control board. The mirror assembly shown in Fig.4.15b is attached to the end of the actuator, and deflects the light beam over the angular range of the motor shaft. Servo

driver boards displayed in Fig. 4.15c interpret the signal from the optical position detecting system inside the motor and then produce the drive voltage required to rotate the mirror to the desired position. The galvo power supply shown in Fig. 4.15 d allows two driver cards to be powered via the separate 2 m power cables.

The two output channels of DAQ#2 (A02, and AO3) illustrated in figure 4.5 provide DC voltages required for the actuator attached to the mirrors through LabView control or the custom-written python based software (SSM). Connections from DAQ output channels (AO2 and AO3) to driver boards are colored in yellow and from power supply to x-scanning and y-scanning driver boards and eventually to the actual actuators in cyan and pink respectively.

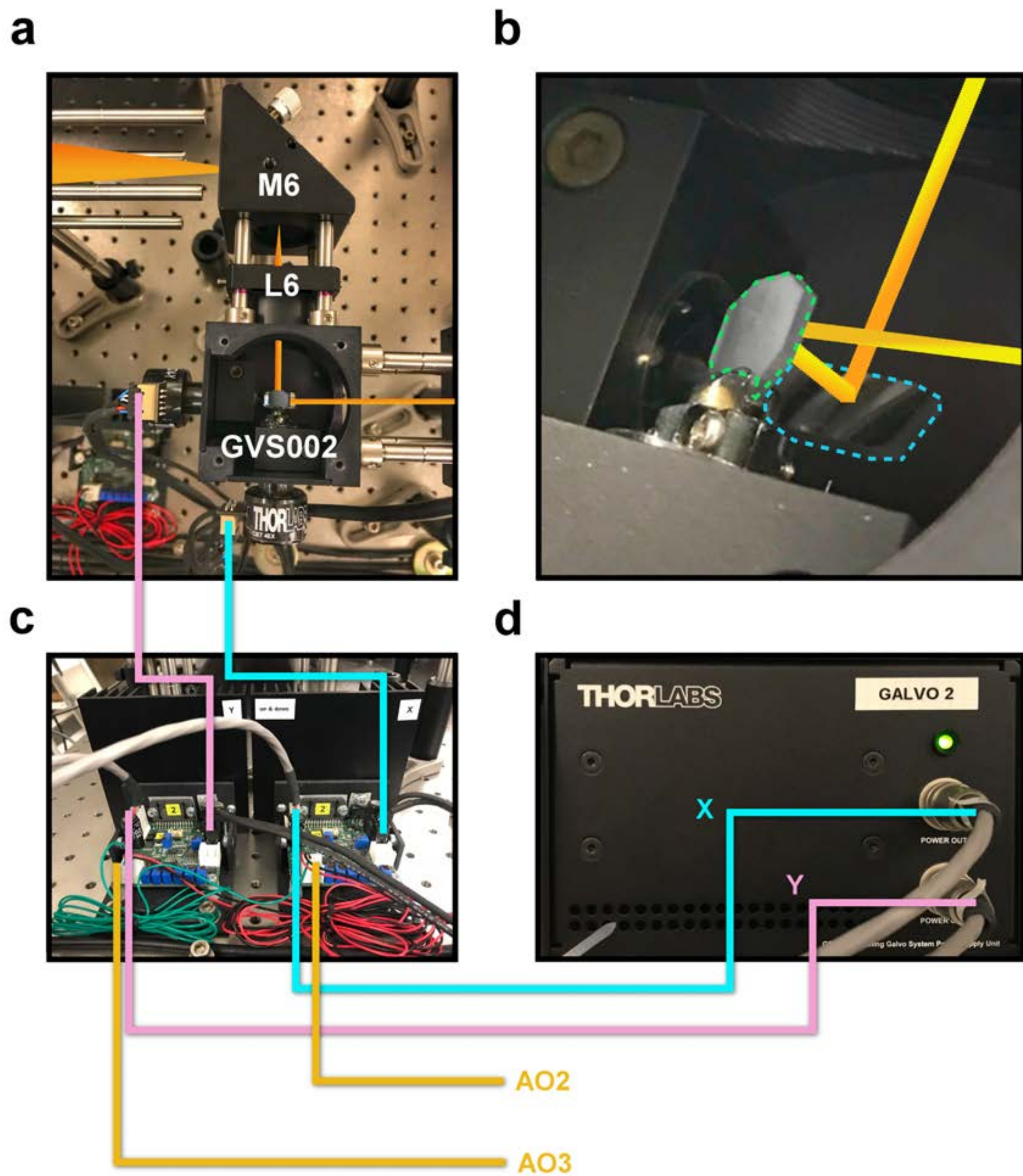

Figure 4.15. Scanning galvo system. a, Optical diagram of light entering and leaving the galvos. b, Mirror assembly configuration. c, Servo driver boards to control scanning over x and y. d, Galvo power supply.

4.6.6 Spatially And Spectrally Resolved Laser Excitations

The beam reflecting from the scanning mirror propagates into a pair of inked achromatic lenses before entering the microscope. In order to maximize the optical power focused onto the device the laser beam should fill the rear aperture of the microscope objective. The diameter of the beam leaving the scanning mirror is about 4 mm (about the size of the aperture) therefore the focal length of these two lenses are chosen equal f_1=f_2=100 mm to avoid beam expansion or reduction. Their only function is to translate the image from the scanning mirror to the rear aperture of the microscope.

Choosing inked achromatic lenses allow the laser beam scanning on the surface of the device without aberration and stray light. Figure 4.16 shows a schematic of the light propagation from scanning mirror (M1) towards the aperture and then scanning over device surface.

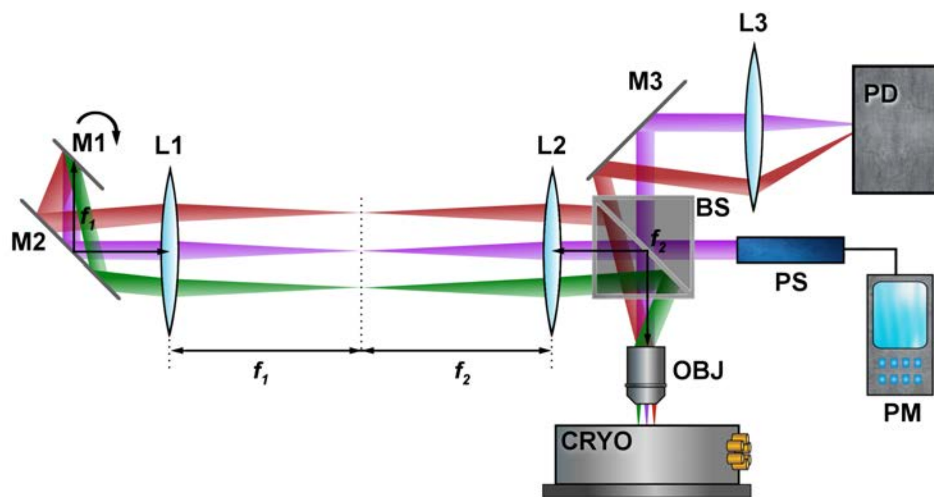

Figure 4.16. Schematics of the scanning Gaussian beam over the surface of the sample.

Scanning mirror M1 reflects the collimated light to mirror M2 from which it's introduced into the lens pair L1 and L2. The lens pair images the beam spot at M1 to the spot at the back of the objective (OBJ) of the microscope via a beam splitter (BS) that reflects 90% of light towards the sample. The light is then focused to a diffraction-limited spot on the surface of the sample in the cryostat using the objective.

Since the two lenses L1 and L2 have equal focal lengths the spot size remains consistent. The beam that passes through the center of the lenses with no deflection is shown in purple in Fig 4.16. When the scanning mirror rotates, the collimated beam is deflected from center; two angles of scanning are illustrated in figure 4.16 by red, and green. With a deflected light the image still forms on the same spot at the rear of the objective but with an angle of incidence. The actuating voltage applied to the galvanometer from the output channels (AO2, and AO3) can controllably change the angle of incidence and scan the focused Gaussian beam across the sample surface and generate a spatial map of photogenerated current.

The reflected light from sample transmits through the BS and reflects to a lens (L3) with focal length of f_3 = 50 mm via a right-angled mirror (M3), and finally gets collected by a photodiode detector (PD). The photodiode converts the optical power to electrical power as a photovoltage; the intensity of the photovoltage is monitored to form a simultaneous reflection image of the sample.

To monitor the whole wavelength range we use two photodetectors. A Si switchable gain detector (Thorlabs: PDA36A) is sensitive to the light from UV to NIR

wavelength range (350-1100 nm), and an InGaAs photodetector (Thorlabs: DET10C) on the other hand is designed to detect light signals ranging from 900 to 1700 nm. The light beams reflecting back from sample surface get focused on the screen of PD to form simultaneous reflection image of the sample, from which differential reflection analysis would be possible. Figure 4.17a,b shows the schematics and actual optomechanical components of the microscope that introduces light from galvos (GVS) to the objective and eventually to the sample for 2D scanning.

As mentioned in section 4.6.1 of this chapter, the Fianium light source provides white light in a broad spectral variance between 400-2200 nm. To achieve the highest performance of this microscope over such a broad spectral range, optical components should match the wavelength range that we choose to conduct experiments. There are three different beam splitter coatings to cover the whole wavelength range. Thorlabs non-polarizing achromatic beam splitter cubes can provide a uniform reflection in these three ranges; BS028 for Vis (400-700 nm), BS029 for NIR (700-1100 nm), and BS030 for IR (100-1600 nm).

The objective used for this microscope is an Olympus UCPLAN N 50X with a high numerical aperture of 0.65 and a long working distance of 2-4 mm. It's designed for optimal transmission in the near infrared (700-130 0nm wavelengths). Using this objective at the wavelengths beyond this range would cause a slight power loss. To have a high efficiency microscope we can mate the BS and OBJ depending upon a change in the wavelength range. These objectives include a corrector ring that adjusts internal

optics to focus through the glass medium; it's designed to compensate for the optical aberrations caused by focusing light through a 1 mm thick transparent glass window of the cryostat.

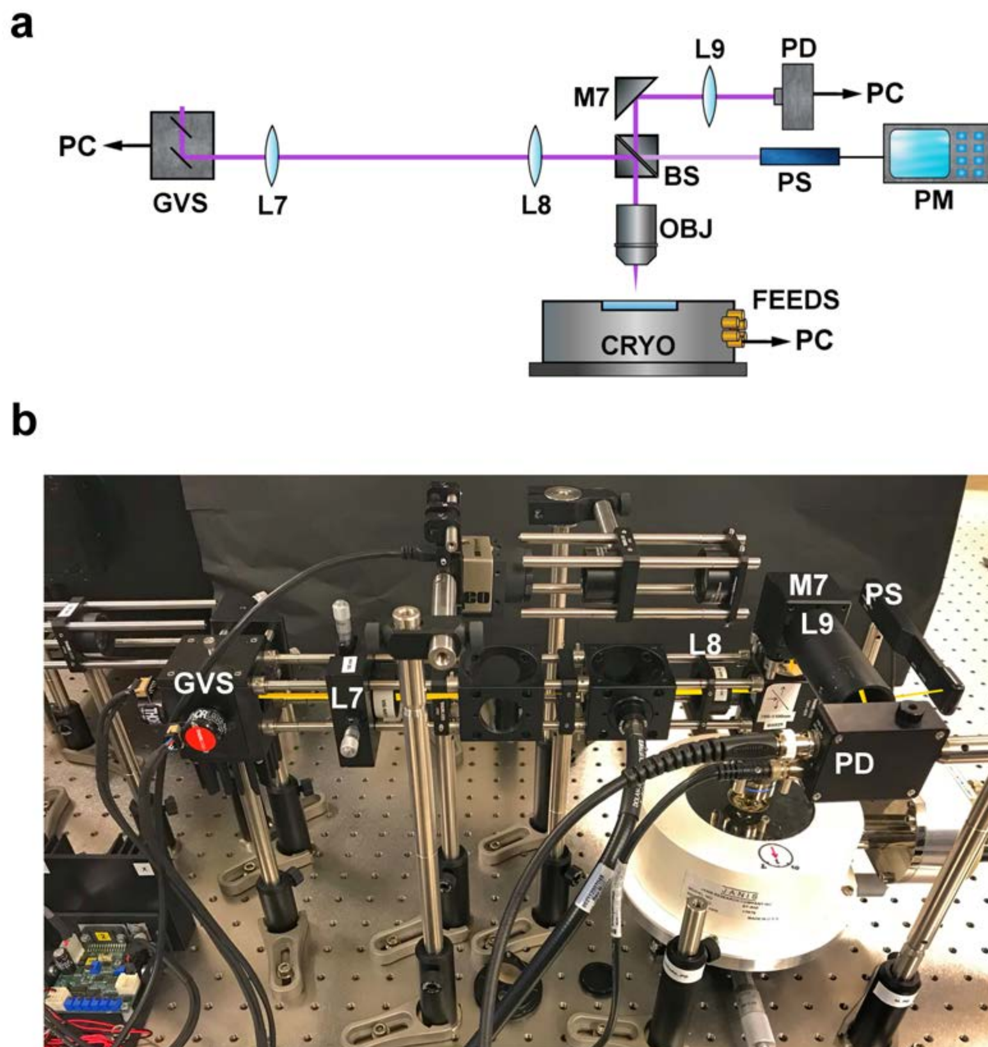

Figure 4.17. Diffraction limited beam spot to the cryostat. a, Schematics of the optics to introduce light to sample. b, Optical diagram on a photograph of the actual microscope.

As mentioned earlier in this section these beam splitters reflect 90% of the light to the sample; the 10% of the light that transmits through the BS can get detected with a power sensor (PS) coupled to a power meter (PM). The power sensor response function should also match the wavelength range of the microscope; using two power sensors (Thorlabs: S130C, and S132C) we can accurately detect the optical power in the ranges of 400-1100 nm and 700-11800 nm respectively in the power range of 500 pW-500 mW.

In this scanning photocurrent microscopy technique the reflected light and the device current are simultaneously collected as the focused laser spot is scanned across the surface of the sample and as a result a pair of correlated spatial maps are generated. These maps are then displayed and analyzed using LabView or python custom-written control software.

Through this microscope we can perform spatial imaging as a function of wavelength by fixing the spectrum at a specific wavelength and conducting 2D spatial scans over the surface of the sample, as changing other parameters such as V_{SD}, V_G, or temperature in order to make 3D or 4D data cubes. We can also perform spectral imaging with a narrow resolution of 1 nm by fixing the laser beam at a specific spot on the device (preferably the heterostructure) while tuning the spectral range over y axis, in this case x axis could be variation of other parameters such as V_{SD}, V_G, or temperature.

4.6.7 Power Dependence Experiments

Another unique function of the supercontinuum scanning photocurrent

spectroscopy microscope (SSPSM) is the ability of allowing power dependence scanning experiments at any specific wavelength within the range of 400-2200 nm. The fiber output power is 8 W, which is high enough for generating a power dependence experiment.

In figure 4.18a placing a mirror on a flip mount (FM1) allows us to deflect laser light from reaching M2. The white light with 8W power then reflects into a periscope and from there reaches a band-pass filter. Using Thorlabs band-pass filters we can allow a specific wavelength with only ± 2 nm to transmit through and reach M9. These filters cut out the laser power to tens of mW, which is pretty good for power dependence experiments. Using the second flip mount (FM2) we lead the light towards reaching the galvo system to again generate a diffraction limited beam spot.

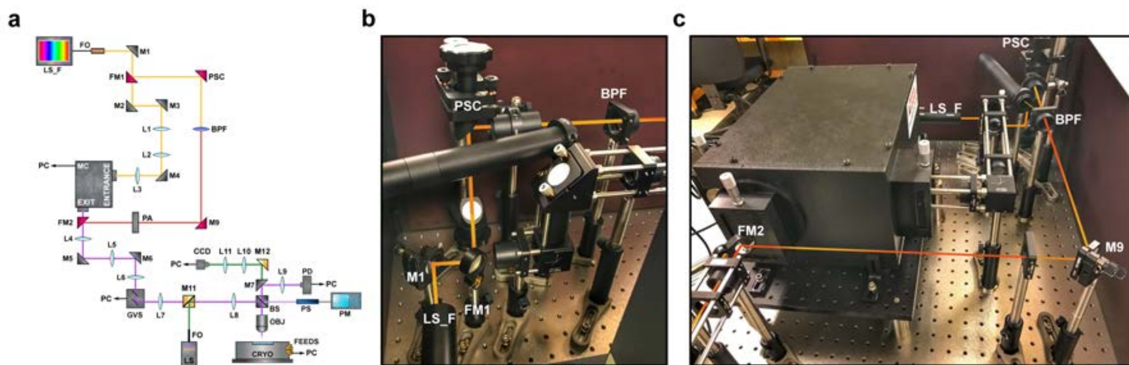

Figure 4.18. Power dependence experiment. a, Schematic of the supercontinuum scanning photocurrent spectroscopy microscope (for a more clear image please see Fig. 4.1). b, Leading optical light from source to a band pass filter (BPF) using a flip mount (FM1). c, Optical light path from BPF to FM2.

Placing a motorized rotation mount (Thorlabs, K10CR1) coupled to a continuously variable reflective neutral density filter (Thorlabs, NDC-50C2) in front of the laser light allows us to control the intensity of the power. These filters provide linear, adjustable attenuation within the coated region via rotation. Using this function of the microscope we can spatially scan surface of devices while stepping through the new parameter, which is optical power. Figure 4.18b, and c illustrate ray diagram on the photographs taken from the actual microscope.

4.7 Running Experiments Through Software

Photocurrent and reflected photovoltage V_{REF} from spatial or spectral scanning can be imaged simultaneously while running the experiments. Using LabView or SSM (a custom-written python based software) helps us to vary different input parameters and get a view of the outcome signal in maps.

Figure 4.19a shows a profile of SSM software, consisting of three main panels at the left to vary and control parameters. Panel_1 allows us to center the reflection imaging or the photoresponse on the maps, set a fixed value for source-drain and gate voltages, vary number of pixels along X and Y axis as well as changing the scan line rate. Through panel_2 we can assign back-gate (AO1), source-drain (AO0), or x-axis (AO2) as the fast scanning axis along x direction, whereas assign back-gate (AO1), source-drain (AO0), Wavelength, or y-axis (AO3) along y direction as the slow scanning axis within a desired range. Panel_3 allows generating data cubes of 2D spatial scans with the third parameter being change in one of parameters of back-gate, source-drain or wavelength, as well as

repeating the data cube in another direction to generate 4D scans by varying one of the other two remaining parameters.

Right column on the software profile shows 2D maps of reflection image and photocurrent image taken from device in panel b of this figure, photoresponse is observed where there is an overlap between the two layers of the heterostructure.

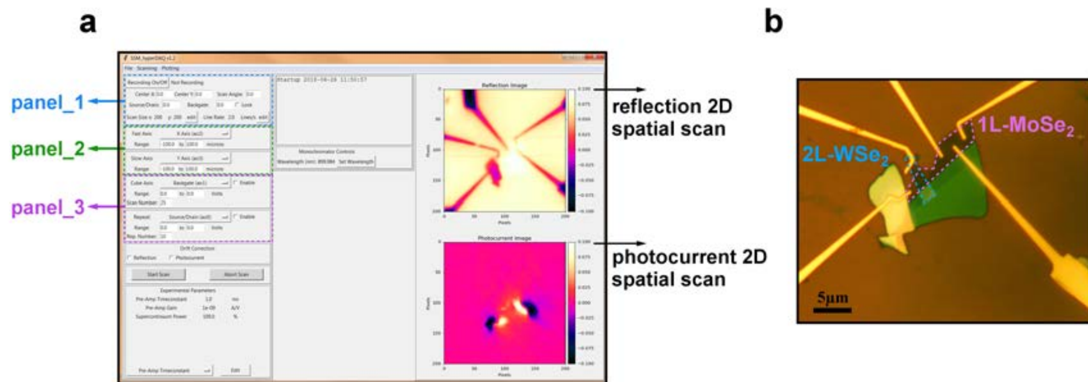

Figure 4.19. Profile of the custom-written SSM software. b, Optical image of a device consisting a *2L*-WSe_2 stacked on top of a *1L*-$MoSe_2$.

REFERENCES

1. *NKT Photonics*, www.NKTPhotonics.com

2. Robert R. Alfano, *The Supercontinuum Laser Source*, *The ultimate white light*. Library of congress, New York, (2016).

3. Eugene Hecht, *Optics, Fifth edition*. Pearson Education, (2017).

CHAPTER 5

BASIC OPTICAL CHARACTERIZATION OF TMD HETEROSTRUCTURES

5.1 Introduction

The investigations of optical properties of layered materials represent one of the main directions of current materials research, as light exposes many of the properties of semiconductors and their structures. There exist many techniques to explore optical properties of materials, among which Raman and photoluminescence are two that are widely used in research and materials development. Raman spectroscopy is a spectroscopic technique used to observe vibrational, rotational, and other low frequency modes in a system. Because the vibrational spectrum is sensitive to the sample thickness, Raman spectroscopy has been widely used to determine the number of layers of exfoliated transition metal dichalcogenides; the energy, width, and amplitude of the vibrational modes are strongly influenced by the thickness of the flakes. These vibrational modes of the crystalline lattices are called phonons. On the other hand, Photoluminescence (PL) is the light emission from any form of matter after the absorption of photons. In this chapter we first present a comprehensive optical characterization of transition metal dichalcogenides - $MoSe_2$, WSe_2 and heterostructures composed of these materials - via two powerful optical spectroscopy techniques: Raman and Photoluminescence. Using extensive characterization including differential reflection, and photocurrent spectroscopy, we confirm strong interlayer electronic coupling at the heterostructure interface. Photocurrent spectroscopy measurements, which

expose a great deal of new information about the heterostrucutres examined here, are presented in chapters 5 and 6 in high detail.

5.2 Raman Spectroscopy

Raman Spectroscopy is a non-destructive analysis technique that provides detailed information about the chemical structure, crystal structure, and molecular interactions. Raman spectroscopy is based on the interaction of light with the chemical bonds within a material, and directly probes the lattice vibrations of a crystal. To model the vibrational modes of a molecule or crystal, we assume that the material is composed of masses (atoms) joined by springs (chemical bonds), so that an input of energy into the system will lead to mechanical vibrations. Each of these vibrational modes is initiated by a specific frequency, usually in the infrared region of the electromagnetic spectrum, and in many systems they are quantized like electronic energy levels. These molecular vibrations cause a change in the polarizability or the dipole moment of the molecules. When a high intensity laser light is introduced to a material, the molecules scatter the incident light. A small fraction of scattered light emerges at different wavelength from the initial light source, and the energy difference depends on the structure of the material. This process, called Raman scattering[1] may occur through the absorption or emission of a phonon within the crystal structure.

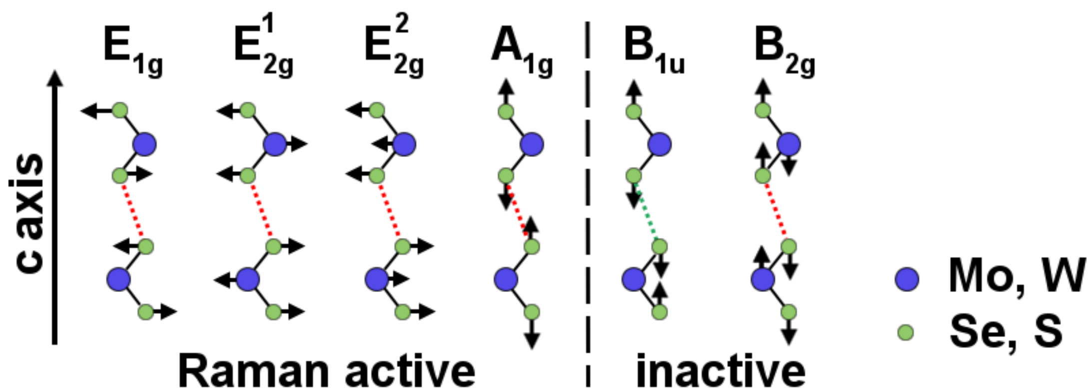

Figure 5.1. Schematic drawing of the four Raman active and two inactive modes of the transition metal dichalcogenides MX_2 (M=Mo, W and X=Se, S). This figure is adapted from reference 1.

We use Raman spectroscopy to determine the number of layers of exfoliated transition metal dichalcogenides as the energy, width and amplitude of the vibrational modes are strongly influenced by the thickness of the flakes and also to identify the vibrational Raman active modes in the atomic layers.

There are four Raman active and two inactive modes of the transition metal dichalcogenides MX_2 (M = Mo, W and X = Se, S) representing different vibrations of the atoms in the lattice, shown in figure 5.1. Raman active mode consists of three in-plane modes (E_{1g}, E^1_{2g}, and E^2_{2g}) and one out of plane mode (A_{1g}).

The devices, shown in Figure 5.2 a & d, were first characterized to identify layer thickness and ensure interlayer coupling, as determined through Raman and photoluminescence (PL) spectroscopy. We used a Horiba LabRAM HR spectrometer with an excitation of 532 nm, with working range of 100 cm^{-1} to 9700 cm^{-1}.

Measurements are performed at room temperature with the power of excitation laser at 2 mw for both individual layers of $MoSe_2$ and WSe_2 and the overlapped region of the heterostructures $WSe_2/MoSe_2$. Figure 5.2 b & e show the Raman spectrum for the $MoSe_2$ and WSe_2 flakes that were carried out before and after constructing the heterostructure.

For the monolayer $MoSe_2$ we observed a very active mode at 241 cm^{-1} (30 meV), and another mode at 289 cm^{-1} (36 meV). The first Raman active vibrational mode is assigned to an out of plane vibration of A' in which Se atoms oscillate in opposite phase perpendicular to the atomic plane with respect to Mo atom at the center not moving, while the second not very active mode to an in-plane vibration of E^1_{2g}, at each unit cell this low intensity mode is caused by Se atoms oscillating in opposite phase with Mo atom in the plane of the atomic layer. Our measurements are in excellent agreement with other studies attributing these vibrations to a monolayer $Mose_2$.

For bilayer WSe_2 we found a very active Raman mode at 250 cm^{-1} (31 meV), and two other modes one at 256 cm^{-1} (31.7 meV) and the other at 308 cm^{-1} (38 meV). Based on many previously reported literatures the combination of these modes is an indication of having a bilayer material. The first two very close modes near 30 meV are assigned to E^1_{2g} and A_{1g} respectively. In E^1_{2g} vibrational mode two in phase Se atoms oscillate in opposite to a W atom at each layer and the two layers oscillate laterally opposite to one another, while in A_{1g} mode Se atoms oscillate in opposite phase, out of plane with respect to W atoms.

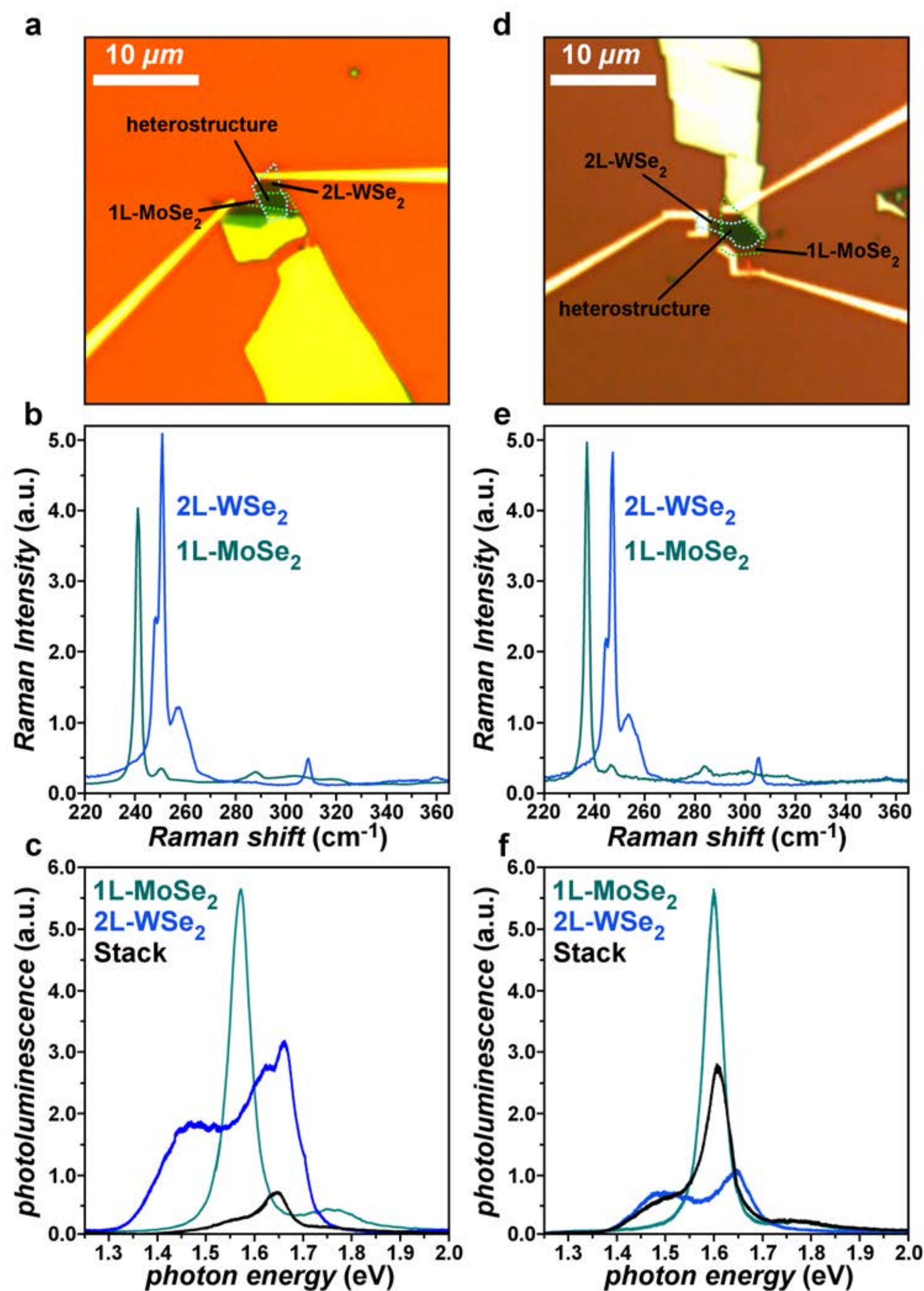

Figure. 5.2. Optical images, Raman spectroscopy, and PL spectroscopy of Devices 1 and 2. a, d, Optical images of the two $MoSe_2$/*2L*-WSe_2 heterostructures with contacts. b, e, Raman spectra (excitation wavelength λ=532 nm) for $MoSe_2$ (green), and *2L*-Wse_2 (blue). c, f, PL spectra of $MoSe_2$ (green), *2L*-WSe_2 (blue), and the stack (black).

5.3 Photoluminescence Spectroscopy

Figure 5.2 c & f show the room temperature photoluminescence (PL) spectra with a laser wavelength λ= 532 nm fixed on the individual TMDs and on the overlapped region. A schematic of the device geometry along with higher resolution PL spectra taken from each layer and the overlapped region is shown in figure 5.3 a and b respectively. In the monolayer $MoSe_2$ (green line, Fig. 5.3 b), PL peaks were observed at photon energy E_{PH} = 1.57 eV and 1.75 eV, while in *2L*-WSe_2 (blue line, Fig. 5.3 b), two peaks were observed at E_{PH} = 1.46 eV and 1.66 eV. When measured in the heterostructure overlap region, we observed strong suppression of the lowest energy PL peak (originating from the WSe_2), and an order of magnitude decrease of the PL peaks at 1.55 eV and 1.64 eV. Such PL suppression, which was typical of these devices, has been studied previously[2-6] and is attributed to charge redistribution and the formation of spatially indirect, bound e-h pairs at the interface.

The PL spectra of the heterostructure devices show several key features that indicate interlayer electron transfer and equilibrium charge redistribution between the layers in the heterostructure[7,8]. Figure 5.2c shows the photoluminescence (PL) spectra of $MoSe_2$, *2L*-WSe_2, and the heterostructure. The PL emission of $MoSe_2$ has a large peak at 1.57 eV and a shoulder at 1.75 eV, while the *2L*-WSe_2 exhibits two peaks at 1.46 eV and 1.66 eV, in agreement with previously reported data2. Figure 5.2 (d, e, and f) shows characterization data for a second *2L*-WSe_2/$MoSe_2$ heterostructure, Device 2. Raman spectra and PL are again in agreement with the results of ref[1].

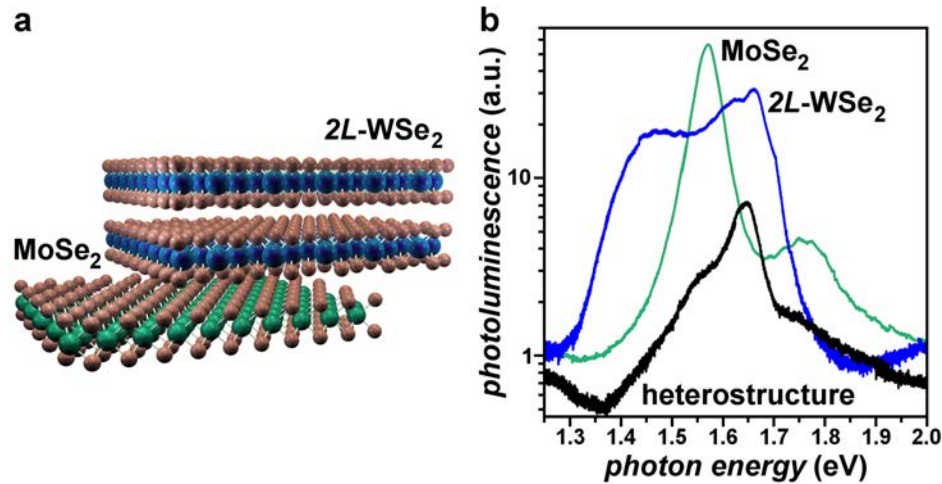

Figure 5.3. Device geometry and the PL spectra of the 2D semiconductor heterostructure device. a, Schematics of the atomic layer heterostructure. b, Photoluminescence (λ = 532 nm) from MoSe2 (green), *2L*-WSe2 (blue), and the heterostructure (black).

5.4 Photocurrent and Differential Reflection Spectroscopy

After devices were placed into high vacuum (10^{-6} torr), we first annealed the samples at 420 °C for 48 hours to improve device contact quality and remove surface contaminants[6]. Following this procedure, the devices were kept under a 10^{-6} torr vacuum at all times. We carried out scanning photocurrent spectroscopy measurements using a tunable Ti:sapph laser with 200 fs pulse duration and a 76 MHz rep rate combined with a custom-built scanning microscope[9]. The photocurrent was measured with a diffraction-limited beam spot at various wavelengths over the Ti:sapph laser range (wavelengths 700-1000 nm) and at average powers below 1 mW. After initial photocurrent measurements to assess device contacts, the device resistance and DC current noise was significantly decreased when measured at low and high V_{SD} voltage. An order of

magnitude decrease in the low-bias (V_{SD} < 0.5 V) resistance was typical after 12-24 hours of sustained scanning photocurrent measurements under vacuum, after which time the device remained stable. Each of the devices described here were measured for more than 60 days, and demonstrated stable operation after annealing.

After annealing, photocurrent and differential reflection spectra were taken to confirm interlayer coupling at the interface, as determined by the strong correlation with PL spectral features. We measured photocurrent and reflection spectra with a 0.7 mW beam focused to a diffraction-limited 500 nm diameter (FWHM) spot. Figure 5.4 a shows photocurrent (red), ΔR/R (blue), and PL (gray) as a function of incident photon energy. The quantity ΔR/R is the difference between the reflection at any point and the reflection of the silicon substrate, normalized by the background reflection from the substrate. In Figure 5.4 b we show spatial ΔR/R maps taken at different wavelengths. We observed a clear spatial dependence of ΔR/R, and a wavelength-dependent transition from positive, through zero, and then to negative ΔR/R. We took the data from the green dot in Figure 5.4 b to plot the ΔR/R spectrum in Figure 5.4 a. The zero crossing of the ΔR/R spectrum occurs near 1.45 eV, and a minimum in ΔR/R occurs at 1.66 eV, slightly higher in energy than the peak in PL emission. The photocurrent shows a peak near 1.66 eV and continues to increase at higher photon energies.

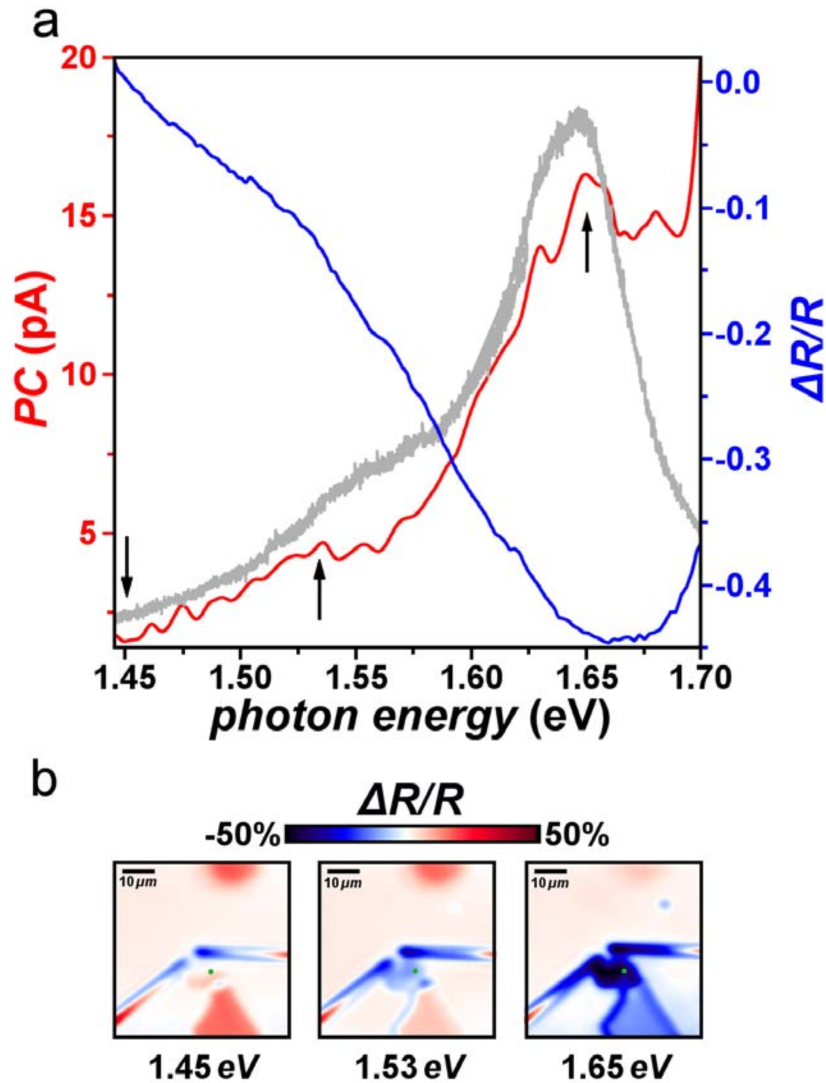

Figure. 5.4. Differential reflection and photocurrent spectroscopy measurements of Device 1 in figure 5.2. a, Photocurrent, ΔR/R, and PL spectra from $MoSe_2/2L$-WSe_2 heterostructure illustrated respectively by red, blue, and gray lines. b, Spatial ΔR/R maps at different excitation photon energies (labeled).

REFERENCES

1. Tonndorf Ph., et al., Photoluminescence emission and Raman response of monolayer MoS_2, $MoSe_2$, and WSe_2. *OPTICS EXPRESS 4909,* **21** (2013).

2. Hong, X. et al. Ultrafast charge transfer in atomically thin MoS2/WS2 heterostructures. *Nat. Nanotechnol.* **9**, 682-686 (2014).

3. Rivera, P. et al. Valley-polarized exciton dynamics in a 2D semiconductor heterostructure. *Nat. Commun.* **6**, 1-6 (2015).

4. Rivera, P. et al. Observation of long-lived interlayer excitons in monolayer MoSe2– WSe_2 heterostructures. *Science* **351**, 688-691 (2016).

5. Rigosi, A. F., Hill, H. M., Li, Y., Chernikov, A. & Heinz, T. F. Probing Interlayer Interactions in Transition Metal Dichalcogenide Heterostructures by Optical Spectroscopy: MoS2/WS2 and MoSe2/WSe_2. *Nano Lett.* **15**, 5033-5038 (2015).

6. Furchi, M. M., Pospischil, A. A., Libisch, F., Burgdörfer, J. & Mueller, T. Photovoltaic Effect in an Electrically Tunable van der Waals Heterojunction. *Nano Lett.* **14**, 4785- 4791 (2014).

7. Rivera, P. et al. Valley-polarized exciton dynamics in a 2D semiconductor heterostructure. *Nat. Commun.* **6**, 1-6 (2015).

8. Ceballos, F., Bellus, M. Z., Chiu, H. & Zhao, H. Ultrafast charge separation and indirect exciton formation in a MoS2–MoSe2 van der waals heterostructure. *ACS Nano* **8**, 12717- 12724 (2014).

9. Kresse, G. & Furthmüller, J. Efficient iterative schemes for ab initio total-energy calculations using a plane-wave basis set. *Phys. Rev. B* **54**, 11169-11186 (1996).

CHAPTER 6

HOT CARRIER-ENHANCED INTERLAYER ELECTRON-HOLE PAIR MULTIPLICATION In VDW HETEROSTRUCTURE PHOTOCELLS

6.1 Introduction

Two-dimensional TMDs have captured a great deal of attention in the scientific communities for their wide range of unique properties, as well as their promise for electronic and optoelectronic performance at the nanoscale. In this chapter, we describe the electronic operation and electronic transport measurements of heterostructures composed of WSe_2 and $MoSe_2$. We measure the electronic transport characteristics at various regimes of applied bias and gate voltage as a function of temperature. Through interlayer I-V_{SD} characteristics we report on highly efficient multiplication of interlayer e-h pairs in these 2D semiconductor heterostructure photocells, indicating that layer-indirect e-h pairs are generated by hot electron impact excitation at temperatures near T = 300 K. By exploiting this highly efficient interlayer e-h pair multiplication process, we demonstrate near-infrared optoelectronic devices that exhibit 350% enhancement of the optoelectronic responsivity at microwatt power levels. Our findings, which demonstrate the remarkable efficiency of carrier multiplication in TMD- based optoelectronic devices, make 2D semiconductor heterostructures viable for a new class of ultra-efficient photodetectors based on layer-indirect electron-hole excitations. The main results of this chapter were published in reference 1.

6.2 2D-TMD Semiconductors Junction Characteristics

Heterostructures based on atomically thin van der Waals materials are fundamentally different and more flexible than those made from conventional covalently bonded materials, in that the lack of dangling bonds on the surfaces of van der Waals materials enables the creation of high-quality heterointerfaces without the constraint of atomically precise commensurability[2]. Two-dimensional (2D) transition metal dichalcogenides (TMDs) have recently emerged as promising candidates for future electronics and optoelectronics.

While most of TMDs are intrinsic n-type semiconductors due to electron doping originating from chalcogen vacancies, stacking two different TMDs can generate not only N-N but also P-N, and P-P junctions at the interface. Depending on the detailed work function of the constituent materials, a hetero-interface will have one of the three types of band alignment formed at the junction. From the conventional perspective, charge transfer across the heterojunction is driven by the electronic band structure alignment of the acceptor and donor materials[3]. The hetero-interface could then be one of the following types: straddling (type I), staggered (type II), and broken (or misaligned, type III), as illustrated in figure 6.1. The hole and electron are separated into different components for type II and type III heterostructures and are the desired band alignment for charge separation. In these cases, devices can be formed into electronic hetero-junctions with different concentrations of N- (electron) and P- (hole) type charge carriers. Thus, they can form P-N, N-N, and P-P junctions depending on the position of the Fermi

level at equilibrium.

The combination of two TMD materials $MoSe_2$ and WSe_2 forms a type II band alignment at equilibrium, creating an ideal system for charge transfer. In this section we study the electronic band structure of a heterostructure composed of tungsten diselenide (WSe_2) and molybdenum diselenide ($MoSe_2$) at the interface under applied positive and negative gate and source-drain voltages. In the next two sections, we then study the two regimes of N^+-N and P-N in detail.

Figure 6.2 shows the electronic band structure of the $MoSe_2$/*2L*-WSe_2 heterostructure investigated here. In the intrinsic (uncharged) state (Fig. 6.2, a), the chemical potential of the entire system is leveled under equilibrium condition at the charge neutrality point and there is an equal space between the chemical potential and each of the two lowest conduction band and highest valence band in the system.

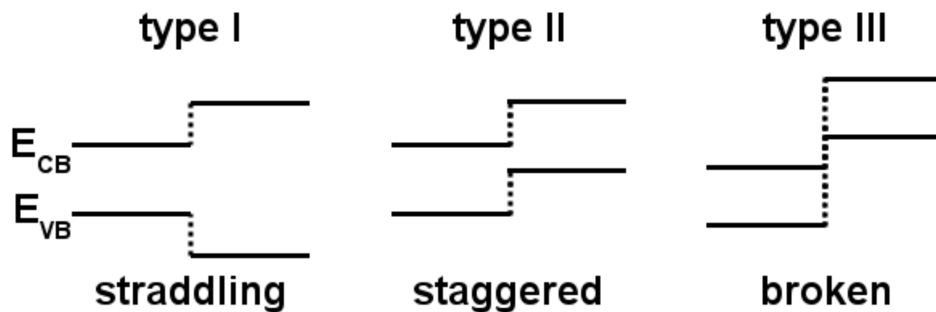

Figure 6.1. Various heterostructure band alignments. For type I heterostructures, the band energy levels of one material straddle those of the other, resulting in the transfer of both holes and electrons to the narrower band gap material. For type II and III heterostructures, the band energy levels are staggered or broken, respectively, so that charge separation is energetically favorable.

There are three layers in the system; the first layer is the Si substrate being used as the back-gate conductance (red is an indication of electrons population and blue is used for holes). Above that a monolayer $MoSe_2$ is placed, the schematic is presenting the conduction and valence band edges, and above all there is a bilayer WSe_2 with its own band edges. There are two gaps (shown in white) between each layer that are presenting the potential wells in the system. At the intrinsic state there is no potential drop in the system and therefore no charge transfer. The conduction band edge of $MoSe_2$ is closer to the Fermi level, making it more n type than $WSe_{2,}$ which has a larger gap between its conduction band and the Fermi level. Tuning the Fermi level up and down via applying gate voltage, it can create N^+-N, P-N, and also P^+-P junctions. Characteristic of the N^+-N and P-N junctions are explicitly represented in sections 1.5.1 and 1.5.2 respectively.

Applying a positive back gate voltage to this type II heterostructure, we increase the hole population at the gate channel, hence electron population will increase at the two-layer stack, as a result it shifts the whole Fermi level of the system up towards the two conduction band edges shown in figure 6.2b. The potential barrier that an electron needs to overcome the first barrier and reach the first layer of the heterostructure (MoSe2) is indicated in the figure 6.2b as eV_G. The effect of the back gate would be different on each of the two layers of the heterostructure as the charge density on layer 1 ($MoSe_2$) screens the capacitive coupling to layer 2 (WSe_2), overall the potential drop between the two layers of the heterostructure would be the subtraction of the gate effect on each of these two layers as $\Delta\phi = \phi_{GMo} - \phi_{GW}$. We can then study the band structure of the system under applying positive and negative source-drain voltages between the two

layers, illustrated respectively in Figure 6.2c & d. Figure 6.2c, illustrates the band structure under applying positive gate voltage plus a positive source-drain voltage to WSe_2 layer. A positive V_{SD} on WSe_2 layer generates a potential difference between the two layers of the heterostructure in the same direction as the gate voltage has created between them, as a result it increases the barrier height and we can call it reverse bias, $\phi_{rev} = \Delta\phi + qV_{SD}$ ($V_{SD} > 0$). Reversing the direction of the source-drain voltage on WSe_2 changes the barrier height differently illustrated in Fig. 6.2d. In this case the potential drop between the two layers caused by source-drain voltage is in opposite direction with the potential drop caused by gate voltage, hence it decreases the barrier height $\phi_{fwd} = \Delta\phi$ - qV_{SD} ($V_{SD} > 0$) and we can call this forward bias.

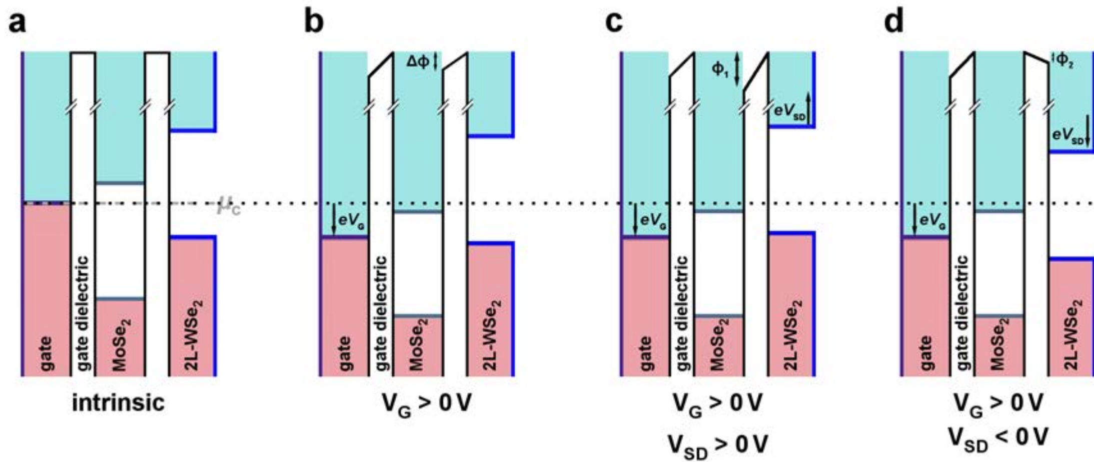

Figure 6.2. Schematics of the $MoSe_2$/*2L*-WSe_2 electronic band structure under different values of V_{SD} and V_G. a, Schematic illustration of the electronic band structure of the heterostructure at the intrinsic state with $V_G = 0V$ and $V_{SD} = 0V$, chemical potential (gray dashed line) of the whole system is leveled under equilibrium condition. b, & c, Electronic band structure under $V_G > 0V$ and $V_G < 0V$ respectively. d, and e, Electronic band structure under $V_G < 0V$ & $V_{SD} > 0V$, and $V_G < 0V$ & $V_{SD} < 0V$ respectively, V_{SD} is applied to $MoSe_2$.

6.3 Gate Voltage Dependence of I-V_{SD} Characteristics of 2L-WSe_2/$MoSe_2$

As discussed before in details in chapter 6.2 and illustrated in figure 6.2 we could electrostatically dope the interface of this heterostructure through a global back gate voltage. As a result we observed an N^+-N device behavior at low V_{SD} and a well-defined transition from insulating behavior at V_G = -50 V to conducting behavior at V_G = 10 V through I-V_G characteristics.

As the source-drain voltage V_{SD} was increased, we observed a highly unusual device response. Figure 6.6a shows a color map of the current I as a function of V_{SD} and V_G. The I-V_{SD} characteristics (Fig. 6.3b inset) measured in the low-current state ($V_G < V_{ON}$) exhibit very distinct behavior from those in the highly conducting N-type transport regime. As the gate voltage increased, the forward bias I-V_{SD} characteristics ($V_{SD} > 0$ V, Fig. 6.3b) exhibited a monotonic increase as a function of V_{SD}. In contrast, Figure 6.3a shows that the reverse bias ($V_{SD} < 0$ V) current first increased sharply to a peak value near V_{SD} = - 4.8 V (bright feature, Fig. 6.3a) and then decreased at higher V_{SD}. The non-monotonic behavior in reverse bias emerged for $V_G > -36$ V.

As gate voltage increased, the current peak remained at an approximately constant V_{SD} value. In the following, we examine the dependence of the interlayer current on source-drain voltage, gate voltage, temperature, and optical illumination. In Figure 6.3c, the reverse bias current peak emerges over a range of gate voltages corresponding to an abrupt increase of the interlayer current I.

To examine the emergence of this peak more thoroughly, Figure 6.3d shows differential conductance dI/dV_{SD} vs. V_{SD} as a function of gate voltage V_G. Near V_{SD} = -2.5 V, a maximum in the differential conductance, labeled g_M, appears as V_G increases.

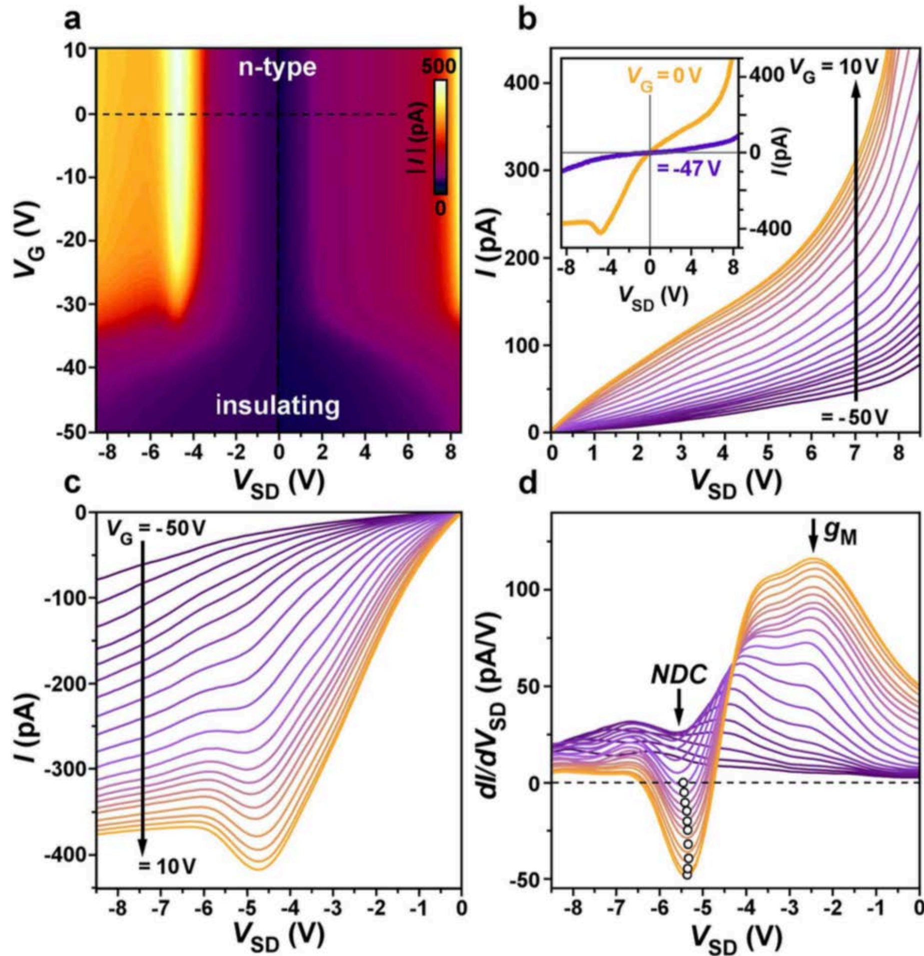

Figure 6.3. Gate voltage dependence of the I-V_{SD} and dI/dV_{SD} characteristics in the 2D n^+-n heterojunction device. a, Color map of I vs. V_{SD} and V_G (T = 340 K; heterostructure overlap area 4.3 μ m2). b, Forward bias I-V_{SD} characteristics as a function of V_G (increasing from dark purple to orange, labeled with vertical solid arrow). Inset, I-V_{SD} characteristics at V_G = 0 and V_G = - 47 V (labeled). c, Reverse bias I-V_{SD} characteristics as a function of V_G. d, dI/dV_{SD} vs. V_{SD} characteristics (T = 340 K). NDC labels the negative differential conductance peak values (marked with open circles). g_M is the maximum differential conductance.

In contrast, near V_{SD} = -5.4 V, valleys in dI/dV_{SD} vs. V_{SD} evolve into prominent negative differential conductance (NDC) for increasing V_G (labeled with open circles). The NDC occurs at a nearly constant V_{SD} value as the gate voltage is increased. We conclude that the onset of NDC, and thus the reverse bias current peak, directly correlates with the V_G dependent onset to unipolar electron conduction.

6.4 Temperature Dependence of I-VSD Characteristics of 2L-WSe2/MoSe2

The striking non-monotonic behavior of the reverse bias I-V_{SD} characteristics also arises as the temperature increases, and differs strongly from interlayer Zener tunneling behavior[4]. We show in Figure 6.4 the I-V_{SD} characteristics as a function of V_G at several temperatures. Below T = 340 K, the I-V_{SD} characteristics exhibit no current peak in reverse bias. At and above T = 340 K, however, the reverse bias current peak becomes evident as V_G is increased (Fig. 6.4a). Importantly, we also observed that the reverse bias current increased much more rapidly with increasing temperature when compared to the current at $V_{SD} > 0$ V. At T = 360 K (Fig. 6.4b), the asymmetry in the I-V_{SD} characteristics is significant: the reverse bias current particularly at low negative V_{SD} is approximately two orders of magnitude larger than in forward bias. By rescaling the temperature-dependent reverse bias interlayer current as $T\,ln(I / T^2)$, the data (for $V_G > V_{ON}$) collapse to a temperature-independent characteristic as a function of V_{SD} (Fig. 6.4c). In forward bias (Fig. 6.4d), a similar temperature-independent characteristic is observed, yet the current must be rescaled as $T\,ln(I / T)$. In contrast to the temperature-independent current expected for interlayer tunneling across the interface[3], the reverse bias interlayer current I

$\propto T^2 \exp(-1/T)$ increases sharply with temperature at low reverse bias, giving rise to a current peak at increased temperatures.

We attribute the non-monotonic reverse bias current to interlayer e-h generation by high-energy electrons transiting the atomic layer interface. In the e-h pair excitation process requiring the lowest excess energy, an electron in WSe_2 gains the combined energy of the interlayer potential energy offset ΔE_c^0 and the kinetic energy of the source-drain electric field to create a low-energy electron in $MoSe_2$ plus an interlayer e-h pair (Fig. 6.4e)

$$e_{\mathrm{W}} + K_e(V_{SD}) \rightarrow e_{\mathrm{Mo}} + (e_{\mathrm{Mo}} + h_{\mathrm{W}}). \quad (6.1)$$

The subscript W or Mo indicates the layer into which the electron (e) or hole (h) is transferred. The final three-body state includes an interlayer e-h pair produced at the interface. The kinetic energy available to an electron e_{W} in WSe_2 is given by $K_e = \Delta E_c$, where $\Delta E_c\ (V_{SD}) = \Delta Ec^0 - \mathrm{e}\ (\alpha V_{SD})$ is the total potential energy drop for the interlayer electron transfer process $e_{\mathrm{W}} \rightarrow e_{\mathrm{Mo}}$. The potential energy drop can be tuned by changing V_{SD}, and the phenomenological factor α accounts for additional voltage drop at the contacts.

To model the device characteristics to include interlayer e-h multiplication, we apply a conventional lucky electron model for hot electron injection through the 2D semiconductor heterojunction (See 6.5 for a detailed representation). Ignoring recombination of interlayer e-h pairs, the low bias current due to e-h pair multiplication I_M takes the form:

$$I_M \propto \Gamma_M \, (k_B\, T)^2 \exp(-K^*_{\mathrm{e}} / k_B\, T), \qquad (6.2)$$

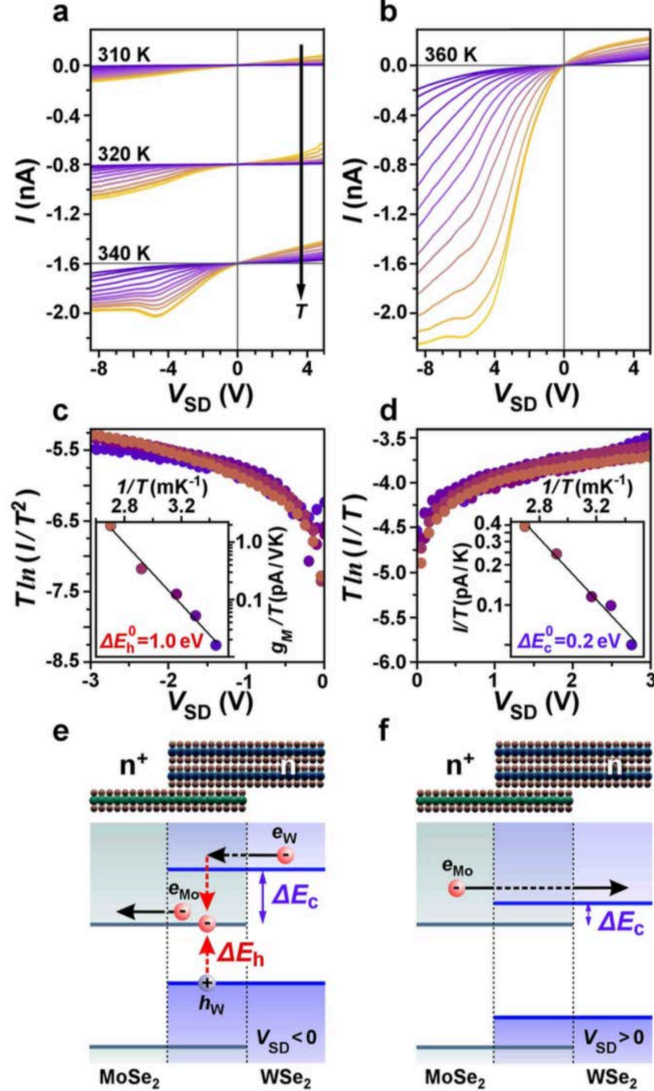

Figure 6.4. Temperature dependence of the interlayer I-V_{SD} characteristics. a, I-V_{SD} characteristics at T = 310 K, 320 K, and 340 K (shifted vertically for clarity). V_G increases from - 50 V to 10 V (dark purple to orange). b, I-V_{SD} characteristics for increasing V_G at T=360 K. c, $Tln(I/T^2)$ vs. V_{SD} in reverse bias at T=300 K, 310 K, 320 K, 340 K, 360 K (V_G =15 V). Inset g_M/T vs. $1/T$ (V_{SD} = -2.5 V, V_G = 15 V). d, Tln(I/T) vs. V_{SD} in forward bias at the same temperatures (V_G = 15 V). d, (inset) I/T versus 1/T at V_{SD} = 2.0 V, V_G = 15 V. e, Electronic potential energy diagram for the heterojunction in reverse bias with electron-hole pairs generated at the $MoSe_2$/$2L$-WSe_2 interface. f, Electronic potential energy diagram for $V_{SD} > 0$ V.

Where k_B is the Boltzmann constant, and Γ_M contains details about the impact excitation probability and interlayer transit rate. The minimum kinetic energy required for a hot electron to excite an interlayer e-h pair in reverse bias is given by

$$K^*_e = \Delta E^0_h - \Delta E^0_c + 2e\,(\alpha V_{SD}), \qquad (6.3)$$

where $\Delta E^0_h > \Delta E^0_c$. When a negative V_{SD} is applied, the potential energy gained by the e_W electron increases while the interlayer excitation energy decreases $\Delta E_h = \Delta E_h^0 - e\,(\alpha V_{SD})$ (Fig. 6.4e). For increasing reverse bias, the rapidly increasing current due to e-h multiplication I_M is overcome by the evolution of the recombination rate with V_{SD}: recombination increases with the reduction of ΔE_h, and also increases with V_G since there are more electrons available to combine with the holes generated through impact excitation. This competition results in NDC and a corresponding peak in the dark I-V_{SD} characteristics.

6.5 Interlayer Electron Transport of 2L-WSe2/MoSe2

In this section, we obtain the temperature and V_{SD} dependence of the interlayer current I by a straightforward calculation based on the electron transmission formalism[5]. Following Chul-Ho Lee, et al.[6], we model a 2D n-type, type II heterojunction in which most of the voltage drop in the device occurs across the vertical junction, leaving no appreciable potential barriers in the lateral transport direction within each semiconductor layer. In our model, we assume these contributions to the functional form of the I-V_{SD} characteristics to be negligible, and later compare this assumption to experimental data. We then evaluate the current in forward and reverse bias by assessing the rates of

electron transmission through the N- type heterojunction (Fig. 6.5), including the rate of interlayer e-h pair multiplication. Our model assesses only carrier kinetic energy, and asks: at what kinetic energy does a carrier have sufficient excess energy to produce additional electron-hole pairs?

Our phenomenological model was developed to qualitatively explain the temperature dependence of the I-V_{SD} characteristics in the voltage regime just below the appearance of NDC. Like conventional heterojunction devices, the current-voltage characteristics are quite complicated, exhibiting several regimes that are described by various microscopic processes. In conventional N^+-N and P-N junctions for example, different regimes often exhibit different ideality factors n. The commonly used ideality factor is attributed to various mechanisms, but strictly speaking is a phenomenological constant included to express the proportionality between electric potential drop and applied voltage. In comparison to our data (section 6.5), we thus include a phenomenological parameter $\alpha < 1$, which quantifies the 'lever arm' between electric potential energy and applied voltage V_{SD}. In section 2.5 we calculated the density of states for atomic layer transition metal dichalcogenides and from equation 2.13 found that the density of states approaches a constant value for electrons near the bottom of the bands, but depends linearly on the electron energy at high energies, which is completely distinct from that at 2D electron gases.

6.5.1 Forward Bias Characteristics

Figure 6.8 shows a schematic of the potential energy landscape for electrons in

the heterojunction for $V_{SD} > 0$ V. For $k_BT >> \varepsilon F$, we assume classical Boltzmann distributions to evaluate how many right-moving electrons (i.e., electrons that are transferred from $MoSe_2$ into WSe_2) transit the interface when a positive V_{SD} is applied. From the left side, we consider a charge carrier with energy that is just enough to get over the potential barrier at the interface ΔE^0_c. From the diagram, this carrier has kinetic energy $\varepsilon - \varepsilon_F = \Delta E^0_c - eV_{SD}$ for $V_{SD} > 0$ V.

In the forward bias interlayer transport process, conduction occurs through electron states near the bottom of the conduction bands in both materials. In this case, the density of states in both layers is approximately independent of energy. The interlayer current results from counting only right-transiting electrons and is given by:

$$I_+ = \int_{\varepsilon}^{\infty} ev\eta_0 g_W(E)\, g_{Mo}(E)\, f(E)\, dE \qquad (6.4)$$

where $v = v_F$ is the electron Fermi velocity, η_0 is the transmission coefficient, $g_W(E)$ and $g_{Mo}(E)$ are the density of states in WSe_2 and $MoSe_2$, respectively, and $f(E)$ is the electron distribution in $MoSe_2$.

Assuming eV_{SD}, $\Delta E^0_c >> k_BT$, the interlayer current is then

$$I_+ = \Gamma_+ \,(k_B T)\, exp\,(-(\Delta E^0_c - eV_{SD})/k_B T \qquad (6.5a)$$

where

$$\Gamma_+ = \frac{ev\eta_0}{(\pi a^2 t^2)^2}\,(\Delta E^0_c + \Delta E^0_h)\,(\Delta E^0_h + \Delta E^0_v). \qquad (6.5b)$$

Here, we model the system to have constant transmission coefficient η_0 for carriers whose total kinetic energy is sufficient to transit the barrier between the TMD layers.

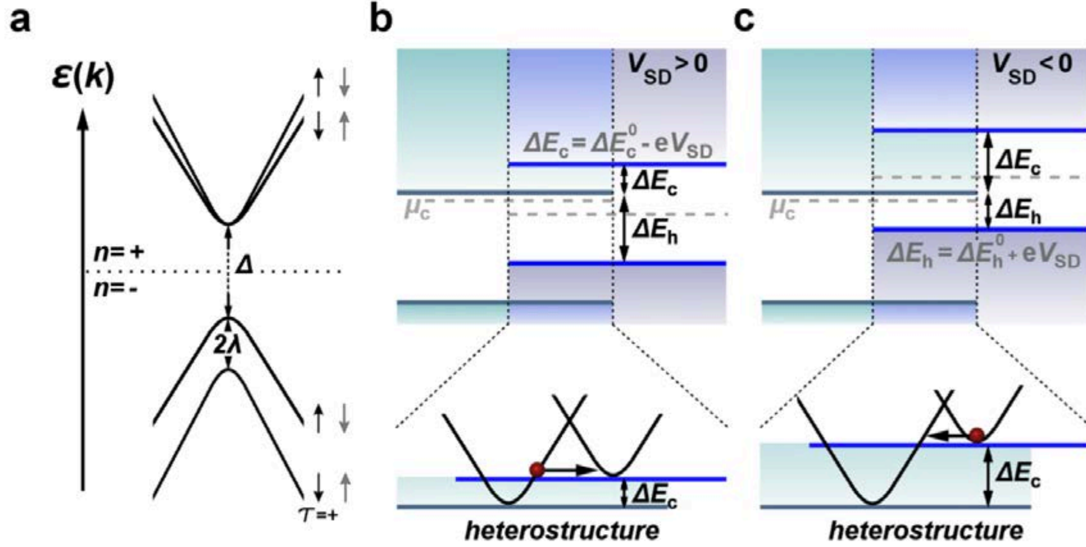

Figure 6.5. Schematics of TMD band structure and interlayer electronic transport. a, energy band diagram of a 2D-TMD material with hyperbolic band structure, b, c, Electronic band structure of the $MoSe_2$/*2L*-WSe_2 under forward and reverse bias respectively, the area inside the vertical dashed line illustrates the heterojunction.

According to Figure 6.5, the band gap energy in WSe_2 is approximately equal to $\Delta E^0_c+\Delta E^0_h$ and in $MoSe_2$ equal to $(\Delta E^0_h + \Delta E^0_v)$.

Equation (6.5) indicates that in forward bias the normalized current I_+/T should exhibit an exponential decrease with $1/T$, from which the activation energy ΔE^0_c can be extracted. Equation (6.5) can also be re-expressed in terms of a temperature-independent quantity that depends only on ΔE^0_c and V_{SD}:

$$k_B T \ln I_+/\Gamma_+ k_B T = -\Delta E^0_c + eV_{SD}. \quad (6.6)$$

The forward bias I-V_{SD} characteristics, when rescaled as $T\ ln(I_+/T)$ as in equation (6.6), should collapse to a single characteristic. The current $T\ ln(I+/T)$ vs. V_{SD} exhibits temperature independent behavior with a linear increase as V_{SD} increases.

The data for all temperatures (Fig. 6.7d) indeed exhibit this behavior, collapsing to a temperature-independent characteristic current $T\ ln(I\ /\ T\ )$. We infer the conduction band offset ΔE^0_c = 0.2 eV from an exponential fit of the forward bias current I/T as a function of $1/T$ (Fig. 3.8d inset). The value obtained from transport measurements shows excellent agreement with band structure calculations ΔE^0 (theory) = 0.20 eV (Fig. 2.4). The energy ΔE^0_c is the maximum kinetic energy available to a hot electron at $V_{SD} = 0$ V (Fig. 1.7a).

6.5.2 Reverse Bias Characteristics

In reverse bias, the temperature and V_{SD} dependence of the interlayer current serves as a signature of hot electron injection into $MoSe_2$, while the thermally activated behavior arises from the energetic threshold for e-h pair multiplication. The electron-hole pair production process takes place in two steps: (1) a low-energy electron in WSe_2 is transferred into a high-energy state in $MoSe_2$. (2) The high-energy (hot) electron in $MoSe_2$ decays and produces an interlayer e-h pair. As the reverse bias voltage is increased, electron-hole pairs generated by high-energy electrons are separated in the electric field and increase the device current. We first define the energy barrier for additional electron generation due to e-h pair multiplication, and then evaluate the interlayer current I that results from e-h pair multiplication when $V_{SD} < 0$ V.

For interlayer transport from WSe_2 (right) to $MoSe_2$ (left), it is important to note that electrons need not overcome a potential energy barrier, but instead may gain the potential energy ΔE^0_c. In conventional devices, this leads to reverse bias saturation current with weak dependence on V_{SD} or temperature[7]. However, interlayer e-h pair production requires a hot electron with a minimum excess kinetic energy, and thus depends strongly on both V_{SD} and temperature. From the schematic in Figure 3.9, the minimum kinetic energy required for an electron to generate an interlayer *e-h* pair is given by:

$$K^*_e = \Delta E^0_h - \Delta E^0_c + 2eV_{SD}, \tag{6.7}$$

where ΔE^0_h is the interlayer e-h pair excitation energy at $V_{SD} = 0$ V. We note that when $V_{SD} < 0$ V, the potential energy that can be gained by an electron is increased $\Delta E_c = \Delta E^0_c + e\,|V_{SD}|$, while the interlayer excitation energy is simultaneously decreased $\Delta E_h = \Delta E^0_h - e\,|V_{SD}|$, resulting in equation (6.7).

In reverse bias, the energy difference between the conduction bands of the two materials is large. Due to the electric field at the interface, low-energy electrons in WSe_2 with approximately constant density of states are transferred into hot electrons in $MoSe_2$ at high kinetic energy with density of states proportional to E (equation (2.13)). The current due to interlayer e-h pair multiplication I_M is then

$$I_M \approx \int_\varepsilon^\infty ev\gamma_0 \left(\frac{E^W_{GAP}}{\pi a^2 t^2}\right)\left(\frac{E}{\pi a^2 t^2}\right) exp\left(-\frac{(E-E_f)}{K_B T}\right) dE; \tag{6.8a}$$

$$= \frac{ev\gamma_0\left(\Delta E^0_c + \Delta E^0_h\right)}{(\pi a^2 t^2)^2} \int_\varepsilon^\infty E exp\left(-\frac{(E-E_f)}{K_B T}\right) dE; \tag{6.8b}$$

where we assume that the product of the transmission coefficient and impact excitation rate γ_0 is approximately constant above the kinetic energy threshold. Computing the integral over the entire energy range and noting $k_B T >> \varepsilon_F$, gives

$$I_M = \Gamma_M (K_B T)^2 \left(exp\left(\frac{-K_e^*}{K_B T}\right) - 1 \right); \quad (6.9a)$$

$$\Gamma_M = \frac{ev\gamma_0\left(\Delta E_c^0 + \Delta E_h^0\right)}{(\pi a^2 t^2)^2}. \quad (6.9b)$$

In contrast to the forward bias current, there is an additional power of $k_B T$ in the reverse bias current, which arises from the density of available electron states in $MoSe_2$.

Equation (6.9) indicates that in the V_{SD} and temperature regime in which e-h pair multiplication is the dominant source of current, the reverse bias current can be re-expressed in terms of a temperature-independent quantity that depends on $\Delta E^0{}_h$. The reverse bias I-V_{SD} characteristics, when rescaled as $T\ ln(I_M/T^2)$ as in equation (6.9), should collapse to a single line. In this case, the voltage dependence of $T\ ln(I_M/T^2)$ exhibits universal behavior, with a linear increase with V_{SD}.

While equation (6.9) gives the temperature scaling of the current due to e-h pair multiplication, an additional straightforward analysis is required to obtain $\Delta E^0{}_h$. First, note that equation (6.9) contains a V_{SD}-independent term and a V_{SD}-dependent term. In order to isolate the activation energy $\Delta E^0{}_h$, we simply take the derivative dI_M/dV_{SD} of equation (6.9), giving

$$\frac{|dI_M/dV_{SD}|}{(2\Gamma K_B T)} = \exp(-K_e^*/K_B T). \quad (6.10)$$

Equation (6.10) indicates that the quantity $(dI_M/dV_{SD})/T$ vs. $1/T$ should exhibit an exponential decrease, from which the activation energy $K^*{}_e$ can be extracted.

6.6 Gate and Temperature Dependence of dlogI/dVG of 2L-WSe_2/$MoSe_2$

The model described in sections 6.3 and 6.4 makes a number of predictions that can be compared to experiment. First, as the reverse bias voltage is increased, hot electrons with kinetic energy that exceeds K^*_e may generate interlayer e-h pairs (Fig. 6.4e), which are subsequently separated into the constituent electron and hole. Impact excitation is expected to generate additional conduction electrons at the interface. As a consequence, the onset gate voltage V_{ON} is lowered for negative V_{SD}, while it is not affected for $V_{SD} > 0$ V.

We examine the gate voltage dependence of the interlayer current to test this conjecture. Figure 6.9a shows a color map of $dlogI/dV_G$ vs. V_G and V_{SD} taken at $T = 340$ K. At $V_{SD} > 0$ V, we observed a vertical peak feature in the $dlogI/dV_G$ map that occurs near $V_G = -36$ V. We label this gate voltage, which remains constant in forward bias, as V^+_{ON} in Figure 6.6a. Such standard behavior does not include the effects of e-h pair multiplication. In contrast, horizontal line traces of $dlogI/dV_G$ in reverse bias (Fig. 6.6a bottom) show that V_{ON} decreases approximately linearly with increasing negative V_{SD}. This response is consistent with the e-h pair production process of equation (1): additional electrons generated in the $MoSe_2$ conduction band increase the electron density in the unipolar interlayer channel, thus lowering the gate voltage required for the onset to conduction.

Our model also predicts that by reducing temperature, impact excitation and charge multiplication are suppressed. To see this, Figure 3.10b shows the temperature evolution

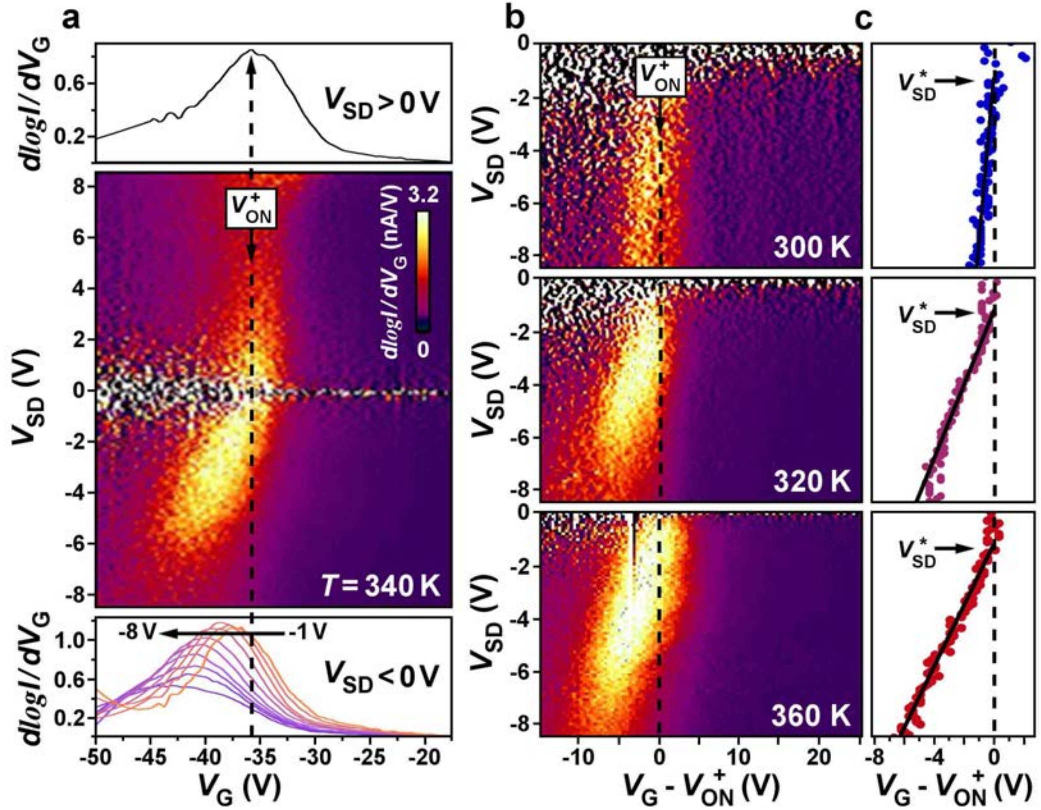

Figure 6.6. Gate voltage, source-drain voltage, and temperature dependence of $dlogI/dV_G$ in the atomic layer semiconductor heterostructure device. a, Color map of $dlogI/dV_G$ vs. V_G and V_{SD} (T = 340 K). Top, $dlogI/dV_G$ vs. V_G characteristic at V_{SD} = 2.0 V. Vertical dashed line labels the maximum value of $dlogI/dV_G$ in forward bias, denoted V_{ON}^+. Bottom, $dlogI/dV_G$ vs. V_G characteristics for increasing negative V_{SD} from V_{SD} = -1.0 V (yellow line) to V_{SD} = -8.5 V (purple line). **b**, $dlogI/dV_G$ vs. V_G and V_{SD} for negative V_{SD}. The gate voltage axis is shifted by V_{ON}^+ (vertical dashed line) extracted at each temperature. **c**, Maximum values of $dlogI/dV_G$ extracted at each temperature. V^*_{SD} labels the intercept of the linear fits of the maxima and V_{ON}^+ .

of the $dlogI/dV_G$ maps in reverse bias. At each temperature, we extract the maximum values of $dlogI/dV_G$ as a function of V_G and V_{SD} (Fig. 6.6c). At T = 300 K, the onset gate voltage shifts only slightly below V^+_{ON} (vertical dashed lines Fig. 6.6c) as the reverse bias

V_{SD} is increased, indicating that no additional charge is generated at the interface. Above T = 320 K, as the source-drain voltage increases above the threshold V^*_{SD} = -1.2 V, the onset gate voltage V_{ON} decreases approximately linearly with increasing negative V_{SD}. The appearance of this feature, in which V_{ON} decreases linearly with negative V_{SD}, correlates directly with the temperature-dependent increase of the interlayer current (Fig. 6.4).

The very low threshold voltage V^*_{SD} shown in Figure 6.4b highlights an important aspect of hot carrier-enhanced e-h pair generation. The interlayer transport process $e_W \rightarrow e_{Mo}$ transfers a low-energy electron in the WSe_2 conduction band into a hot electron above the conduction band edge in $MoSe_2$ (Fig. 6.5). Impact excitation generates additional charge density only if the excess kinetic energy exceeds K^*. V_{ON} is therefore reduced below V^+_{ON} once the source-drain voltage exceeds a critical energy $eV^*_{SD} > 1.2$ eV (labeled in Fig. 6.6c). The threshold voltage V^*_{SD} for interlayer e-h pair generation is lower than the energy-conservation limit for excitation of intralayer bound e-h pairs in either $MoSe_2$ ($\Delta E_{Mo}/e$ = 1.57 V) or $2L$-WSe_2 ($\Delta E_W/e$ = 1.46 V).

6.7 Power Dependence of I-VSD Characteristics of 2L-WSe$_2$/MoSe$_2$

So far in this chapter we explicitly discussed hot carrier-enhanced interlayer impact excitation through electronic transport experiments of $2L$-$WSe_2/MoSe_2$. Here we study this phenomenon through optoelectronic experiments. Figure 6.7a shows interlayer photocurrent characteristics measured as a function of temperature at low optical power (17 μW) and λ = 900 nm. When $V_G < V_{ON}$, the dark current (black line trace Fig. 6.7) is

strongly suppressed since the N^+-N heterojunction formed at the interface is depleted of conduction electrons. Under local optical illumination of the heterostructure, we observed dramatic increase in the reverse bias photocurrent with increasing temperature. In contrast, the photocurrent at $V_{SD} > 0$ shows negligible temperature dependence. The prominent enhancement of the reverse bias photocurrent is fully consistent with equation (1): an optically excited e_W electron in the conduction band of WSe_2 undergoes efficient multiplication into an e_{Mo} electron and additional e-h pairs.

Remarkably, we find that the $MoSe_2$/2*L*-WSe_2 photocells exhibit a responsivity enhancement that exceeds 350%. To quantify the multiplication factor, we measured the detailed power dependence at each temperature (power dependence for T = 300 K shown in Fig. 6.7b) and examined the ratio of the responsivity R at elevated temperatures to that at T = 300 K. Since impact excitation is suppressed at low temperatures, the ratio R_{350} / R_{300} gives a lower bound estimate of the multiplication enhancement. Figure 6.10c shows the multiplication enhancement factor R_{350} / R_{300} as a function of V_{SD} for various optical powers. At low power (blue data), the enhancement factor exceeds 3.5 and shows a clear peak near V_{SD} = -2.8 V. At high optical power (red data) the enhancement is reduced, likely resulting from increased electron-hole pair annihilation or thermal effects. Of key importance, the maximum multiplication near V_{SD} = -2.8 V corresponds very closely to the peak conductance g_M due to e-h multiplication in the absence of light (Fig. 3.4d). This direct correspondence further highlights the ultra-low V_{SD} threshold for hot carrier-enhanced impact excitation.

The extraordinary efficiency of the $e_W + Ke \rightarrow e_{Mo} + (e_{Mo} + h_W)$ process at elevated temperatures is an unexpected result. Normally, relaxation mechanisms such as optical phonon emission are very efficient for relaxing hot electrons, including those in individual monolayer TMDs[8]. In contrast, the $e_W \rightarrow e_{Mo}$ process observed here produces hot e_{Mo} electrons that subsequently relax excess kinetic energy equal to ΔE_h^0. Multiplication dominates over ordinary interlayer electron transfer, and thus the reverse bias current depends sensitively on ΔE_h^0 and temperature. According to equation (2) in section 3.8, I_M contains a temperature-dependent pre-factor of $(k_B T)^9$. This factor arises from the increased density of states available to hot e_{Mo} electrons during impact excitation (Fig. 6.5), and does not arise in forward bias (section 6.5.1).

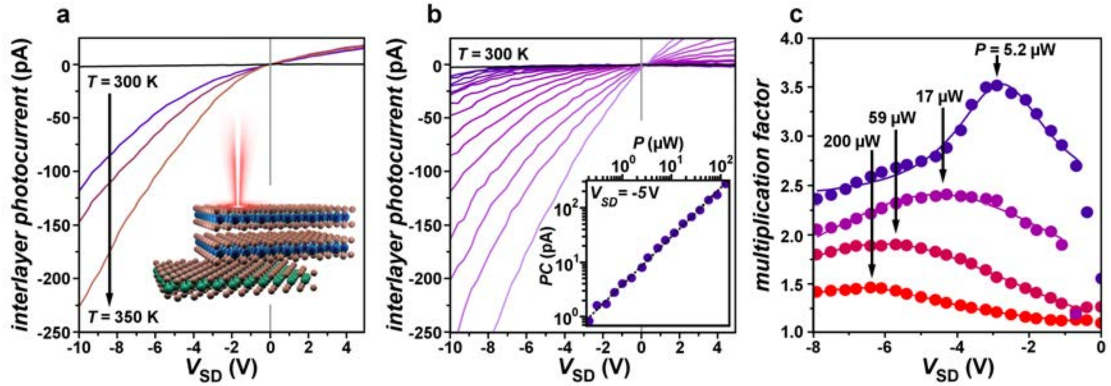

Figure 6.7. Interlayer photocurrent characteristics and multiplication enhancement in the 2D heterojunction photocell. a, Interlayer photocurrent vs. V_{SD} at T = 300, 340, and 350 K with $V_G < V_{ON}$; black line trace is the dark I-V_{SD} characteristic. Optical illumination is focused at the heterostructure with a laser at λ = 900 nm, P = 17 μW. (see inset schematic) b, Interlayer photocurrent vs. V_{SD} for increasing optical power at T = 300 K. Inset, photocurrent vs. power at V_{SD} = -5 V. c, Multiplication factor determined from the ratio of the responsivities R_{350} / R_{300} at various optical power levels (labeled). Solid lines are Lorentzian fits used to determine the peak multiplication value.

The differential conductance in reverse bias is given by $g = dI_M/dV_{SD} \approx 2eI_M / k_BT$ (Section 6.5.2 equation 10), suggesting a linear relationship between $ln(g/T)$ and $1/T$ with a slope of $-K_e^*$. Figure 6.4c inset shows the data $ln(g_M/T)$ vs. $1/T$ over a range of temperatures. From the slope of the linear fit ($-K_e^*$) and equation (6.3) in section 6.7, we obtain the interlayer e-h pair excitation energy $\Delta E_h^0 = K_e^* + \Delta E_c^0 = 1.0$ eV. The value obtained from transport data agrees well with ΔE_h^0 (theory) = 0.94 eV (Fig. 2.5).

Hot electron impact excitation results in a highly efficient energy relaxation process that differs strongly from conventional impact ionization. In the TMD heterostructure photocells, no avalanche breakdown behavior is observed, giving additional insight into the origin of the NDC in Figure 6.3. While NDC is often attributed to tunneling behavior, here the NDC is due to the competition between multiplication and e-h pair recombination. Recent measurements of 2D heterostructures have suggested that Shockley-Read-Hall (SRH) and Langevin processes dominate the unusual recombination of interlayer e-h pairs[9-11]. In the devices demonstrated here, the multiplication-recombination competition results in a peak in the dark I-V_{SD} characteristics (Fig. 6.3c) and a corresponding reduction of the multiplication enhancement factor at high negative V_{SD} (Fig. 6.10b). While in standard semiconductors, competing energy relaxation mechanisms restrict carrier multiplication to extremely large biases[12]; interlayer impact excitation dominates at very low applied V_{SD} bias. Such remarkable behavior may enable enhanced energy transfer, power conversion efficiency, and light emission processes that take advantage of the layer-indirect nature of 2D heterostructure e-h pairs.

6.8 Comparison of the Model to Experimental Data

Our simple model agrees well with the temperature dependence observed in Figure 6.7, but may not capture all details of the interlayer transport processes at all biases. Importantly, we note that the model agrees well only within the voltage regime leading up to the onset of NDC (-3 V < V_{SD} < -0.5 V). Within this voltage regime, α remains constant and can be extracted from the temperature-dependent data such as that shown in Figure 6.4c. The obtained value for the device of Figure 6.3, α = 0.2, is typical for TMD heterostructure devices studied here, and likely arises from a combination of contact resistance, resistance drop across the individual materials, as well as intralayer recombination processes. Figure 6.8 shows I-V_{SD} characteristics over the range of voltages that can be well described by our model. The rescaled current $Tln(I/T^2)$ changes approximately linearly with V_{SD} over the range -3 V < V_{SD} < -0.5 V and for increasing values of V_G near the onset threshold. $Tln(I/T^2)$ also increase linearly with V_G over the range of voltages -37 V < V_G < -31 V, which is precisely the onset regime. The linear dependence on V_{SD}, and the corresponding constant value of α over this voltage regime strongly suggests that the potential drop across the interface scales proportionally to the applied voltage in a similar way over the entire voltage range near the onset to NDC. Of importance, the voltage drop along the lateral direction of the interface may depend on the device current, which in turn influences the voltage drop across the junction. While this is not explicitly treated in our model, the details of this effect are captured qualitatively in the phenomenological factor α. While a detailed treatment would require microscopic understanding of the interlayer transfer rates and the exact origins of α, we

exclude this subtle effect since α remains constant over the voltage regime of interest, thus allowing us to capture the basic temperature dependent behavior. At very low bias (V_{SD} < 0.5 V), the regime in which the current does not match the behavior in our model, α is difficult to extract since the current does not increase exponentially. As suggested in Chul-Ho Lee, et al.[13], this likely results from the lateral voltage drop or the non-exponential behavior due to recombination effects. At very high voltage (above NDC), we observe an additional feature of carrier multiplication: an enhancement of the device noise due to impact excitation.

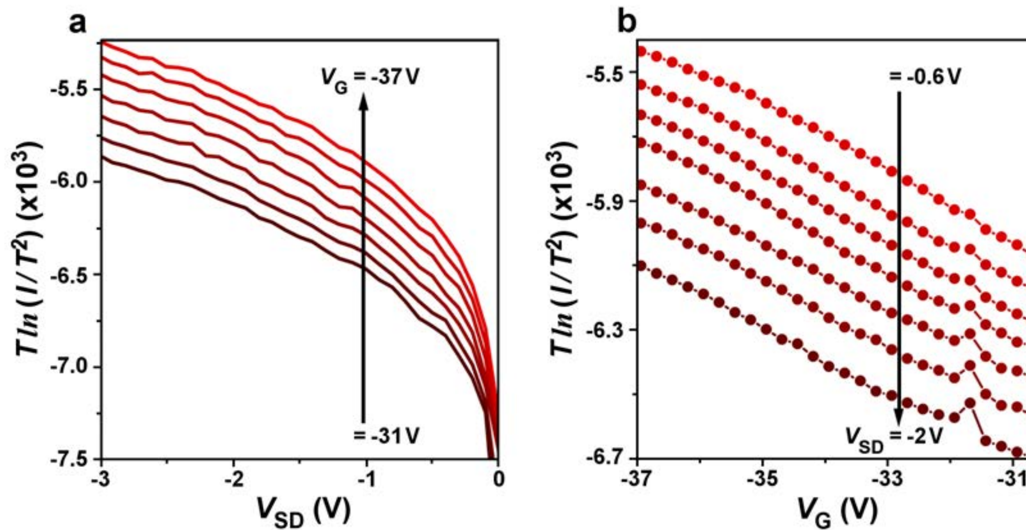

Figure 6.8. Interlayer current-voltage characteristics in the transport regime near the onset to NDC. a, Reverse bias I-V_{SD} characteristics, rescaled as described in Section 3.9.1. b. I-V_G characteristics with the same rescaling shown at various values of V_{SD}.

At T = 360 K, the efficiency of impact excitation increases, leading to significant noise at high voltage. While this behavior may result from random current fluctuations due to carrier multiplication, it is not well described by the hot-carrier enhanced impact

excitation model below the threshold. Future work will focus closely on exploring the impact excitation noise factor to explore noise in the carrier multiplication process.

6.9 Photoresponse of the Atomic Layer Hetero-Junction

For the assessment of the multiplication factor, we were very careful to photoexcite only within the WSe_2 absorption edge while avoiding optical absorption in the (overlapping) low energy tail of the $MoSe_2$ absorption peak. Absorption in $MoSe_2$ may result in complicated interlayer transfer processes and additional state filling that may skew the determination of the multiplication factor. From Figures 5.2 and 5.4, we show that the heterostructure exhibits somewhat weak, but easily measured photoluminescence and photocurrent response at photon energy 1.38 eV (corresponding to λ = 900 nm). While this energy is slightly below, but still within the absorption peak of the e_W transition, we chose this wavelength to avoid as much as possible any absorption in the low energy tail of the $MoSe_2$ absorption edge, which begins to become non-negligible as the photon energy increases above 1.4 eV (Figure 5.4).

Figure 6.9 shows photocurrent I-V_{SD} characteristics taken at increasing photon energies and T = 300 K (in the regime of inefficient impact excitation) with the laser power fixed at P = 17 μW. While the overall photoresponse at 1.38 eV is comparatively weak, the photocurrent results primarily from absorption in WSe_2 rather than combined absorption within the absorption bands of WSe_2 and $MoSe_2$. As the absorption of $MoSe_2$ becomes important at higher energies, the overall photoresponse increases proportionally. At higher photon energies, a careful assessment of the multiplication factor is less

dependable, as it must include the additional effects of current flow and interlayer transfer caused by absorption in both layers. Future work will examine the detailed photon energy dependence of impact excitation process by probing the intricate dependence of photocurrent on photon energy, voltage, and temperature.

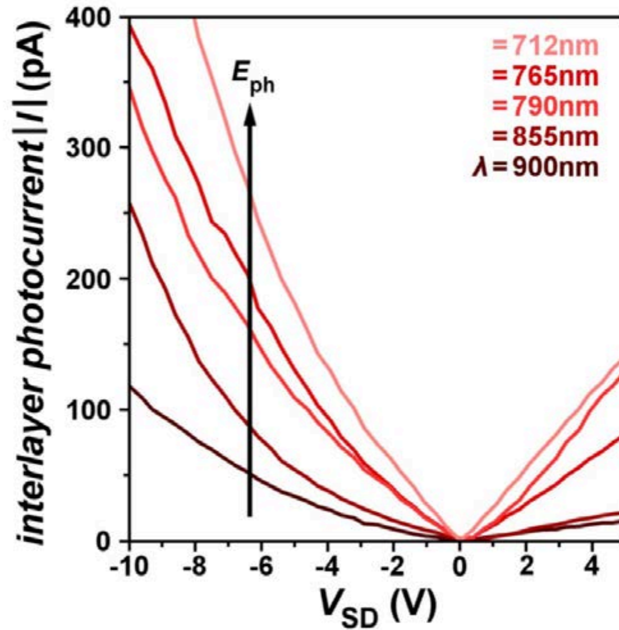

Figure 6.9. Wavelength dependence of the interlayer photocurrent-voltage characteristics at T = 300 K. Photocurrent (absolute value) vs. V_{SD} measured as a function of decreasing wavelength (increasing photon energy) at fixed power = 17 μW. Photon energies are E_{ph} = 1.38 eV, 1.45 eV, 1.57 eV, 1.62 eV, and 1.74 eV from bottom to top. For comparison, the black line trace is the same data shown in main text Figure 6.1a (T = 300 K, Ephoton = 1.38 eV).

6.10 2D-TMD N^+-N Heterojunction Characteristics

The global back gate voltage V_G allows electrostatic doping of the $MoSe_2$/*2L*-

WSe_2 interface, which is produced by mechanical exfoliation of bulk TMD crystals followed by van der Waals-mediated pick-up, dry transfer, and high vacuum annealing (See sections 3.4 & 3.5 for details). Assembling the individual TMDs into a heterostructure results in a built-in potential energy difference across the interface characterized by the band offset energy ΔE_c^0 (ΔE_v^0) of the two conduction (valence) bands (Fig. 6.10a). An electron transiting the interface from WSe_2 into $MoSe_2$ experiences the potential energy drop, while an electron travelling in the opposite direction must gain sufficient kinetic energy to overcome the potential energy barrier ΔE_c^0. At the heterostructure interface, the energy difference ΔE_h^0 between the highest valence band and lowest conduction band is the minimum energy required to excite an interlayer e-h pair.

Figure 6.10b shows the current I as a function of gate voltage V_G at source-drain voltage V_{SD} = 0.65 V. The I-V_G characteristic demonstrates ordinary unipolar electron-type (N- type) semiconductor heterojunction behavior: current that increases monotonically at low V_{SD} and a well-defined transition from insulating behavior at V_G = -50 V to conducting behavior at V_G = 10 V. From the I-V_G characteristic, we compute $dlogI/dV_G$ and find the maximum, which determines the onset gate voltage V_{ON} = -35.5 V. For gate voltages above V_{ON}, electrons are transferred through the N^+-N heterojunction formed at the interface of the heavily electron-doped (N^+) $MoSe_2$ and lightly electron-doped (N) WSe_2.

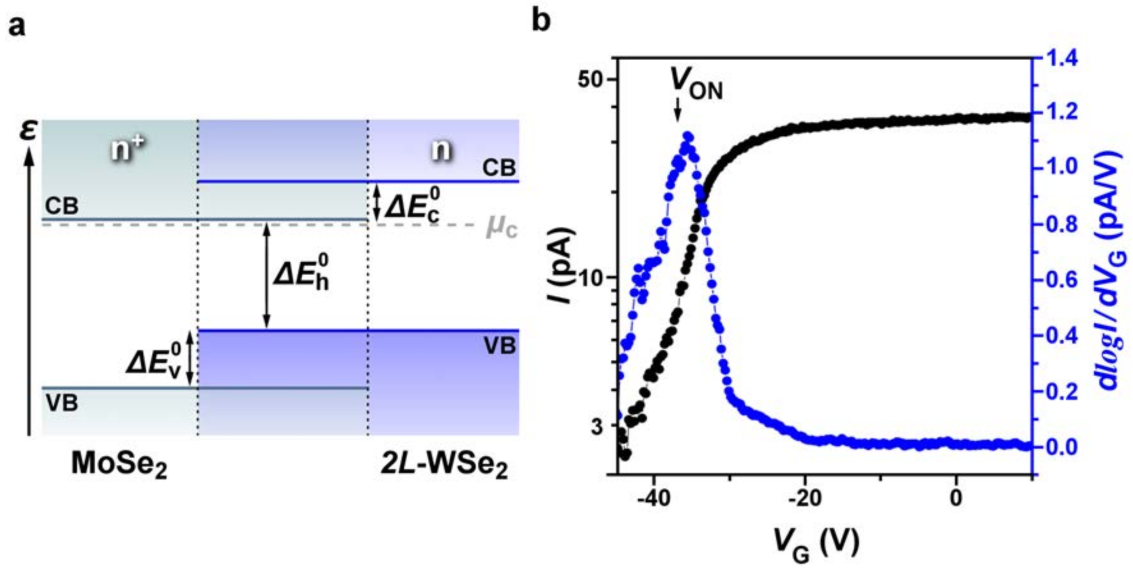

Figure 6.10. Band structure, and current-voltage characteristics of the 2D semiconductor heterostructure device. a, Electronic energy band diagram of the N^+-N heterojunction at V_{SD} = 0 V, showing the conduction bands (CB), valence bands (VB), and chemical potential μ_c in equilibrium (dashed gray line). b, Device current I (black) and $dlogI/dV_G$ (blue) vs. gate voltage V_G (V_{SD} = 0.65 V; T = 340 K).

REFERENCES

1. Barati, F. et al. Hot carrier-enhanced interlayer electron–hole pair multiplication in 2D semiconductor heterostructure photocells. *Nat. Nanotech.* **12**, 1134–1139 (2017).

2. Lee, C. et al. Atomically thin p–n junctions with van der Waals heterointerfaces. *Nat. Nanotechnol*. **9**, 676-681 (2014).

3. J. Kang, S. Tongay, J. Zhou, J. Li and J. Wu, Band offsets and heterostructures of two-dimensional semi- conductors, *Appl. Phys. Lett*., 2013, **102**(1), 012111–012114.

4. Nourbakhsh, A., Zubair, A., Dresselhaus, M., & Palacios, T. Transport Properties of a MoS2/WSe_2 hterojunction transistor and its potential for application. *Nano Letters* **16**, 1359-1366 (2016).

5. Datta, S., *Electron Transport in Mesoscopic Systems*. (Cambridge university Press, *Cambridge, 1995).*

6. Lee, C. et al. Atomically thin p–n junctions with van der Waals heterointerfaces. *Nat. Nanotechnol.* **9**, 676-681 (2014).

7. Furchi, M. M., Pospischil, A., Libisch, F., Burgdörfer, J. & Mueller, T. Photovoltaic effect in an electrically tunable van der waals heterojunction. *Nano Lett.* **14**, 4785-4791 (2014).

8. Movva, H. C. P. et al. High-mobility holes in dual-gated WSe_2 field-effect transistors. *ACS Nano* **9**, 10402-10410 (2015).

9. Rivera, P. et al. Valley-polarized exciton dynamics in a 2D semiconductor heterostructure. *Nat. Commun.* **6**, 1-6 (2015).

10. Rivera, P. et al. Observation of long-lived interlayer excitons in monolayer MoSe2– WSe_2 heterostructures. *Science* **351**, 688-691 (2016).

11. Lee, C. L. et al. Atomically thin p–n junctions with van der Waals heterointerfaces. *Nat. Nanotechnol.* **9**, 676-681 (2014).

12. Sze, M. & NG, K. K. *Physics of Semiconductor Devices.* (Wiley-Interscience publications, United States, 1963).

13. Lee, C. et al. Atomically thin p–n junctions with van der Waals heterointerfaces. *Nat. Nanotechnol.* **9**, 676-681 (2014).

CHAPTER 7

PHONON-ASSISTED ANTISTOKES UPCONVERSION IN A VAN DER WAALS HETEROSTRUCTURE P-N JUNCTION PHOTOCELL

7.1 Laser Cooling of Semiconductors

Laser cooling of solids, and more specifically semiconductors, has recently attracted a lot of interest. Laser cooling is most commonly used for cooling and trapping atoms and ions to extremely low temperatures. Surprisingly, the concept of laser cooling of solids or optical refrigeration was proposed by Pringsheim in 1929[1], nearly half a century before Doppler cooling of atoms was contemplated and well before the invention of the laser. In the solid phase, thermal energy is due to vibrational modes of the lattice (phonons). For a given electronic transition, photons in the low energy (red-shifted) tail of the absorption maximum may be absorbed, followed by spontaneous emission of more energetic (blue-shifted) photons. During the emission process, the energy difference between absorption and emission is extracted from lattice thermal vibrations (phonons) through a process known as anti-stokes process. In order to demonstrate laser cooling in any system, the key requisite is to demonstrate the anti-stokes absorption processes.

Historically, material purity problems prevented the observation of this type of laser cooling until 1995, when it was first demonstrated in ytterbium-doped glass[2], a rare earth doped material (RE). Soon after this successful observation of net cooling, attention

was directed towards cooling matter in various condensed phases, beyond RE materials. The desire to achieve much lower temperatures than RE doped systems, as well as the search for direct integration into existing semiconductor-based devices, has placed the focus of numerous theoretical and experimental investigations of laser cooled solids on semiconductors. Experiments recently conducted on bulk GaAs heterostructures[3], as well as CdS bulk and nanostructures[4], have shown promising results, motivating a strong interest in laser cooling of semiconductors even without the demonstration of net cooling. Semiconductor cooling could provide more efficient pump light absorption, the potential of much lower temperatures, and the opportunity for direct integration into electronic and photonic devices for low temperature operation. In principle, the existence of a continuum of states outside the direct band gap characteristic of many semiconductors could allow such materials to get much colder (temperatures ~10 K and below) than RE materials (limit of ~100 K)[5].

7.2 Preliminary Optical Characterizations

In this chapter we study phonon assisted anti-stokes absorption in a 2D heterostructure photocell composed of a bilayer tungsten diselenide (*2L*-WSe_2) stacked on top of a monolayer molybdenum diselenide ($MoSe_2$) on a Si/SiO_2 substrate integrated into a field effect heterojunction device. A back-gate voltage controls the doping level of carriers between the layers of the heterostructure. Source-drain contacts give electrical access to each layer in order to apply voltage to one layer and collect the interlayer current from the other (Fig. 7.1a).

The heterostructure studied here is unique in that two atomically thin materials form an interface between atomic systems with many fewer atoms than bulk solid-state systems. The first step towards exploring anti-stokes absorption is to be able to make high quality devices exhibiting a high level of control over different parameters of the system. In chapter 3 we discussed in detail the process to make very clean and high quality devices. We studied the characteristics of this heterostructure when it forms an N^+-N heterojunction (see Chapter 1 section 5.1). We also discussed how a P-N junction (see Chapter 1 section 5.2) can be formed by tuning the Fermi level, giving us the ability to electrostatically tune the carrier density at the interface. In the P-N junction regime, we uniformly tune the heterostructure, balancing electrons and holes to reach the charge neutrality condition. As we will show, under this charge neutral condition, we are able to more fully explore phenomena like anti-Stokes absorption.

Figure 7.1b illustrates the Raman spectra taken from both the individual layers and the heterostructure. We used a Horiba LabRAM HR spectrometer with an excitation of 532 nm, with working range of 100 cm^{-1} to 9700 cm^{-1}. Measurements are performed at room temperature with the power of excitation laser at 2 mW. For the monolayer $MoSe_2$ we observed a very active mode at 30 meV (241 cm^{-1}), and another mode at 36 meV (289 cm^{-1}). The first Raman active vibrational mode is assigned to an out of plane vibration of A′ while the second not very active mode to an in-plane vibration of E^1_{2g}, For bilayer WSe_2 we found a very active Raman mode at 31 meV (250 cm^{-1}), and two other modes at 31.7 meV (256 cm^{-1}) and 38 meV (308 cm^{-1}).

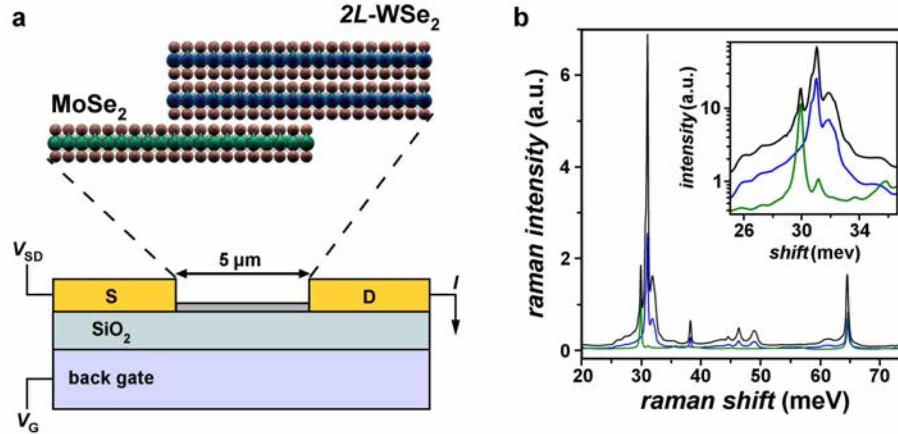

Figure 7.1. Device configuration, and Raman Spectra. a, (top) Schematics of the atomic layer heterostructure (bottom) and the n-p heterojunction device with a Si/SiO_2 back gate and source drain electrodes (heterostructure overlap area 6 μm^2). b, Raman (λ = 532 nm) from $MoSe_2$ (green), *2L*-WSe_2 (blue), and the heterostructure (black). b**,** (inset) Raman zoomed in closeup right around the very active area (30 meV).

Our measurements show excellent agreement with previous studies[6-8], attributing these vibrational modes to monolayer $MoSe_2$ and bilayer WSe_2. The first modes near 30 meV in WSe_2 are assigned to E^1_{2g} and A^1_g respectively[7,8]. In E^1_{2g} vibrational mode two in phase Se atoms oscillate in opposite to a W atom at each layer and the two layers oscillate laterally opposite to one another, while in A^1_g mode Se atoms oscillate in opposite phase, out of plane with respect to W atoms. Raman spectra taken from the heterostructure (black line) has a contribution of both layers, and it shows the feature of the constituent materials and nothing else. According to figure 7.1c the most dominant feature of Raman is around 30 meV, and the inset shows details of these features on a log scale. According to reported literature[6,7], these features are due to low frequency optical phonon modes in the atomically thin system.

7.3 Spectral Imaging of High-Energy Excitation

Using the custom-built instrumentation presented in chapter 4, we fix a Gaussian beam on the overlapped region of the heterostructure and tune the photon excitation energy within a range between 1.37 - 1.55 eV (equivalent to wavelength within 800-900 nm) while measuring the interlayer photocurrent. Figure 7.2a shows the interlayer photocurrent vs. photon excitation energy and gate voltage. Tuning the system to positive gate voltage, the device is in the N-N configuration, and we observe several photocurrent features as a function of photon energy. Moving towards zero gate voltage values, these features disappear as we reach the charge neutral condition. As the gate voltage is tuned in the negative direction, we again observe photocurrent features as the device enters the P-N configuration.

To examine this behavior more carefully, Figure 7.2b shows the photocurrent as a function of photon excitation energy taken at V_G = -2 V from figure 7.2a. We observe a feature at 1.53 eV right around the PL peak position of $MoSe_2$. Tracking this feature down over gate voltage (figure 7.2c), we observed no redshift. Neutral exciton does not change with respect to electrostatic doping while charged exciton does; hence this feature is labeled the neutral exciton of $MoSe_2$ (X^0_{Mo}). The second feature n figure 7.2 b is observed at 1.49 eV, with a redshift of the amount of 21 meV (Fig. 7.2 c). This feature is consistent with $MoSe_2$ trion peak (X^+_{Mo}) in two ways, first that it happens in the right energy as other people have seen[10], and second it redshifts like we would expect trions to redshift[11]. The third feature is observed at 1.44 eV with the redshift of 54 meV, consistent

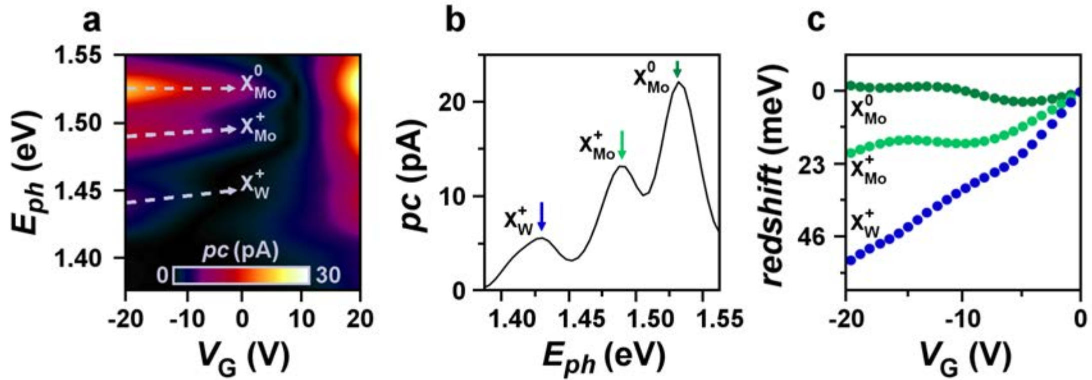

Figure 7.2. Gate voltage dependence of the excitation photon energy of the P-N atomic layer heterostructure under high excitations. a, Color map of excitation energy (1.37 eV to 1.55 eV) vs. V_G at a fix V_{SD} = +6 v (T = 300 K). b, Interlayer photocurrent vs. excitation photon energy that shows the existence of three peaks, neutral exciton peak in $MoSe_2$ at 1.52 eV, positive exciton peak in $MoSe_2$ at 1.49 eV, and positive exciton peak in WSe_2 at 1.44 eV. c, Red shift of the peak positions versus gate voltage, neutral exciton in $MoSe_2$ (in dark green), positive exciton peak in $MoSe_2$ (in medium green), and positive exciton peak of WSe_2 (in blue).

with charged exciton of WSe_2 ($X^+{}_W$). The important point here is that by tuning the gate voltage from -20 V towards zero we are basically pulling ions out of the system and depleting the system completely from ions, so by the time that we reach -2 volts all we are left with are primarily the neutral excitons. This is the gate voltage where the most asymmetric diode characteristic of the device (P-N junction behavior) happens in the system (discussed in details in section 7.5).

7.4 Spectral Imaging of Low-Energy Excitation

Being able to deplete the system from charged excitons by moving towards V_G = -2V we are only left with neutral excitons at the interface of the heterostructure. Observation of antistokes process requires having a clean system free from charged

carriers and being able to photoexcite the two-level system with controllable photons. Next we tune the photon energies below the energy gap of the interface and measure photocurrent as a function of photon excitation energy and gate voltage. Figure 7.3a shows a color map of photon excitation energy between 0.88-1.03 eV (λ = 1200-1400 nm), and gate voltage between -20 to +20 volts taken at 16 K. Looking at the data we observe three weird things, the first one is that a very strong photocurrent response happens around 1 eV and only at V_G = -2 V. 1 eV is the interlayer gap at the interface that we found from flat band condition that is discussed in 1.5.2 from fig.1.8 and also from our old calculations[12].

The second weird thing observed in fig.7.3a is that not only we observed a strong photocurrent response at 1 eV but also some other resonances that happen at lower and lower energies. Finally, the third weird thing we observed is that these small features increment in energy at about 30 meV away from each other, very interestingly this is the energy value where Raman was very strong.

Figure 7.3b illustrates interlayer photocurrent as a function of photon excitation energy at gate voltages of -2, 0.7, 0.2, 3.5, and 5.0 volts respectively from top to bottom. Photocurrent at V_s = -2 V is where we get the strongest response. In order to identify the position of these features we applied lorentzian fit to photocurrent data at V_G = -2 V and found the average position of the peaks being at 1.01, 0.98, 0.95, 0.92, and 0.89 eV, with energy difference of about 30 meV from each other, Raman was very active at this energy value. The first peak labeled X_I is the energy required for an indirect interlayer

exciton to form at the interface. We then observed photocurrent suppression in the small features at higher gate values where system is not charge neutral.

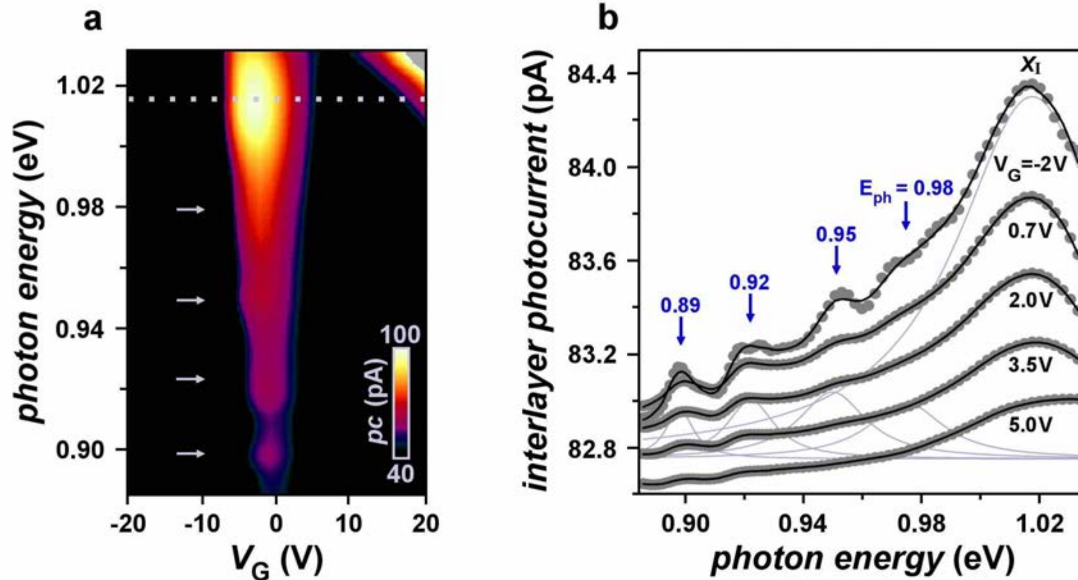

Figure 7.3. Low energy excitations. a, Color map of excitation energy vs. V_G (T = 16.7 K). b, Interlayer photocurrent vs. excitation energy characteristics as a function of gate voltage.

7.5 2D-TMD P-N Heterojunction Characteristics

We can also integrate TMDs into semiconductor photodiodes and study the optoelectronic characteristics. The electronic energy band diagram of a similar heterostructure incorporated into a photocell device is shown in figure 7.4a. A band offset between the two conduction (valence) bands at V_{SD} = 0 V results from the built-in potential energy difference across the interface. The energy gap between the lowest conduction band and the highest valence band in the system is large enough to form an interlayer exciton (X_I) when photo-exciting the device. Chemical potential at equilibrium

lives in a medium regime between the lowest conduction and highest valence bands, which forms a charge neutrality condition.

Applying a positive back gate voltage, shifts the Fermi level up by increasing the electron concentration in the system, making both layers N-type ($MoSe_2$ more N-type than WSe_2), creating an N^+-N heterojunction photocell (discussed in section 1.5.1). Now we apply negative gate voltage to the device, it shifts the Fermi level down by increasing the hole concentration in the system, so the Fermi level would be between the conduction band edge of $MoSe_2$ and the valence band edge of WSe_2, making $MoSe_2$ more n-doped with electrons as the majority carriers and WSe_2 more P-doped with holes accumulation at the band edge, creating a P-N heterojunction photocell. Black arrow in figure 6.4a labeled X_I indicates the photogenerated interlayer excitons in which its electrons belong to $MoSe_2$ layer and holes to WSe_2 layer.

Spatially distributed charge at the interface of the heterostructure is shown in figure 6.4b top. Applying a source-drain voltage (figure 7.4c) can tune the potential drop (ϕ), to reduce the potential barrier width and make the carriers transfer easier (forward bias behavior of a rectifier) or increase the barrier width (the behavior of a rectifier under reverse bias). If the applied V_{SD} is large enough it can flatten the bands by taking ϕ to zero, in this case the voltage is called flat band voltage[2]. Flat band voltage is proportional to the activation energy needed to generate an interlayer exciton $\phi = X_I - eV_{SD}$, when $\phi = 0$, $X_I = eV_{FB}$. A color map of the photocurrent with the excitation wavelength of $\lambda = 800$ nm, as a function of V_{SD} vertical axis and V_G horizontal axis is shown in figure 6.5a, data is taken at low temperature of 16.7 K.

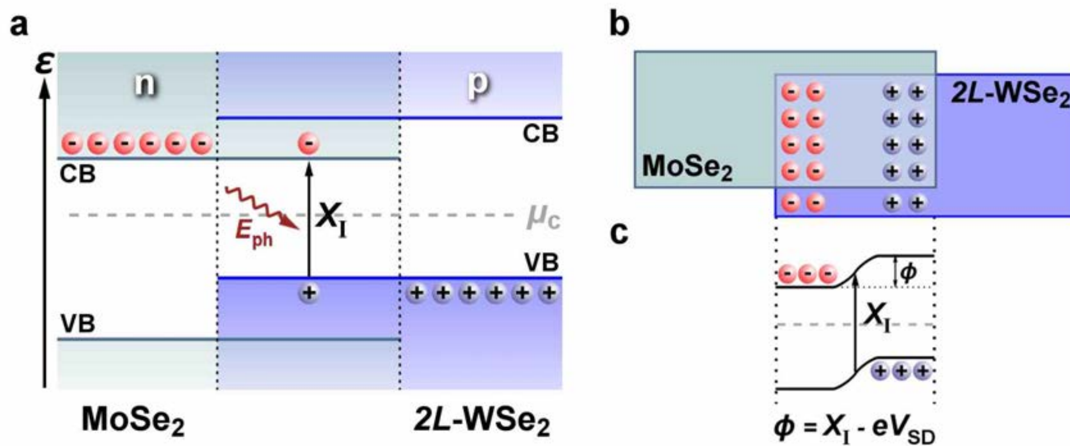

Figure 7.4. Band structure, and interlayer charge transfer at the P-N junction of *2L*-WSe_2/$MoSe_2$. a, Electronic energy band diagram at $V_{SD} = 0$ V, showing the conduction bands (CB), valence bands (VB), and chemical potential μ_c in equilibrium (dashed gray line). b, Spatially distributed charges at the interface, *2L*-WSe_2 is more p-doped and $MoSe_2$ is accumulated with negative electrons. c, Electronic band diagram of the interface, applying V_{SD} changes the height of the barrier ϕ.

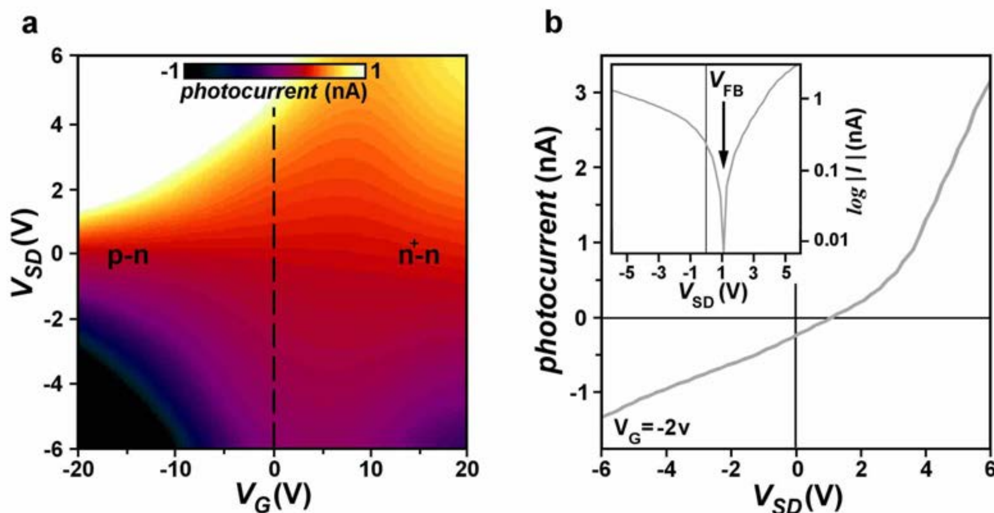

Figure 7.5. Gate voltage dependence of I-V_{SD} characteristics under illumination and in the absence of light. a, Color map of I vs. V_{SD} and V_G ($T = 16.7$ K) under illumination of $\lambda = 800$ nm. b, I-V_{SD} characteristics taken from color map at $V_G = -2$V, the onset of the P-N junction regime. b, (inset) absolute value of log scale of I-V_{SD} with an arrow indicating the flat band voltage at 1 volts.

It shows an N^+-N junction behavior at positive gate voltages and a P-N junction characteristic in negative gate values. The onset of the P-N heterojunction behavior is right around V_G = -2 V. Figure 7.5b depicts photocurrent as a function of V_{SD} at V_G = -2 V where it has the most asymmetric diode characteristic similar to a P-N junction.

In a P-N junction photodiode, the position where the I-V_{SD} curve passes through zero-photocurrent axis is called flat band voltage (explained in details in Fig. 7.4c), in the fourth quadrant (where $V_{SD} > 0$ and $I < 0$) electrical power is been generated within the photodiode. The inset in figure 6.5b illustrates the absolute value of the I-V_{SD} curve, it shows that the cross over voltage is happening at V_{FB} = 1V, it implies that the activation energy needed in this system to generate an interlayer exciton is about 1 eV.

7.6 Phonon-Assisted Antistokes Shift

Band profile in the lateral direction is depicted in Figure 7.6a, it shows the spatially indirect exciton formation at the interface of $MoSe_2$ and *2L*-WSe_2, by photoexciting the heterostructure with a controllable photon energy the electron in conduction band of WSe_2 undergoes indirect transition to the valence band of $MoSe_2$ by moving in real space shown by black arrow. From our old calculations we know that at the interface of this heterostructure, the highest valence band edge of WSe_2 is located at the Γ valley of its first brillouin zone and the lowest conduction band edge of $MoSe_2$ located at the K valley of its own first brillouin zone.

An electron transitioning from WSe_2 to $MoSe_2$ experiences an indirect momentum exchange from the middle of the brillouin zone of the later to the corner of the brillouin

zone of the former shown in figure 7.6c. We found from the flat band condition shown in figure 1.8 that this interlayer gap is about 1 eV; this is the activation energy an electron needs to transition across the interlayer gap. The existence of phonons is required in this system to both enable the momentum exchange for electrons, and to compensate the energy difference for the space indirect transfer when we reduce the photoexcitation energy.

Figure 7.6b shows electron transitions at different photon excitation energies. We have a very clean system, no intermediate energy level, no ions, and we have one transition of 1 eV from the highest valence band of WSe_2 |0,0> (ground state) to the lowest conduction band of $MoSe_2$ |1,0> (first excited state) shown by X_I (interlayer exciton). Based on Born-Oppenheimer approximation we can separate the contribution of electrons and phonons in an energy level, such that electronic ground state can consist of several excited phononic states.

The second peak in figure 7.6b is observed with a photoexcitation of 30 meV smaller than the first peak. We argue that phonons with energy of 30 meV are assisting this antistokes process to happen in the system by compensating the energy difference neede to generate an interlayer exciton. Consequently three more peaks each with photon energy of 30 meV smaller than the previous one observed in figure 7.3a indicated by arrows in figure 7.6b. The second transition takes an electron in its ground state combined with a phonon at its first excited state to a state where electron would be in its first excited state and phonon in its ground state, in another word phonons are being consumed for this transition to happen.

We argue that the energy difference for transitions is compensated by phonons of energy 30 meV in the system, one, two, three and four phonons respectively are being pulled out of the system and spent efficiently for an electron indirect transition between the states. This number is in perfect agreement with our Raman measurements shown in figure 7.1b, where we observed the strongest peak with energy 30 meV an indication of the existence of low frequency optical phonons in the system. These phonons in the system are assisting the anti-stokes processes in this 2D-TMD based semiconductor heterostructure photocell.

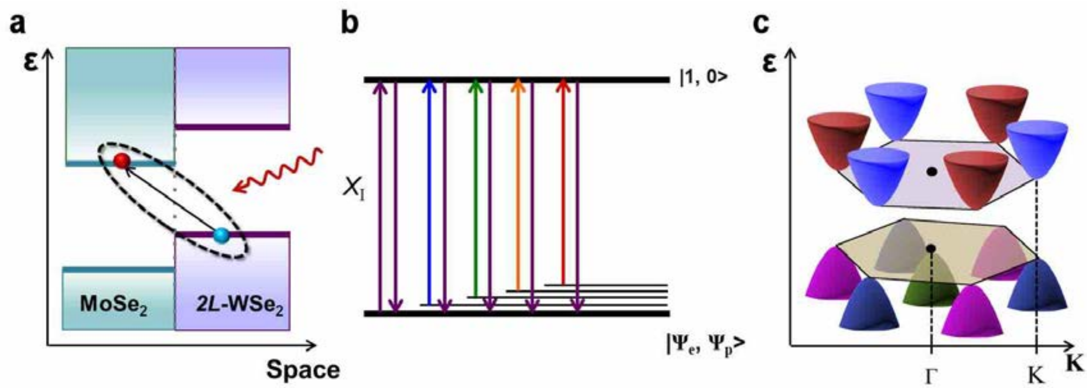

Figure 7.6, Band profile, two-level system transitions, and *E-K* diagram of the heterointerface of *2L*-WSe_2/$MoSe_2$. a, Band profile in the lateral direction, a photon with controllable energy photoexcites the heterointerface and generates indirect interlayer excitons. b, Two-level system of the interface, X_I is an indication of interlayer exciton. Arrows from phononic excited states are representing phonon-assisted antistokes shifts. c, *E-K* diagram of the first BZ of the interface, the top BZ belongs to $MoSe_2$ layer with the lowest conduction band located at K point valley while the bottom BZ belongs to WSe_2 layer with highest valence band located in Γ point valley.

REFERENCES

1. Pringsheim, P., Zwei Bemerkungen über den Unterschied von Lumineszenz- und Temperaturstrahlung. *ZeitschriftfürPhysikAHadronsandNuclei* **57**,739-746, (1929).

2. R. I. Epstein et al., Observation of laser-induced fluorescent cooling of a solid. *Nature (London)* **377**, 500 (1995).

3. Sheik-Bahae, M., & Epstein, R. I., Can laser light cool semiconductors?. *PRL* **92**, 2474031-4 (2004).

4. Zhang, J., Li, D., Chen, R., & Xiong, Q., Laser Cooling of a Semiconductor by 40 Kelvin: An Optical Refrigerator Based on Cadmium Sulfide Nanoribbons. *Proc. of SPIE* **8638** 863808-2 (2013).

5. Seletskiy, D. V., et al., Laser cooiling in solids: advances and prospects. *Rep. Prog. Phys.* 79 096401 (2016).

6. Tonndorf Ph., et al., Photoluminescence emission and Raman response of monolayer MoS2, MoSe2, and WSe_2. *OPTICS EXPRESS* 4909, 21 (2013).

7. Hong, X. et al. Ultrafast charge transfer in atomically thin MoS2/WS2 heterostructures. *Nat. Nanotechnol*. 9, 682-686 (2014).

8. Rivera, P. et al. Valley-polarized exciton dynamics in a 2D semiconductor heterostructure. *Nat. Commun*. 6, 1-6 (2015).

9. Ross J. S., et al., Electrical control of neutral and charged excitons in a monolayer semiconductor. *Nature Communications* **4**, (2013).

10. Shepard G. D., et al., Trion-Species-Resolved Quantum Beats in $MoSe_2$. *ACS Nano*, **11**, 11550-11558 (2017).

11. Wang G., et al., Excitons in atomically thin transition metal dichalcogenides. *Rev. Mod. Phys.* **90**, 021001-0210025 (2018).

12. Barati, F. et al. Hot carrier-enhanced interlayer electron–hole pair multiplication in 2D semiconductor heterostructure photocells. *Nat. Nanotech.* **12**, 1134–1139 (2017).

CHAPTER 8

CONCLUSION

We started chapter 1, with presenting the characteristics and basic operation of the elementary building blocks of semiconductor electronic devices: semiconducting P-N junctions. We then introduced light to study its interaction with matter within these junctions: P-N junction photodiodes. We aim to integrate a class of atomic layer semiconductor known as transition metal dichalcogenides (TMDs) into semiconductor photodiodes and study the optoelectronic characteristics. Before discussing that we presented a brief theory of TMDs electronic band structure and studied *2L*-WSe_2/$MoSe_2$ in particular through DFT calculations. To understand the electronic transport in these devices we first studied the density of available electronic states (DOS) in conventional 2D electron gases. We then calculated the DOS of TMDs through their band dispersion. Through these calculations we found that DOS is independent of energy states in conventional 2D systems while it's linearly proportional to energy states in 2D-TMDs.

We continued chapter 3 with presenting the procedure to wafer preparation, exfoliation, making stacks and finally device fabrication. Dry transfer method is used for making stacks, for device fabrication we used EBL, FIB and metal deposition methods.

An experimental instrumentation was necessary to perform measurements on these devices. The supercontinuum scanning photocurrent spectroscopy microscope is designed and developed for most of the work presented in this thesis. In chapter 4 we present the

development of this microscope by combining spatially and spectrally resolved laser excitation techniques along with an electronic transport experiments platform.

Using advanced optoelectronic measurements, we discovered highly efficient multiplication of interlayer electron-hole pairs at the interface of a *2L*-WSe_2/$MoSe_2$ integrated into a field- effect heterojunction device, the results are discussed in chapter 6 of this thesis. Electronic transport measurements of the interlayer current-voltage characteristics indicate that layer indirect electron-hole pairs are generated by hot electron impact excitation at temperatures near T=300 K. By exploiting this highly efficient interlayer e-h pair multiplication process, we demonstrated near-infrared optoelectronic devices that exhibit 350% enhancement of the optoelectronic responsivity at microwatt power levels. This efficient energy relaxation pathway that competes with electron thermalization losses, make 2D semiconductor heterostructures viable for a new class of hot-carrier energy harvesting devices that exploit layer-indirect electron-hole excitations.

Through our novel spatially and spectrally resolved measurements (in chapter 7) on these high quality 2D-TMD devices, we've been able to isolate the interlayer exciton species through a phenomenon called phonon assisted antistokes process and have identified an entirely new light-matter interaction within these states. We show that under optimized experimental conditions phonon assisted anti-stokes absorption near the interlayer exciton edge of a van der Waals semiconductor heterostructure composed of tungsten diselenide and molybdenum diselenide become dominant, such that at low photon energies near 1eV, we observed a strong photocurrent peak with several low

energy echoes spaced by 30 meV below this fundamental absorption feature. This process, which we find to be highly efficient due to the alignment of the exciton dipole moment to the atomic displacement of the out-of- plane optical phonon modes, marks the first and most critical step toward laser cooling of atomic layer semiconductors. Moreover, the anti-stokes absorption process observed here could enhance the efficiency of next generation photovoltaics, since it converts vibrational energy into electronic excitations using photons with energies that are lower than the band gap, manuscript is in preparation.